COMPUTATIONAL FRAMEWORKS FOR MATERIALS DESIGN AND ADDITIVE MANUFACTURING

A Dissertation

by

LUKE AARON JOHNSON

Submitted to the Office of Graduate and Professional Studies of
Texas A&M University
in partial fulfillment of the requirements for the degree of

DOCTOR OF PHILOSOPHY

Chair of Committee,	Raymundo Arróyave
Committee Members,	Ibrahim Karaman
	Alaa Elwany
	Patrick Shamberger
Head of Department,	Ibrahim Karaman

May 2019

Major Subject: Materials Science and Engineering

ABSTRACT

The discovery of new materials is a necessary component for the advancement of humanity as a species, which is evidenced by the common practice of delineating major eras of humanity by the materials associated with the most advanced technologies of the time: Stone, Bronze, Iron, etc. The introduction of new materials has progressed beyond discovery of new elements to the development of highly specialized materials that possess properties far greater than the sum of their elemental constituents. Traditional experimental techniques for optimizing these materials are often outpaced by the rapid development cycles of the technologies that they ultimately enable. Fortunately, the same computational power that has allowed faster technology development overall can also be used to accelerate materials development. This is accomplished by supplementing experimental results with physics-based simulations that improve extrapolative predictions beyond our current state of knowledge.

There are a multitude of issues to consider when developing a coupled approach between experimental and computational methodologies. Engineering design principles can aid in the co-development of both experiments and simulations by providing a common ground and a common set of tools to formalize the problem/objective. The four parts of this dissertation are primarily focused on the development of computational frameworks for the design of new materials and/or processing conditions. In the first work, a materials design framework based on the idea of Efficient Global Optimization was developed to optimize the ratio of Aramid Nanofibers, Graphene Oxide, and Carbon Nanotubes within a composite supercapacitor electrode, subject to a user defined preference for the tradeoff between mechanical and electrochemical performance. The second work establishes a novel technique for quantifying and visualizing the uncertainty associated with precipitation model predictions used to tailor the transformation behaviour of a Ni-48wt.%Ti shape memory alloy. The third work details the coupling of the aforementioned precipitation model with a symmetry-enhanced Finite Element thermal model to look at secondary phase formation during additive manufacturing of a Ni-49.1wt.%Ti shape memory alloy. The fourth work presents a com-

putational framework for predicting the printability of alloys for additive manufacturing and shows very good agreement with experimental observations from a Ni-5wt.%Nb alloy, and an equiatomic CoCrFeMnNi alloy.

DEDICATION

To all of the people who have helped me reach this point in my life, through the good times and the bad. We are who we surround ourselves with and I am very fortunate to have the support of such a remarkable group of friends and family. I never would have made it without you.

CONTRIBUTORS AND FUNDING SOURCES

Contributors

This work was supported by a dissertation committee consisting of Professor Raymundo Arróyave [advisor], Professors Ibrahim Karaman and Patrick Shamberger of the Department of Materials Science and Engineering and Professor Alaa Elwany of the Department of Industrial & Systems Engineering.

The experimental data analyzed for Chapter 2 was provided by Professor Jodie Lutkenhaus. The experimental analyses depicted in Chapter 2 were conducted by Anish Patel of the Department of Chemical Engineering. The experimental data analyzed for Chapter 4 was provided by Professor Ibrahim Karaman. The experimental analyses depicted in Chapter 4 were conducted by Ji Ma and Brian Franco of the Department of Materials Science and Engineering. The experimental data analyzed for Chapter 5 was provided by Professors Ibrahim Karaman, Alaa Elwany, and Hans J. Maier. The experimental analyses depicted in Chapter 5 were conducted by Raiyan Seede and Hannah Boon of the Department of Materials Science and Engineering; Bing Zhang and Mohamad Mahmoudi of the Department of Industrial & Systems Engineering at Texas A&M University; and Janine T. Maier of the Institut für Werkstoffkunde (Materials Science) at Leibniz Universität Hannover. All other work conducted for the thesis (or) dissertation was completed by the student independently.

Funding Sources

Graduate study was supported by the following funding sources: NASA–Space Technology Research Grants Program, Early Stage Innovations [grant number NNX15AD71G]; the NSF Research Traineeship for Data-enabled Discovery and Design of Energy Materials [grant number 1545403]; and the Army Research Office [grant number W911NF-18-1-0278]. Portions of this research were conducted with the advanced computing resources provided by Texas A&M High Performance Research Computing.

TABLE OF CONTENTS

Page

Page

LIST OF FIGURES

FIGURE Page

FIGURE Page

LIST OF TABLES

TABLE Page

1. INTRODUCTION

This chapter consists of a broad overview of the principles associated with materials design and additive manufacturing, which are the two main concepts discussed in this document. Detailed introductions pertaining to the specific content of each individual chapter can be found at the beginning of each chapter. The first section of this chapter discusses the historical development of materials, the transition from descriptive to prescriptive methodologies in materials science, and detailed discussions of the current paradigms of materials design. The second section contains a summary of metal-based additive manufacturing in terms of its history, current issues, potential solutions to those issues, and lessons that can be learned from more well established disciplines like welding and other laser-metal processing techniques. This chapter is concluded with a brief section summarizing the contents of each project and how the concepts contained therein are related to the broader topics discussed here in the introduction.

1.1 Materials Design

It is generally known that materials are the primary limiting factor when considering the development of new technology. This idea is reflected in the classification of prominent eras in human history based on the material associated with the most advanced technology available at the time: stone, bronze, iron, plastic, silicon. Each one of these advancements enabled the development of new technologies for the betterment of humankind and exploration of our world and solar system. In many of these cases, the discovery of these groundbreaking new material classes was often the serendipitous byproduct of experimental exploration. While we as a species are surely grateful for these discoveries, our appetite for advancement has grown exponentially in recent decades meaning that materials development cannot be left to chance. This demand has required a dramatic shift in the field of Materials Science and Engineering from a primarily descriptive discipline to a more prescriptive mindset. This new mindset requires a more standardized approach to the characterization and prediction of materials and their complex interrelated physical phenomena.

Engineering design concepts provide the tools required to formalize our collective knowledge of materials. The application of design principles accelerates the development and discovery of new technologies by identify potential performance gaps of existing technologies through the formalization of complex relationships within their systems [1]. One useful concept for understanding materials development is that of the innovation S-curve, which characterizes the maturation of a technology over time as an increasing sigmoidal function. In the S-curve model, the rate of improvement of the technology is slow in the early stages, reaches a maximum rate of improvement in the middle of the life-cycle, and slowly tapers off near the end as that particular technological implementation is perfected. Revolutionary ideas that address the same need more effectively with an entirely new approach are considered to be the start of a new S-curve. In the context of the stone, bronze, and iron ages, as each material reached full maturation (the end of its S-curve), a new higher performing material class (new S-curve) was discovered and the trend of technological advancement continued. As a new material class is introduced, development of the previous technology is not eliminated, but the research focus for that material often shifted to that of specialization and differentiation from other materials. In fact, there are still ever-evolving use cases for all materials classes associated with the eras of humanity: stone in the form of obsidian is still used in specialized surgical scalpels, bronze has widespread use in bearings and propellers, and iron is used extensively in the form of various steel products. This idea of innovation both *within* and *between* S-curves highlights one of the fundamental decisions present in materials design; incremental optimization of an existing material vs. exploration for the discovery of the potentially groundbreaking new materials.

An example of optimization within a material class (i.e. within an S-curve) is the continual development of steel over the course of hundreds of years. In an effort to compile these centuries of accumulated knowledge, Materials Scientists in the mid 90's introduced the concept of materials as systems [2]. In that key work, Greg Olson detailed an approach in which interrelated physical phenomena that occur within steel were conceptualized as a hierarchical network of relationships linking the processing history and resultant microstructure of a steel alloy to its mechanical perfor-

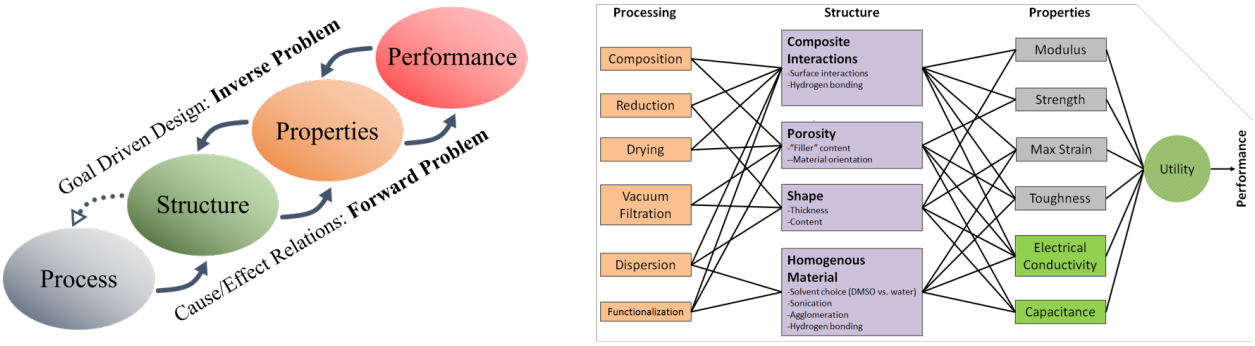

Figure 1.1: Typical examples of the (a) process-structure-property hierarchy proposed by Olson and (b) example systems chart for the design of a supercapacitor electrode.

mance. The general schematic of this concept, as well as a detailed example of a complete system can be seen in Figure 1.1. This hierarchical understanding of materials phenomena can be applied to any system and has seen widespread adoption within the materials science community to this day. Design of the material in question is accomplished by coupling the deterministic description of a materials Process-Structure-Property (PSP) with iterative optimization techniques that search the user-defined input space for a particular set of processing conditions that result in some optimal value of a material property like yield strength or corrosion resistance.

The concept of materials as systems is very useful when trying to balance competing physical phenomena within a particular material system, but they do not typically provide a way of extending beyond the design space immediately surrounding the system. On the other hand, Ashby focuses on drawing conclusions across material boundaries through the use of projections and performance-based combinations of material properties to aid in performance-based materials selection in product design, as seen in many of his works. Ashby's approach can highlight gaps in the current design space and indicate gaps in the research, but it provides minimal guidance on how to attain that performance. Ashby actually wrote about this need for outward looking frameworks to guide material design as far back as 1987 [3].

The approaches of Ashby and Olson excel at *exploiting* the current design space, but lack guidance mechanisms for *exploring* new materials. Additionally, they require a significant amount

of pre-existing knowledge in order to be successful. This is not to say that their approaches are not useful, in fact both Olson and Ashby have close ties to commercially successful businesses (Questek ®and Granta ®, respectively) which were built around their design principles. However, focusing on either one of these techniques ignores the potential design space of completely new materials.

The biggest technological leaps forward were not prompted by slowly optimizing within the material systems of the day, they were often stumbled upon by chance well outside the composition space of known materials and alloys of the time [4]. As an example, high entropy alloys, which are currently specifically designed to be in the middle of composition space, are a huge topic of discussion at the moment because of their unique properties [5, 6]. A less recent, but more ubiquitous example of near equiatomic alloys can be found in NiTi shape memory alloys which exhibit very useful mechanical behaviour in response to externally applied stresses [7]. Clearly, there are game-changing alloys at non-standard compositions that have yet to be discovered and the real challenge is to create material-agnostic frameworks that help guide the exploration of this vast design space.

1.1.1 Hierarchy of Representations

Ideally, these design frameworks should consist of generalized material models, experimental methods for testing these agnostic models, and search techniques that promote exploration. Practically, designers need to provide real-world solutions to specific problems using the most general framework possible. Designing with this mindset emphasizes the necessity of looking at the problem from a materials agnostic point of view at multiple levels of detail. Innovation within this field often centers around finding unique ways of transferring and combining information throughout these various levels of detail [8, 9]. The Materials Genome Initiative and Integrated Computational Materials Engineering initiatives focus on developing these methods [10, 11]. A shift in thinking about design frameworks from a material centered hierarchy, to a hierarchy of physical abstractions may help shift focus to more material agnostic methodologies. Research methods within this design hierarchy can be classified into three levels of abstraction as shown in Figure 1.2.

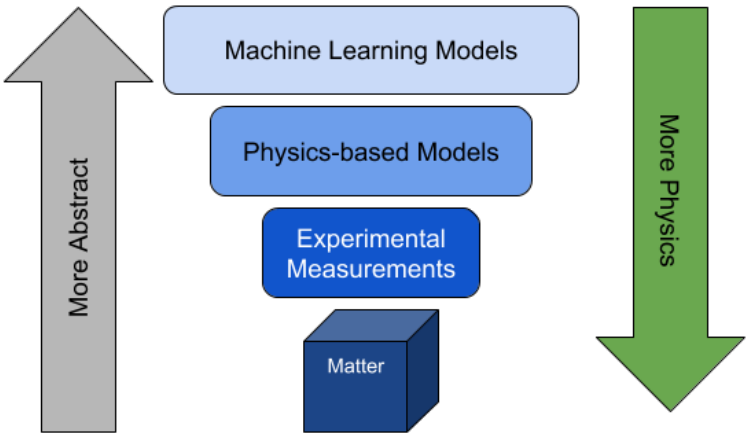

Figure 1.2: General view of materials design as a hierarchy of abstraction where each subsequent level contains less "physics".

The physical object itself is at the most fundamental level because, by all accounts, matter cannot ignore the laws of nature. Experimental characterization of the physical object is just above that, since they are the most accurate representation of the physical object available. Characterization ignores the least amount of physics, but still is not a perfectly accurate representation. This level is full of snapshots and projections of what is actually happening in the real material. For example, a material can be subject to two different types of experiments which characterize the material's mechanical and electrical responses to external stimuli. This level of abstraction consists of sets of data points characterizing the most important aspects of the material in question. Unfortunately, the number of available data points is inevitably limited and this is where the next level of abstraction becomes useful.

The next level of abstraction consists of physics-based models that are used to fill in the gaps and identify trends of experimental measurements. These models have some basis in the underlying physical behavior we hold to be true through repeated observations across many different materials. This is the realm of thermodynamics and kinetics. The fundamental laws of thermodynamics are the broadest example in this category and serve as the starting point for many of the models contained therein. Scientists like Fick, Fourier, and Maxwell are famous for recognizing trends and creating equations that describe mass and energy transport phenomena from these basic

principles and experimental observations. We still use these fundamentals today, but add extra terms to account for discrepancies between the basic model and measurements taken in specific material classes.

The idea of abstraction can be extended to the point at which no currently known physical principles are included in the model whatsoever. This is the realm of non-parametric machine learning where models are simply fit to data and subsequently used to predict and guide experimentation. In general, this increasingly abstract model leads to shorter computational times and an increase in the searchable area. Chances of finding a solution with these machine learning techniques can be increased by including information from the less-abstract more-physical results from lower levels of the hierarchy. This increase in predictive capability after calibration also applies to physics-based models.

Although this abstraction structure is not motivated by the paper, it has many similarities with the four paradigms described in Agrawal and Choudhary's recent perspective paper on data informatics in materials science [12]. Informatics based materials discovery has become popular in recent years [13, 14, 12]. While a purely data-drive approach can be successful, speed and accuracy of the framework is increased if past knowledge of physical insights is include in the predictions. A hierarchical structure like this is necessitated by the existence of discontinuities and unforeseen correlations between variables that are not necessarily predictable *a priori*. If all materials had smooth responses to external stimuli and behaved like ideal mixtures, perfect models could be created based on one or two data points. This is most certainly not the case, so the best option is to create frameworks that make the best decision possible with whatever data is currently available.

If the goal of design is exploration and discovery of new materials, a successful framework must have the ability to incorporate information from all levels of abstraction. For example, a machine learning model that doesn't incorporate any physical principles has a much smaller chance of finding reasonable results upon extrapolation. On the other hand, breakthrough materials that revolutionize industries often don't agree with any of the physics-based trends fit to the existing data at the time. Obviously, there are some decisions that need to be made about which level of

abstraction is appropriate for the current situation. Materials designers can make the most impact when developing these frameworks by finding more-informative projections, developing unique combinations of existing models and experiments across the various levels discussed above [8, 9].

1.1.2 Uncertainty in Design

The next question then becomes: what information is necessary in order to make these decisions about what to include in a framework. The most obvious metrics are how confident the user is in the results, and how sensitive the results are in the areas of interest. These two metrics may be quantified by error bars on experimental data, R-squared values at the physical modeling level, or precision and recall metrics at the Machine Learning level. In lieu of these metrics, a quick analysis of the significance of any major assumptions can provide a rough estimation of the uncertainty associated with the given predictions. The landscape of potential search areas and the risks associated with those predictions is the most complete and honest representation of the current state of knowledge in a project. The decision about which approach to take is ultimately based on the intersection between the uncertainty of the prediction and the risk-aversion of the end user.

The quantification and consideration of uncertainty within the design process can have significant impacts on both local optimization of existing materials and global exploration for new materials. However, inclusion of uncertainty within the design process can come with some drawbacks like the time and cost associated with experimental replicates or Monte Carlo sampling of a computational. These considerations may render uncertainty based search and optimization criteria unfeasible in some situations. That being said, this assertion of the importance of uncertainty in materials design is backed by many well established communities within the field of materials science [15, 16, 10]. Recent publications have also shown how the direct incorporation of uncertainty as a predictor can inform alloy modifications for the optimization of material performance characteristics [17].

There are numerous approaches to quantifying the uncertainty and accuracy of the predictions. Quantification can be split into two large categories consisting of local quantification and global quantification. Local quantification can be achieved via analytical derivations of the governing

equations is possible. If The governing equations are not known, an iterative numerical sampling method can be used. Although numerical sampling approaches introduce confounding information in the form of finite sample size effects, these methods are consistently applicable across many complicated systems and the models themselves are usually close to reality. The third option for local characterization is that of experimental replication which develops a better understanding of uncertainty/variability at certain regions of the design space by repeating experiments at those locations. Replication is typically the most expensive option and is even more susceptible to finite sampling issues, but is also the closest to reality and is applicable to arbitrarily complex systems. All three of the methods above are descriptive of the current state of knowledge about a system and are useful in determining whether a data point or simulation result can be trusted.

If uncertainty is to be included directly as a feature in the design optimization approach, it is necessary to introduce methods for predicting uncertainty in regions far from available data or simulations. This is mostly relevant during global exploration of the design space outside of currently known materials and processing conditions. If the designer wants to use a particular functional form to introduce some physical assumptions into the system, confidence and/or prediction intervals can be used to predict uncertainty throughout the design space. Confidence intervals quite literally represent one's confidence that the model parameters represent the true physical parameters. Prediction intervals are an extension of confidence intervals which include sample size contributions to the uncertainty of model parameters (i.e. are the data used to train this model an accurate reflection of the true distribution?). The inclusion of uncertainty in the parametric model based approach may counteract some of the biases associated with its physical assumptions. As mentioned above, the use of parametric models can be more useful for gaining generalizable knowledge about material phenomena, but they may miss potentially groundbreaking material discoveries due to their basis in currently understood physics. Another method of uncertainty prediction throughout the design space is associated with the non-parametric (i.e. non physics based) response surface models such as Gaussian Processes Regression. This method predicts uncertainty by assuming a functional form for the spatial correlation between points in the design space, meaning that points

further from experimental or physics based simulation data will have greater uncertainty associated with them. The non-parametric nature of this approach is easy to implement and removes any model bias since it contains no assumptions about physical phenomena underlying the data. The downside is that the knowledge gained during the design optimization scheme will be highly specific to that particular problem and as such may not be generalizable to other material systems or design problems.

The concept of predicting some interval surrounding a mean prediction surface can be extended by considering the evolution of the distributions itself. Direct calculations of material property distributions result in more realistic predictions of uncertainty/variability throughout a design space, but come with a significant increase in computational complexity and simulation time when compared to other approaches that assume normally distributed values and spatially correlated variability in the design space, as described in the previous paragraph. For example, instead of simply predicting the evolution of the average size for a population of particles (a single number), the simulation would need to predict the evolution of the entire size distribution of particles. This is yet another example of decisions that must me made between different levels of abstraction during the design process, as discussed in Section 1.1. Monte Carlo methods can be used to determine a distribution of output values for a model without any changes to the underlying equation by repeatedly sampling from distributions associated with the input parameters. While Monte Carlo sampling can be computationally expensive, it is often less time intensive overall when compared to the alternative of reworking/extending the governing equations of an existing model to include full distribution calculations. Sampling methods of this style can also be accelerated through the use of computationally inexpensive surrogate models that can accurately approximate the local response of the full model [18, 19].

In general, including uncertainty as a consideration during the iterative design process can lead to larger increases in performance with little-to-no increase in risk. Furthermore, quantification of uncertainty associated with design-selected input variable combinations can point the way toward continued improvement even after the optimal processing conditions have been determined. This

all comes at a cost of slower, more costly iterations within the design framework, but is typically worth it when designing technologies with high costs of failure like those of the aerospace industry.

1.2 Additive Manufacturing

1.2.1 Background

The previously mentioned transitions between material eras (stone, bronze, iron, plastic, silicon) have all been enabled by the development of technology that could supply energy at higher densities, for longer times, with more precise control. Although it was developed well after the Iron Age began, the Bessemer process drastically reduced the cost of producing steel and helped initiate the industrial revolution which significantly increased the rate of technological evolution. Material processing through the application of laser and/or electron beams is essentially the culmination of this progression through ever increasing magnitude of applied energy densities. These energy deposition techniques were first used for precision welding in the 60's and 70's [20, 21]. Applications of electron and laser energy deposition methods quickly expanded from 1-dimensional welding to 2-dimensional surface processing methods such as remelting, hardening, cladding, and cleaning [21]. Lasers in particular have seen widespread adoption in industry over electron beam techniques due to their ability to process electrically conducting and insulating materials in non-vacuum environmental conditions [20, 21]. Leveraging knowledge gained in the development of 1D and 2D laser processing techniques, scientists and engineers established methods for the construction of 3-dimensional shapes through successive build-up of 2D surfaces. The first patent for producing 3D parts via laser energy deposition, now commonly known as Additive Manufacturing (AM), was granted in 1989 [22].

In general laser-based AM processes construct desired part geometries through sequential fusion of metallic powder from individual layers onto a previously fused layer. Within each layer, the desired shape is selectively melted as a laser (with a diameter on the order of 100 μm) rasters across the surface, tracing parallel linear paths on the surface of the part corresponding to the desired part. Once the laser has traced the entire shape for that layer, the build plate is lowered one

layer thickness and a fresh layer of powder is rolled across the surface of the part, ready to be melted in select locations. This process is repeated over and over again, with slight laser pattern variations on each layer, until the entire part has been fused together. The overall concept is similar to that of CNC milling, but instead of removing material with a cutting tool, the material is added through the fusion of powder onto the previous layer.

The geometrical freedom inherent to AM positions it as the go to manufacturing method for the replacement of complicated multi-part sub-assemblies with singular monolithic components [23]. Additive manufacturing allows for internal cooling channel morphologies that would be impossible to achieve through traditional manufacturing or machining techniques [24, 25]. This ability to print almost any shape imaginable has had tremendous influences on design for weight reduction of structural components through topology optimization [26]. In addition to geometric freedom, additive manufacturing enables the design of parts with spatial variations in material properties throughout the geometry of the as-built part. This spatial functionalization is performed by modifying the material in one of two ways: i) direct modifications to the composition of the material powder [27, 28], or ii) local variations in the processing parameters of the laser [29, 30, 31, 32]. Unfortunately, this design freedom comes with some drawbacks. The mechanical strength and fatigue life of AM components are significantly worse than that of the intrinsic bulk properties. This is in large part due to defects that become embedded within the components during the fabrication process [33, 34]. The next section focuses on descriptions of the energy transport processes within additive manufacturing and the physical phenomena associated with those processes.

1.2.2 Important Phenomena

Laser energy and matter interact in a highly dynamic way with many different modes ranging from simple heating and conductive dissipation within the solid substrate [35] to the development of a stable high temperature plasma above the melt pool [36]. Complexity of these interactions is also compounded by the presence of a thin layer of powder on top of the substrate. Modeling and characterization of critical aspects of the AM process helps scientists and engineers make better

decisions about short-term engineering solutions to existing problems, and can also guide the design and optimization of both AM machines and materials to address longer term goals. Selection of the appropriate models and characterization techniques for these endeavours requires an understanding of the important phenomena that occur during the primary energy transport processes: transmission, absorption, or dissipation. Phenomena associated with each of these three processes are defined and discussed below.

1.2.2.1 Transmission

The transmission of laser energy from the focusing lens to the melt pool surface is primarily affected by the composition of the media through which it is being transferred. In general the media that the laser may interact with can be broken down into the inert gas that fills the build chamber (typically Ar or He), and any metallic vapor that has evaporated from the surface of the part. Both of these media have an affect on the laser transmission but special care must be taken when considering metallic vapor effects which can lead to diffraction and/or absorption of the laser above the surface of the melt pool [37, 38]. At high laser energy densities, the environment directly over the melt pool consists of stable plasma cloud surrounded by a less stable cloud of metallic vapor. Interactions between the laser and these two regions occur through Rayleigh scattering and/or Inverse Brehmsstrahlung absorption [36, 39], depending upon the energy density of the incident laser. At energy densities less than 10^{10} W/m^2, the vapor is essentially transparent, but begins to condense droplets that can slightly obscure/absorb/distort the laser beam. Energy densities between 10^{11}-10^{14} W/m^2 result in ionization of the vapor and the formation of a stable plasma above the melt pool which absorbs and subsequently re-radiates a significant portion of the laser's incident energy [40]. This results in a heating case where the energy is actually deposited from two sources, the remaining laser energy that survived transmission through the plasma, and the radiation associated with the plasma. Ablation occurs at energy densities greater than 10^{14} W/m^2, sending shockwaves into the material and ejecting particles [39].

The main sources of literature on this topic come from research on laser welding. Experimental characterization of these laser/vapor/plasma interactions primarily focus on determination of vapor

composition through spectroscopic techniques [41, 42, 43, 44, 45, 46] and quantification of the diffraction and absorption of the laser within the vapor/plasma region above the melt pool [36, 37, 47, 48, 49]. Laser attenuation, diffraction, defocusing is typically studied by shining a secondary laser through the plume to a detector on the other side. This detector records the size, shape, and incident energy of the beam and compares the results to control case with no plume present. Attentuation and defection of the incident beam are both <10% in all experiments, but defocusing of the spot size by up to 50% has been reported for Aluminum alloys [43]. Keep in mind that these values are measured through a small cross-section of the plume, so one would expect the effect to be magnified in the primary AM laser which has a much higher energy density and must pass through the entire vertical column of the plume. Many of these papers show that introducing forced convection parallel to the build plate with a side gas can significantly reduce the effects of the outer plume, however this is not a viable option in powder bed fusion processes as the side gas would remove the powder layer from the surface of the part. Other studies have looked at the influence of the chemical identity and pressure of the shielding/inert gas within the build chamber. Helium is shown to shift the onset of plasma formation to higher energy densities, as compared to Argon due the higher ionization potential of Helium [49]. Reduction in pressure of the build environment has also been shown to suppress plasma formation [50].

In general most AM machines can reach laser energy densities on the order of 10^11 W/m^2, so interactions between the laser and plasma/vapor can be important. While AM machines do not have significant variations in produced laser power, the actual deposited laser power may vary significantly due to the laser/vapor/plasma interactions discussed in this section. These variations in laser power can cause significant variability of the weld pool which will lead to increased porosity and a reduction in overall performance of the as-built part. With this in mind, the best option for addressing these issues is to work a energy densities sufficiently low enough to suppress plasma formation entirely. This high energy density region is in the same corner of laser parameter process space (power and speed) associated with keyhole-shaped weld pools, which are typically seen as detrimental in additive manufacturing because of their increased propensity for vapor entrapment

due to melt pool instabilities. The mention of keyhole-mode welding leads into a discussion of absorption, which is the next stage of the energy transport process associated with laser energy deposition.

1.2.2.2 Absorption

Regardless of what percentage of the laser energy makes it from the focus lens to the build surface, the morphology, material, and phase present at the incident surface has a strong influence on the amount of energy absorbed into the material. In AM literature, studies of laser absorption have historically focused on modeling interactions between the laser and powder layer which predict absorptivities values in the neighborhood of 0.6 [51, 52, 53, 54]. While this makes sense at very low energy densities (before the onset of melting) it ignores the fact that the laser is primarily incident upon the molten metal for the duration of the print, which has an absorptivity closer to 0.3. Evidence for this reduction in absorptivity at the onset of melting was presented in two recent experimental works by Trapp [35] and Matthews [48]. These studies also showed an increase in absorptivity upon keyhole formation which is commonly attributed to the reflections of the laser within a recoil pressure induced depression in the melt pool. Absorption and reradiation of laser energy within any plasma contained within the keyhole region, as discussed in the Section 1.2.2.1, may also contribute to the increase in absorptivity. It is hard to decouple effects of surface morphology when trying to understand the intrinsic absorptivity, however minimum absorptivity values of the liquid metal in [35, 48] approach values close to that of a polished solid metal substrate of the same material. There are slight differences in absorptivity between powder-covered and bare substrates due to the fact that a small fraction of the laser energy (10%) is actually incident upon the powder in front of the melt pool [55]. In contrast to the attentuation, deflection, absorption, and reradiation associated with laser transmission above the melt pool, incorporation of absorptivity effects within an analysis are much more straightforward as the effect can be included as a single parameter that modifies the incident laser power.

1.2.2.3 Dissipation

In the context of energy transport processes during additive manufacturing, the term refers to all of the thermal transport phenomena associated with the transfer of heat away from the area under direct contact with the incident laser. This encompasses heat transfer within the melt pool, heat transfer within the solid substrate, and phase transformations from solid to liquid and liquid to vapor. Marangoni convection is considered one of the most important transport phenomena within the molten melt pool and occurs due to the interaction between a material's temperature dependent surface tension and steep thermal gradients predicted at the surface of the molten pool [34, 55, 56]. Composition of the alloy (especially impurity elements like Oxygen and Sulfur) can have a significant influence on the surface tension and therefore the Marangoni convection of an alloy [57, 58].

In addition to the phenomena that dominate the behaviour of the liquid, solid, and vapor phases, transformations between these phases are important to consider. Latent heats of melting and vaporization are significant contributors to the total amount of deposited energy required to melt and/or vaporize material within the system [59]. As such, disregarding their effects can lead to under-prediction of the minimum laser power required to sustain a stable melt pool during the additive manufacturing process. The solid-liquid interface itself is one of the most common areas of research in AM because of the impact that the solidification microstructure has on the as-built part. Important considerations at this solid-liquid interface include morphology of the solidification front and segregation of elements (particularly Nb in Inconel718). At the liquid-vapor interface, the primary concern is vaporization of the metallic elements within the melt pool. This is of significant importance when considering differential evaporation in which the composition of the as-built part is changed due a difference in the vapor pressures of the elements present within the melt pool. While seemingly detrimental at first glance, this phenomena can actually be utilized to locally tailor the composition of the material [44]. This is exceedingly useful in material systems that are highly sensitive to changes in composition such as Ni-rich NiTi shape memory alloys [60]. Excessive vaporization can lead to the formation of a "keyhole mode" melt pool, that contains a

depression in the liquid surface that is formed from the recoil pressure of the vaporizing metal [61, 34]. While keyhole mode welding is not inherently troublesome, any collapses or instabilities in the keyhole do increase the likelihood of vapor bubble entrapment which serve as stress concentrators [61].

Thermal transport in the solid substrate is relatively straightforward compared to the liquid and vapor phases since it is purely conduction driven. The key modeling consideration in this phase is whether to use temperature dependent or constant material properties [62, 63]. Although the thermal modeling is straightforward in the solid phase, the temperature evolution is often coupled to other physical models that predict the behaviour of the solid-state phenomena listed above. Heat transfer considerations in the solid substrate are important because of the thermally driven phenomena that occur within it such as secondary phase formation, grain growth, and residual stress accumulation [64, 31, 65, 66]. Since these phenomena occur at longer ranges, longer times and lower temperatures than phenomena in the melt pool, the rastering pattern of the laser is much more influential. Thin walled structures pose limitations on the possible scan strategies so researchers have developed methods for modifying the original CAD model to compensate for the distortion [67]. In addition to significantly warping thin-walled structures, part distortion can lead to variations in powder layer thickness which subsequently increases the likelihood of cracking, delamination, and lack of fusion. After residual stress, grain growth and secondary phase transformations also have a significant impact on the properties of the as-built part, as is the case with α and β phases in Ti6AlV4. The primary driving force for texture evolution in additive manufacturing is the selective growth of grains that have their preferential growth directions more closely aligned with the direction of the long range thermal gradients within the solid substrate [31]. This results in a columnar texture of the grains that can lead to anisotropies in material properties. The formation of secondary phases is also an important phenomenon to consider since it can have both positive and negative effects on the as built part. The formation of precipitates within the material can be used to in a positive way to alter material properties locally within

the part [29, 68], but some precipitates like Laves phase and Ni_3Nb in Ni-superalloy systems are detrimental to the mechanical properties of the as-built part [69].

1.2.3 Control Techniques

In order for additive manufacturing to be adopted as a feasible and consistent engineering solution, mechanical property issues associated with the above phenomena must be eliminated in as-built parts. Porosity is the most common defect seen in additive manufacturing and can be attributed to the lack-of-fusion between the molten melt pool and substrate or the entrapment of vapor upon keyhole collapse [33, 34]. Causes for lack-of-fusion result from a lack of overlap between subsequent melt tracks due to improper distance between them [70, 71] and/or inconsistencies in track width when operating at laser speeds that cause instabilities of the melt pool width [72, 53, 73]. Gas bubbles can become entrapped through internal pores within individual powder particles or instabilities in the keyhole which causes it to collapse. Regardless of the cause, pores within the as-built part lead to issues of delamination between layers and internal stress concentrations that serve as nucleation sites for crack growth [72, 53, 73]. Much of the materials science based work on this research topic has focused on controlling these phenomena through optimization of machine parameters like the speed and power of the laser, although some research is now focusing on altering the composition for defect mitigation [74]. In some cases, the same feasible print range cannot be used for different locations on the build plate within the same machine [75]. This large variability in print quality is one of the predominant barriers to widespread adoption of AM structural components in high cost of failure applications like those seen in the aerospace industry.

While there is a general understanding of the physical phenomena behind most of these defects, there is not really a consensus about how to address this issue of variability across machines and materials [76, 75]. Understanding and controlling this source of this machine variance will ultimately make the machines more robust and increase the chance of successful fully-dense builds. This machine centered approach is completely valid, but there are other options available to explore from the perspective of materials science.

In materials science, we often modify existing materials in order to achieve some more optimal performance for a particular application. Making a more defect tolerant material can be achieved by increasing the feasible print range (relevant to the inherent variability of the process) or decreasing the sensitivity of the material to changes in process parameters. An early example of alloy modifications for selective laser melting looked at the effect of minor phosphorous additions can significantly decreased the melting temperature of the alloy, thereby altering the print properties [72, 77].

More recently, there have been a few examples of modifications to aluminum alloys which are notoriously difficult to print due to their susceptibility to hot tearing. In one case, Questek addressed this problem by slightly altering the Mg and Zn content of the alloy [78]. Researchers at UC Santa Barbara used a machine-learning based approach to find a slight addition that promoted grain refinement and homogeneous nucleation from the melt [14]. Taming of these seemingly difficult-to-print aerospace grade aluminum alloys, through relatively minor compositional adjustments shows that this alloy modification approach is just the tip of the iceberg.

Beyond defect mitigation, there are some advancements in the area of localized modification of material properties through changes in either process parameters or composition of the stock material [29, 27, 28]. Modifications of the process parameters like laser speed, laser power, and hatch spacing typically lead to much smaller variations in performance and can be seen as a way to fine tune certain properties. A few papers from Oakridge National Labs exhibited a way to create letters and graphics within the grain structure of an alloy through processing parameters [31, 32]. Recent work at Texas A&M showcased region based control of shape memory alloy transformation behavior via spatial variation in process parameters [29].

Localized functionalization within a single part can also be controlled by spatial variations in feed stock material in Directed Energy Deposition systems. This approach is an excellent example of practical compositional domain *exploration* mentioned above. Unfortunately the increase in dimensionality also comes with an increased risk of defect formation in the material. Research from Penn State and NASA's Jet Propulsion Lab show that simple linear paths through composition

space may lead to defects that make the part unusable [27, 28]. T. Kirk, O. Eliseeva, et. al. at Texas A&M are using a Machine Learning approach to efficiently navigate compositional space with the goal of avoiding undesirable phases. There are other design considerations as well, but this path-planning algorithm provides a good example of how to approach the problem of materials design for a specific application.

It is fairly clear, from the examples above, that the materials science based additive manufacturing community is moving toward a more exploratory mindset of solving current solutions through modifications to existing materials or development of new materials entirely. Exploring and optimizing within this new materials-focused design space requires frameworks for understanding the issues leading to optimal (or suboptimal) results for both defect mitigation and functional grading. To accomplish this, current materials design philosophies should be leveraged to create a framework specific to the design of alloys for additive manufacturing. Since the majority of the phenomena discussed above are thermally activated, the thermal model will be a key component to any such alloy design framework. Brief discussions of relevant approaches to thermal modeling in AM are presented in the next section.

1.2.4 Thermal Modeling

The majority of the phenomema discussed in Section 1.2.2 are thermally activated and/or highly dependent on thermal transport within the material. Because of this, research dedicated to the study of thermal transport during AM processing is one of the most studied topics in additive manufacturing. In general, AM thermal transport models can be separated into three main classes: analytical, fixed domain, and free-surface fluid flow. Even within these classes there is a large variety of approaches due to differences in assumptions between users. As mentioned in the design section of this chapter, selection of the model class, as well as assumptions within that class depend on the physical phenomena being discussed and available experimental data for validation. Sections 1.2.4.1 - 1.2.4.2 below contain summaries of the key works and associated physical phenomena within each model class. A table summarizing the main differences between each thermal model class can be seen in Table 1.1.

Table 1.1: Summary of assumptions and physics associated with different thermal modeling approaches used to study the additive manufacturing process.

			Analytical		Numerical	
			Rosenthal	Eagar-Tsai	Fixed Domain	Free Surface
Transport	Conduction		x	x	x	x
	Radiation				x	x
	Vaporization				x	x
	Fluid Flow	Convection			x	x
		Free-Surface				x
Assumptions	Thermophysical Properties	Constant	x	x	x	x
		Variable			x	x
	Reference Frame	Steady-State	x	x	x	x
		Transient			x	x
	Heat Source	Point	x		x	x
		Gaussian		x	x	x
		Arbitrary			x	x
	Phase Transformations				x	x

1.2.4.1 Analytical Methods

This class of thermal transport models were originally developed to study welding. Rosenthal developed one of the earliest models describing a traveling heat source [79] by assumes a point-source moving at a constant rate. While this analytical model is easy to implement, it does not provide accurate predictions of the weld pool profile itself. Many modifications and extensions were proposed over the years with the most well-known case being that of the distributed traveling heat source model published by Eagar and Tsai [80]. This work extended the Rosenthal model from a point-source to a distributed Guassian profile in order more closely approximate the arc-heating during traditional welding processes. The Eagar-Tsai (ET) model can be used as a good first approximation of weld pool profiles at traversal speeds and energy deposition rates that result in conduction mode melt pools [81].

While ET model results are more accurate than the original Rosenthal predictions, there are still significant limitations associated with the simplifying assumptions of the model. By considering

only thermal conduction and constant thermophysical properties in a quasi-steady state reference frame, the model cannot predict defect-associated phenomena such as keyhole formation. Calibrating the constant thermophysical properties of model for a wide range of traversal speeds and deposited energies presents some difficulty. Since specific heat, conductivity, and density are considered constant, changing the values will simply scale the results of the simulation, leading to better agreement in one area, but worse agreement in another. This approach can still be useful as long as its limitations are considered; it provides the correct trend in melt pool profiles, and can be used as a first approximation when trying to develop an understanding general trends in a material's response to welding and additive manufacturing processes.

1.2.4.2 Fixed Domain

Fixed geometry style numerical methods such as Finite Element (FE) methods are the most commonly used modeling technique for studying thermal transport phenomena in AM. This is mostly due to the wide range of available solvers and the ease of use of the many commercial software packages available. Additionally many universities offer FE element courses and some engineering colleges go so far as to select it as a required course. In the hierarchy of AM thermal models FE models are one step up from analytical style models like the ET and Rosenthal approaches discussed above. As shown in Table 1.1, the key differentiators between an FE approach and analytical methods are the abilities to include: temperature dependent material properties, phase transformations, arbitrary beam shapes/paths, and fluid dynamics for either a transient or steady-state reference frame. Different material properties can be applied to different regions of the domain considered in the domain, which enables the possibility of modeling the powder as well.

These relaxations shift the FE model closer to reality and result in the ability to more accurately predict the thermal response of a system to incident laser energy. The temperature dependent material properties provide more flexibility when calibrating the model to experimental results over the entire range of laser power and scan speed. Model calibration is typically done through comparisons of melt pool dimensions, but can also include peak temperature with the caveat that high

temperature readings are often not very accurate, even in the case of high-temperature pyrometer measurements. The inclusion of phase transformations also has a significant impact on the accuracy of the model in both the solid-liquid and liquid-vapor interface. Latent heat contributions represent a significant portion of the overall energy balance within the melt pool and lead to more accurate representations of the thermal gradients at the melt pool interfaces. The ability to incorporate the incident laser beam as a traveling heat source within a predefined domain allows for the extension of predictions beyond single track simulations. This means that the effect of scan strategies on the solid-state phenomena (residual stress, secondary phase formation, and grain growth/texture) discussed in Section 1.2.2.3 can be modeled. Fluid effects are incorporated via equations that govern the velocity of the liquid metal within the melt pool, albeit without consideration of the interface morphology evolution between molten metal and the environment. This additional physical contribution significantly increase the computational expense of the simulations, but allows for the explicit study of the effects of surface tension and Marangoni convection on melt pool morphology. These fixed geometry models represent a good trade-off between model complexity and predictive capability.

1.2.4.3 Free-Surface Methods

Although fixed geometry methods may include fluid flow, they cannot directly model balling, keyholing, or individual powder particles, all of which require the direct simulation of interfaces that are free to move and evolve over time. These highly detailed models are used to study the most fundamental phenomena associated with the liquid metal surface such as depression/keyhole formation upon rapid vaporization and reflections of the laser energy within those melt pool morphologies [34]. Modeling of the balling/humping melt pool phenomena requires the consideration of fluid properties such as viscosity, surface tension, and convection in the melt pool. ALE3D is a self-described hybrid finite-element finite-volume approach for modeling free surface evolution that was developed at Lawrence Livermore National Laboratory [82]. Carolin Körner et.al. have a computational framework that utilizes a Lattice-Boltzmann approach to model free surface evolution [83]. While very informative, these models are more applicable toward the study of

fundamental phenomena in AM, rather than for design purposes which often require many simulations and multiple iterations which may not be feasible due to the computational expense of this modeling approach. However surrogate modeling techniques can be used to interpolate between expensive physics-based simulations, as described in Section 1.1.

1.3 Overview of Dissertation

This dissertation describes the development and implementation of computational tools critical to the acceleration of materials discovery and development, particularly in the area of additive manufacturing. More general approaches like this often take a little bit longer than just solving the specific problem at hand, but it pays dividends in the future when similar problems are encountered. *The challenge of materials design is in framing a problem in a way that captures the necessary physics behind the issue without becoming so specific that the method only applies to one specific case.* The papers presented throughout Chapters 2-5 try to strike this balance by identifying and modeling the physics associated with the task at hand in the simplest way possible that also captures the relevant phenomena.

Chapter 2 presents a composite supercapacitor electrode design framework that incorporates both electochemical and mechanical design requirements. In the beginning of this project, the design goal and key points of influence were identified through the use of materials system charts discussed in Section 1.1. The finalized design framework used a machine learning methodology called Efficient Global Optimization to tailor the ratios of Graphene Oxide, Carbon Nanotubes, and Aramid Nanofibers within a supercapacitor electrode subject to design requirements that balanced the electrochemical and mechanical performance requirements equally. The success of this project showcases the potential benefits of combining various levels of abstraction within a single design framework. The combination of a pure machine learning model (the most abstract representation) and experimental data (the least abstract representation) lead to an electrode formulation with objectively better performance. Additionally, the optimal formulation was discovered well outside the convex hull of the original data set, meaning that the chosen method of exploration-biased optimization is a useful tool for stepping beyond the current state of knowledge in a system.

Chapter 3 describes a technique developed to understand the sensitivity of the precipitation model used in Chapter 4 and in the inverse-design framework developed as part of my prior Masters thesis work [84]. The sensitivity test captures both alleatoric and epistemic uncertainty by systematically varying process variables and model parameters. The inverse framework was also extended to include chemical composition as a process variable for optimization. Results from the sensitivity analysis show that the model predictions are incredibly sensitive to variations in interfacial energy and initial supersaturation of the matrix phase. Insights from these results are useful for process engineers in industry making budget decisions about equipment and material researchers trying to determine the most important material properties to characterize and calibrate. Sensitivity and uncertainty analyses of the models used in materials design frameworks is essential for their integration into the overall design process, which is one of the primary goals of the Integrated Computational Materials Engineering group [11].

Chapter 4 focuses on the modeling framework developed in order to help explain differences in the martensitic transformation behavior of Ni-rich NiTi shape memory alloy samples that were additively manufactured under different processing conditions (hatch spacing differed from 120 μm to 35 μm). The project resulted in a unique technique that utilized symmetries inherent to the additive manufacturing process to reduce the computation time of the thermal simulations from 60 days to 12 hours. Reducing the simulation time from hours to weeks was key in making this approach a feasible alternative to experimental synthesis and characterization. Information transfer between the two models is fully automated to enable optimization of processing parameters based on a desired spatial distribution of precipitates. The development of this framework lead to a greater understanding of the interplay between scan strategies and longer-range/lower-temperature physical phenomena such as precipitation. The same framework could be used to study texture evolution if the precipitation model were switched for a grain-growth model.

Chapter 5 focuses on a computational framework that assesses the inherent viability of an alloy for additive manufacturing by predicting the "printable region" of an alloy based on melt pool geometries that are calculated using a finite element thermal model supplemented with a Gaussian

Process regression model. Melt pool geometries are used as indicators due to their well known correlation with melt pool instability issues such as balling, keyholing, and lack of fusion. The project also calculated uncertainty of the boundaries for the predicted region such that the framework could accommodate robust design methodologies that require more complete picture of the response of a system. Furthermore, the thermal model was extended from prior research to include keyhole mode volumetric heating considerations through a modification to the absorptivity and conductivity of the vapor phase. As a whole, this project encompasses almost all of the design aspects mentioned in this introductory section: utilization of three different levels of abstraction (experimental observations, physical models, and machine learning models), assessment and inclusion of important physical phenomena, and a physical model that balances accuracy with speed for potential use within an iterative design framework in the future.

2. DESIGN OF MULTIFUNCTIONAL SUPERCAPACITOR ELECTRODES USING AN INFORMATICS APPROACH

The work in this section was completed as a collaboration with Anish Patel from Dr. Jodie Lutkenhaus' research group. We worked together to research and frame the problem into a design context through many late night conversations and discussions. When it came to the actual contributions from each author, I wrote most (if not all) of the code for the project and Anish performed the synthesis and characterization of the material electrodes. We both analyzed the results together and came to agreements on the appropriate course of action at every stage of the project. The task of writing the actual document was split with each person contributing equally in terms of words written and also thorough technical review of sections.

2.1 Introduction

Currently, much research has gone into improving the energy storage capabilities of promising materials, such as reduced graphene oxide [85, 86, 87, 88, 89], due to growing energy demands. The focus on electrochemical properties ignores other performance metrics of the materials. As a result, current energy storage devices are prone to catastrophic failure [90, 91, 92] and are unfit for flexible or structural electronics. Multifunctional energy storage materials, which can simultaneously deliver energy and bear a mechanical load, are a new way to fabricate flexible, bendable, and structural batteries and supercapacitors [93, 94, 95, 96, 97, 98, 99, 100]. However, there is an inherent tradeoff between electrochemical and mechanical performance for multifunctional composite materials [99, 101, 102, 103]. Wetzel quantified this tradeoff using a multi-functional efficiency, or utility, which is an equally weighted linear combination of mechanical and electrochemical properties [104]. Including mechanical properties as a performance metric for energy storage devices can improve the effective functionality of the overall designed component by providing new opportunities for a wide variety of design cases [99, 100, 105, 106].

Recently, we have studied structural supercapacitors containing reduced graphene oxide (rGO) and Kevlar aramid nanofibers (ANFs) [101, 102]. Reduced graphene oxide, derived from graphene oxide (GO), is a well-studied two-dimensional carbon material that is commonly used in supercapacitors due to its excellent electrical conductivity, high surface area, and good chemical stability [107, 108]. Bulk Kevlar fibers possess a Youngs modulus of 90 GPa and tensile strength of 3.8 GPa making it an ideal additive for enhancing the stiffness and strength of composite materials [109]. ANFs are nanoscale Kevlar fibers formed from the dissolution of the bulk fibers [110]. They are promising building blocks for nanocomposite materials due to their excellent mechanical properties and easy processability. Incorporating ANFs with rGO allows for the nanofibers to act as a mechanically reinforcing nanofiller that also prevents the restacking of graphene sheets [102]. This is due to hydrogen-bonding [111, 112] and aromatic stacking [113, 114] (or $\pi - \pi$ stacking), which lead to strong interactions between the two materials. These interactions result in greatly improved mechanical performance [101, 102, 111, 112]. ANFs have also been shown to improve the mechanical properties in other composites [101, 102, 111, 112, 115, 116, 117, 118].

Carbon nanotubes (CNTs) are of interest here as additives to the graphene/ANF electrode for several reasons. CNTs are rod-like nanoparticles that are well known for their high electrical conductivity and exceptional mechanical performance making them an ideal nanomaterial for composite electrodes [119, 120, 121]. Carbon nanotubes have been used as supercapacitor electrodes [122] but they are more commonly used as an additive to increase the electrochemical performance and/or mechanical capabilities (i.e. flexible electrodes). [123, 124, 125, 126] While graphene is an excellent electrode material for supercapacitors, its propensity to agglomerate and restack significantly impedes electrochemical stability [127, 128]. Therefore, the use of an additive that prevents restacking, such as CNTs, leads to an improvement in electrochemical performance. It has been shown that CNTs act as a conductive bridge between graphene sheets to prevent agglomeration and promote conductive pathways [129, 130]. Carbon nanotubes have also been used in composites with polyaniline [125] and manganese oxide [126] to achieve similar results.

There has been a rapid rise in the use of machine learning in materials science, which has led to the acceleration of the materials discovery process [131, 132, 133, 134, 135, 136, 137, 138, 139]. The need for materials informatics partly arises from the large cost of running experiments when attempting to find optimal compositions. For example, fabricating and fully characterizing one of the aforementioned rGO/ANF electrodes can take up two weeks.18 Materials informatics provides powerful tools that can take advantage of previously generated data to better understand the relationships between processing, properties, and performance in order to predict new materials without the traditional costs associated with experimental work.

Here we refine and re-examine Wetzels utility metric in order to broaden its applicability to a wider design space. By doing so, we present a customizable utility function that allows the user to adjustably weight the electrochemical and the mechanical performance metrics. This utility function guides the design of the electrodes toward different regions of the design space based on the application. The primary degrees of freedom in the material system considered in this work are the weight percentages of the electrode's constituents (rGO/ANFs/CNTs). Herein, we focus on the combination of data science and experiments to establish high-level connections between composition and the electrochemical and mechanical properties. Data driven models, in the form of Gaussian processes, are used to establish links between composition and performance without any knowledge of the complex physical interactions within the electrode. These models are used to predict compositions with promising combinations of properties which are then validated experimentally, within a Bayesian optimization framework. This process is performed multiple times, creating a feedback loop for efficient exploration of the design space. We apply this methodology to the rGO/ANF/CNT supercapacitor system as a test case.

2.2 Methodology

2.2.1 Design Problem

In order for these tools to be combined in an effective way it is necessary to establish a description of the system in terms of functional dependencies. This is first done at the component

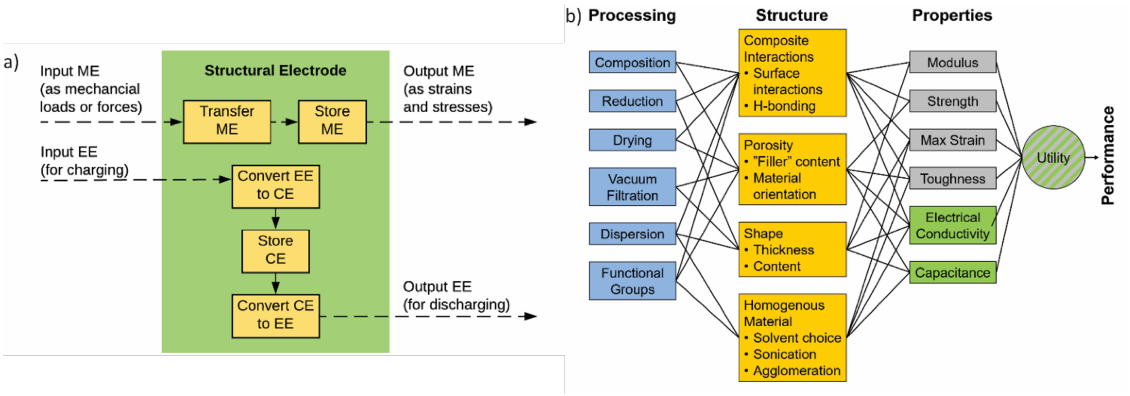

Figure 2.1: (a) Component level functional diagram of a typical structural electrode where ME is mechanical energy, EE is electrical energy, and CE is chemical energy. In this diagram, the structural electrode can discharge electrical energy while also safely handling mechanical loads. (b) Material level system chart of the interactions between process, structure, and properties within a composite electrode consisting of ANFs, graphene, and CNTs.

level to better understand how a structural energy storage device might operate within an overall system. The component level functional model indicates the appropriate performance metrics and properties to consider in the material level functional model. The material level functional model captures relationships between process, structure, properties, and performance in the form of a system chart similar to the type outlined in Olsens report on the design of materials [140]. The material level functional model allows for a fair assessment of how to best combine data, models, and experiments at the appropriate levels of abstraction.

A functional diagram for a structural electrode is used to better understand the relationships between inputs and outputs at the component level, Figure 2.1a. Also, it is used to inform decisions concerning the best way to manipulate functions and sub-functions to achieve objectives and goals. At the component level, Figure 2.1a, the function of a structural electrode is to store and deliver energy to a system while still being safe and stable after sustaining mechanical loads and forces. This requires the consideration of both electrochemical and mechanical requirements [104].

As stated above, the three potential materials of interest for designing a multifunctional energy storage device are graphene, ANFs, and CNTs. The system chart, Figure 2.1b, summarizes the fundamental functional interactions between the various levels of the process-structure-properties

(PSP) hierarchy for composite electrodes that contain these components. For example, composition directly affects composite interactions and porosity of the structure, which, in-turn, affect the electrochemical and mechanical properties listed.

In order to effectively design a new material, the mechanical and electrochemical properties should be combined into a single performance metric (U, which varies from 0 to 1) through a utility function which combines electrochemical utility (ECU) and mechanical utility (MU). Equations 1-3 define the utility based on a combination of various performance metrics where a is a weighting coefficient (which varies from 0 to 1), C is the specific capacitance of the electrode at different scan rates , T is the toughness, σ is the ultimate tensile strength, E is the Youngs modulus, and is the strain at break. These performance metrics were normalized by the typical values for pure reduced graphene oxide electrodes and pure ANF films denoted by subscript *rGO* and subscript *ANF*, respectively. This means that the ternary composite materials are being compared against pure reduced graphene oxide, a commonly investigated material for supercapacitor electrodes, and pure ANF which is known for its mechanical properties. This allows the utility function to reflect the change in performance relative to the highest performing unary component. ECU describes the capacitance values at 6 different scan rates (v = 1, 5, 10, 20, 50, and 100 mV s^{-1}) to take both energy storage and rate capability into account. MU examines 4 important metrics for structural materials and combines them with equal weighting. The value of *a* is chosen to bias the relative importance of electrochemical performance against mechanical performance based on the intended application. For this work, *a* was set to 0.5.

$$U = (1-a)ECU + (a)MU \tag{2.1}$$

$$ECU = \frac{1}{n}\sum_{i=1}^{n}\frac{C_e(sr_i)}{C_{GO}(sr_i)} \tag{2.2}$$

$$MU = \frac{1}{4}\Big[\frac{S_e}{S_{ANF}} + \frac{E_{ANF}}{E_e} + \frac{UTS_e}{UTS_{ANF}} + \frac{T_e}{T_{ANF}}\Big] \tag{2.3}$$

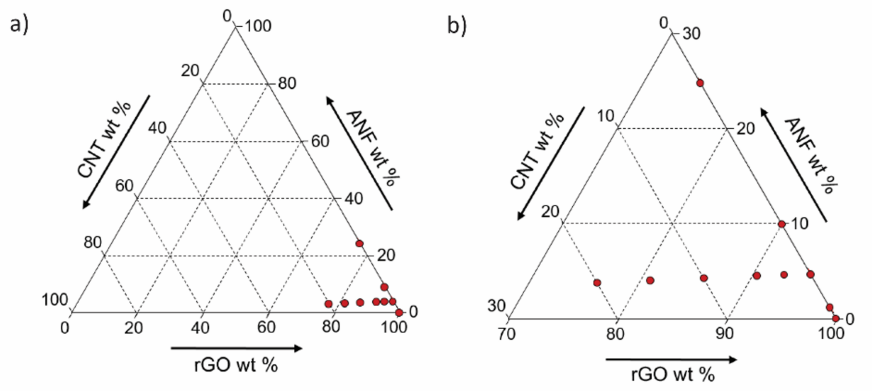

Figure 2.2: Ternary diagram describing the (a) entire design space for rGO/ANF/CNT supercapacitor electrodes and the (b) smaller portion of the design space used in the model. Each point represents a composition already analyzed for electrochemical and mechanical properties.

2.2.2 Model Development

2.2.2.1 Data

High quality data is required to form effective data-driven computational models. The primary source of data for this work is experimental data generated in-house regarding electrochemical and mechanical properties of rGO/ANF/CNT composite electrodes. There are many advantages associated with using this dataset. For example, using a single set of experimental data eliminates many potential confounding features such as processing method, slight variations in characterization techniques, and sample dimensions because many design variables are controlled and held constant. If external sources of data (regarding the raw materials or binary composites) were used, additional features would be needed to properly model the data. This would prevent experimental validation due to lack of appropriate processing equipment.

While using one set of experimental data is beneficial, there are also challenges to this approach. The experimental data available only explores a small portion of the entire design space as shown in Figure 2.2a. This may cause problems in modeling the entire space because the model will have inaccurate predictions away from the data heavy corner. However, it is not necessary to explore the entire design space. Previous work in the area of multifunctional composites show that

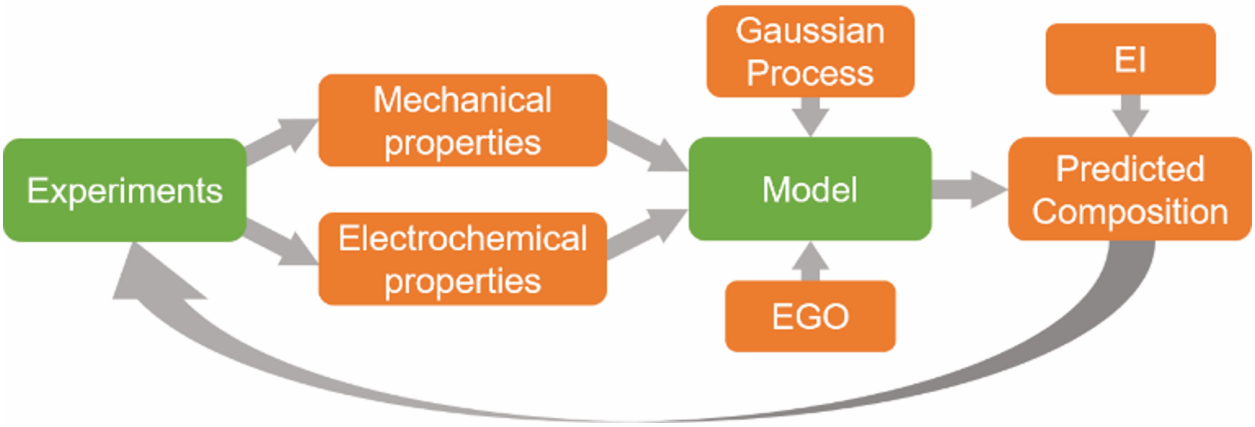

Figure 2.3: Schematic showing feedback between experimental data and the computational model. EI is expected improvement and EGO is efficient global optimization.

using ANFs or CNTs as additives (in small quantities) provides a large enhancement in mechanical and electrochemical performance, respectively [109, 111, 112, 115, 117, 118, 116, 126, 130]. Also, exploring high graphene content composites better tailors this analysis to energy storage applications since graphene acts as the primary electroactive component in the composite. Reducing the design space to consider only high graphene content and low ANF and CNT content will provide the best analysis into multifunctional energy storage devices with the current experimental dataset available. This reduced area is shown in Figure 2.2b.

2.2.2.2 Regression

A model is fit to the experimental data and used to guide future experimental work. These guided experiments are then used to update the model so better predictions can be made in the next iteration. A schematic of this feedback loop is shown in Figure 2.3. This synergistic framework, combining experiments and modeling for the purpose of optimal experimental design, is inspired directly by research which has laid the groundwork for efficient global optimization (EGO) of expensive functions in general [141] and, more recently, in material science [17]. In these works, Gaussian process models (GPMs) are fit to available data and then coupled with an optimality metric called expected improvement (EI) which balances exploration and exploitation of the design space.

In order to effectively create a model from this dataset, appropriate representations of the expected response surface of such a model must be established. GPMs describe the expected behavior of the surface according to the sensitivity of the data to each control variable, and the correlation between points in the design space. Sensitivity and correlation are encoded in a kernel function through the use of hyperparameters which represent the characteristic length and correlation distance of the response surface, respectively. Selection of the kernels functional form (Matern, radial basis functions (RBF), etc.) is often based on the expected nature of the response surface *a priori*. Multiple kernels are tested and compared based on their predicted surfaces. With an appropriate kernel and relevant hyperparameters defined, the GPM is fit to a dataset by finding hyperparameter values that minimize the error between the response surface and the data points. The GPM, with optimized hyperparameters, is then used to predict the mean and variance of the response surface for the entire design space.

Predicted response surfaces of GPMs were then used, in conjunction with a leave-one-out (LOO) cross validation technique, to find the most predictive feature set. Four feature sets (ANF /rGO, ANF /CNTs, rGO /CNT, rGO /ANF /CNT) were analyzed using this technique. In LOO analysis, one point is removed from the dataset and the model is trained on the remaining data. The error of the model is calculated as the difference between the models predicted value and the actual value at the removed point. This process is repeated until all data points have been sampled. Each feature set is analyzed with this approach and the resulting distribution of errors are compared to select the best feature set. A summary of these analyses is given in the Section 2.3.

Once the final GPM and feature set combination is determined, the mean and variance predictions of the model are used with an acquisition criterion to select new potential experiments. The choice of acquisition criteria depends on the objective of the design problem. Since the objective of this work is to optimize the performance of a supercapacitor electrode, criteria that seek the optimum value in a design space were chosen: Upper Confidence Bound (UCB), Probability of Improvement (PI), and Expected Improvement (EI).

UCB, the simplest approach, selects new experimental points by finding the maximum value when the mean and variance surfaces are added together. While easy to calculate, UCB has the drawback of a slow convergence rate if the predicted variance dominates the mean response. PI selects the next experiment by finding the point in the design space that has the largest region of its probability distribution above a predefined target value of the optimization. This target value is typically selected as the best point found so far plus a constant value. The magnitude of this constant term determines the behavior of the search criteria with large values promoting exploration and small values promoting exploitation. The main issue with PI is the need to select this target offset *a priori*. EI extends the idea of PI by including information about the centroid of the same area considered by PI. By using the centroid, EI considers both probability and magnitude of the improvement [142]. This provides a balance between exploration and exploitation in which points that have lower probability but larger magnitudes of improvement can be selected over points with higher probability but lower potential improvement in the response surface. Analysis of these acquisition criteria for this particular design problem can be seen in section 2.3 below.

2.2.3 Experimental

2.2.3.1 Electrode Characterization

Briefly, rGO/ANF/CNT electrodes were fabricated using vacuum filtration of a graphene oxide/ANF/CNT dispersion in dimethyl sulfoxide (DMSO). The electrode was dried and thermally reduced to obtain flexible and free-standing electrodes, Figure 2.4a-c.

The composite electrodes thickness was characterized using scanning electron microscopy (SEM, JEOL JSM-7500F). Average thicknesses of 15-30 μm were obtained. Cross-sectional SEM imaging of the composite revealed a tightly packed and layered structure, Figure 2.4d-e. However, the ANFs and CNTs were not directly observed due to their small size and low loading in the composite. CNTs were characterized using transmission electron microscopy (TEM, JEOL JEN-2010). Samples were prepared by drop casting a solution of CNT in DMSO directly onto a TEM grid.

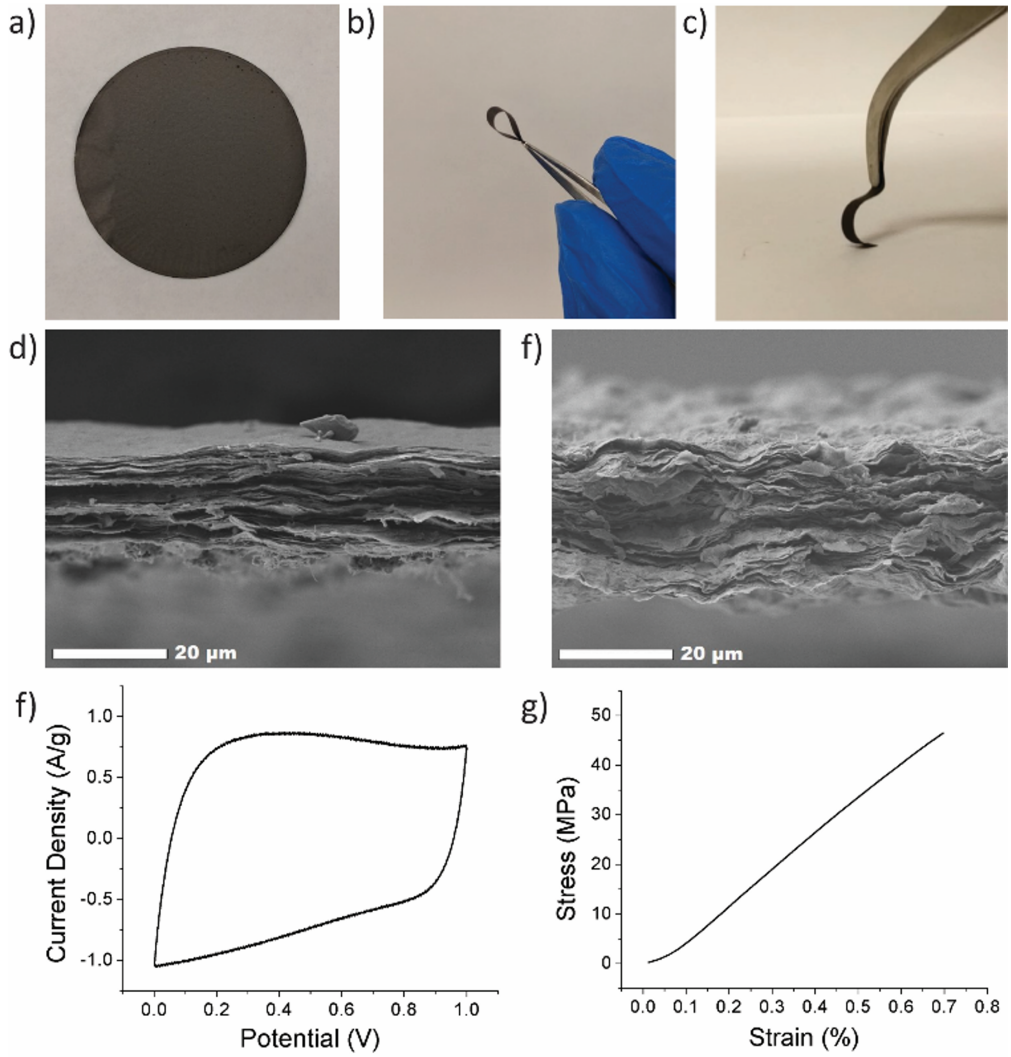

Figure 2.4: Digital images of (a) an rGO electrode and (b-c) an rGO/ANF composite electrode (no CNTs). Cross-sectional SEM images of (d) an rGO/ANF electrode without CNTs (95/5 wt% rGO/ANF) and (e) with 20 wt% CNTs (76/4/20 wt% rGO/ANF/CNTs). (f) A representative cyclic voltammogram and (g) a typical stress-strain curve for an rGO/ANF/CNT composite electrode (90.25 rGO wt%, 4.75 ANF wt%, 5 CNT wt%)

Electrochemical characterization was carried out using cyclic voltammetry (CV) on both a Gamry potentiostat and Arbin instrument (Gamry Interface 1000, Gamry Instruments and Arbin). The electrochemical performance was tested using a two-electrode symmetric coin cell with 6M KOH as the electrolyte. The coin cell consisted of, from bottom to top, a bottom metal covering, carbon paper current collector, electrode, electrolyte, separator (Celgard 3501), electrolyte, electrode, current collector, spacer, spring, and metal covering. The electrodes were prepared by cutting a 16 mm circle sample out of the composite electrode. Cyclic voltammetry was conducted at varying scan rates from a voltage of 0 to 1 V. Specific capacitance (F g^{-1}) was calculated from CV curves using Equation 2.4, where m is the mass of the two electrodes (g), ν is the scan rate (V s^{-1}), V is the voltage range (V), V_l is the low-voltage cutoff (V), V_h is the high-voltage cutoff (V), and I is the current (A). Figure 2.4f shows a CV curve for a rGO/ANF/CNT composite with 90.25 rGO wt%, 4.75 ANF wt%, and 5 CNT wt% at 20 mV s^{-1}. The electrode stores energy through electric double layer (EDL) capacitance. This is evident through the lack of redox peaks in the CV curves and the rectangular shape of the curve, which indicates ideal capacitive behavior.

$$C = \frac{2}{mv\Delta V} \oint_{V_l}^{V_h} I(V)dV \tag{2.4}$$

Mechanical performance was evaluated using quasi-static uniaxial tensile testing using a dynamic mechanical analyser (DMA Q800, TA Instruments). The electrode was cut into rectangular strips approximately 2.5 mm in width, 20 mm in height, and thicknesses ranging from 15 to 30 μm. The electrode samples were gripped using a thin film tension clamp with a clamp compliance of about 0.2 μm N^{-1}, and the tensile tests were conducted in controlled strain rate mode with a preload of 0.02 N and a strain ramp rate of 0.1 % min^{-1}. A typical stress-strain curve of a rGO/ANF/CNT composite with 90.25 rGO wt%, 4.75 ANF wt%, and 5 CNT wt% obtained from tensile testing is shown in Figure 2.4g. Mechanical properties obtained from the stress-strain curve include Youngs modulus, strength, ultimate strain, and toughness.

2.3 Results and Discussion

2.3.1 Feature Selection

Utility for the initial experimental data was calculated using Equations 2.1 with an a value of 0.5, indicating equal weighting of both electrochemical and mechanical utility. The relationship between the three features (rGO wt%, ANF wt%, and CNT wt%) and utility is shown in in Figure 2.5a-c. This shows that the regression model can be used to establish a direct link between composition and performance. The features that were selected all affect the value of utility in a noticeable way. However, a single feature alone cannot explain the utility values and cannot capture the design space. For example, from Figure 2.5c, which focuses on CNT wt% as the single feature, it is evident that multiple samples with 0 wt% CNT have different values of utility and that additional information from other features would be required in order to accurately predict the composites behavior. This can also be seen with ANF wt% as a feature, Figure 2.5b. Feature selection is required to find the best combination of features that can model the design space. Lookman et al. also found that composition dependent features can be used to predict performance and guide experimental exploration of the design space [17, 143].

Feature selection was used to find the most predictive feature set. Four combinations of the three features (ANF/rGO, ANF/CNT, rGO/CNT, rGO/ANF/CNT) were tested using leave-one-out cross validation, as shown in Figure 2.5d. The unary feature sets were disregarded due to their inability to describe complete compositions. Unary feature sets would prevent experimental validation of predicted compositions. Each feature set performed almost identically. The leave-one-out error for the complete feature set (rGO/ANF/CNT) was 19.9 % while the errors for the feature sets ANF/rGO, ANF/CNT, and rGO/CNT were 19.6 %, 20.1 %, and 19.3 %, respectively. The uniformity in errors is expected because all four feature sets contain enough information to define the entire system in terms of composition due to mass conservation constraints. The complete feature set with all three features (rGO wt%, ANF wt%, and CNT wt%) was used as it contained the most information and performed as well as the other feature sets. Analysis of variance (ANOVA) was

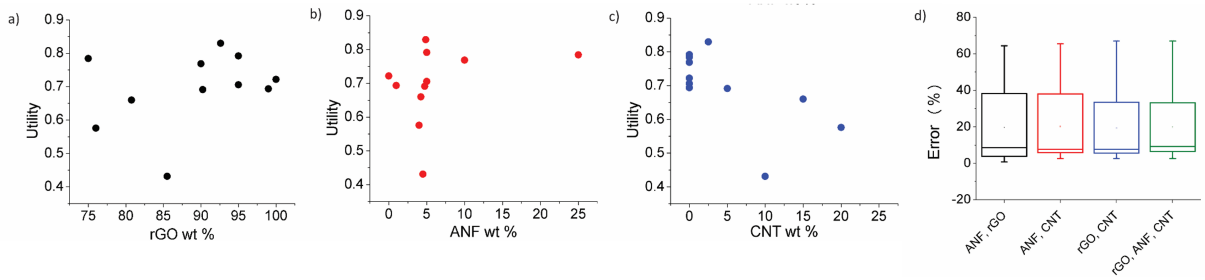

Figure 2.5: Values of utility for the features (a) GO wt%, (b) ANF wt%, and (c) CNT wt% for each experimental data point. (d) Leave-one-out cross validation error of four different feature sets. Boxes are a statistical representation of the distribution of errors for each feature set. The top and bottom line are the maximum and minimum data points, the top and bottom of the box are the 75th and 25th percentile markers, the middle line is the median, and the point within the box is the mean.

used to compare the variance between the 4 feature sets. There was no statistical difference between the errors of the different feature sets meaning the average of the errors of the four feature sets obtained using leave-one-out cross validation are all equal.

2.3.2 Response Surface

After considering multiple kernels, a combination of two RBF kernels with different characteristic length limits were chosen to allow the hyperparameter optimization subroutine to identify multiple characteristic frequencies of the response surface. In other words, using these two RBF kernels allows the response surface and acquisition criteria to balance exploration and exploitation. The two kernels prevent the model from being trapped in local maxima but limits exploration so that potential absolute maxima can be identified properly. A predictive model of the utility, calculated using this kernel, was obtained using the regression techniques described in section 2.2.2.2 and using initial experimental data. Plots of this utility and standard deviation vs. electrode composition are displayed in Figure 2.6 with the design space defined as 0-30 wt% ANF, 0-30 wt% CNT, and 70-100 wt% graphene. The model indicates that the utility is highest for high rGO loading (>95 wt%). However, the model also shows the potential for promising compositions near 80 wt% rGO, 5 wt% ANF, and 15 wt% CNT. This is most likely because high rGO loading will lead

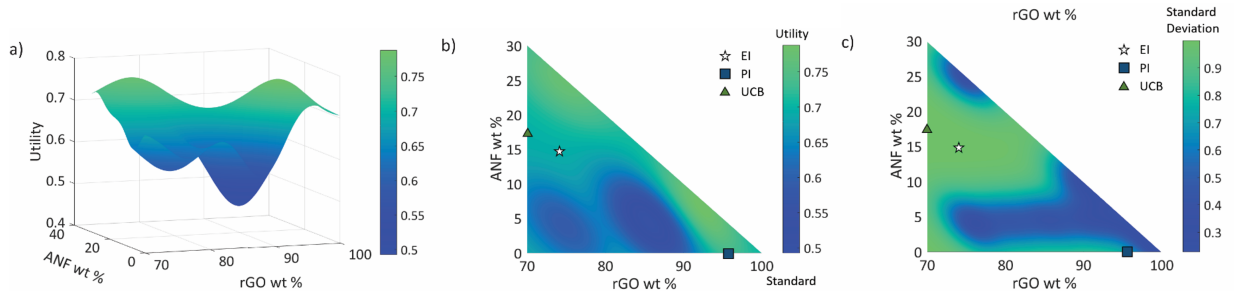

Figure 2.6: Three-dimensional plot of (a) utility, and (b) contour plots of utility and (c) standard deviation vs. composition. Circular points represent initial experimental data while the star, square, and triangle represent recommendations from the model based on either expected improvement (EI), probability of improvement (PI), or upper confidence bound (UCB), respectively.

to high capacitance values as it is the main contributor in the composite due to its high surface area and electrical conductivity. CNTs can also contribute to the capacitance of the electrode while also potentially imparting improved mechanical properties due to strong $\pi - \pi$ interactions between the CNTs, rGO, ANFs. Finally, adding in small amounts of ANF will slightly reduce the specific capacitance of the electrode as it is an electrically insulating material and will not contribute to the capacitance. However, ANFs will greatly improve mechanical properties by strongly associating with the rGO sheets through hydrogen bonding and $\pi - \pi$ stacking.

The three acquisition criteria, expected improvement (EI), probability of improvement (PI), and upper confidence bound (UCB) (white star, blue square, and green triangle, respectively in Figure 2.6b-c) all point to different locations on the utility surface. UCB (green triangle) indicates the point that has the maximum utility value possible when examining both mean and variance, PI (blue square) describes the highest probability of improvement, and EI (white star) takes both the probability and magnitude of improvement into consideration. In this work, EI is selected as the acquisition criteria instead of PI due to its lack of sensitivity to the target offset value. The selection points for PI and UCB are plotted in Figure 2.6b-c along with EI selection points for comparison. Both UCB and EI recommend testing in areas that have high variance, or areas that have not been experimentally probed. This is because the model requires more information across the design space (exploration) before it can begin to search for a maxima (exploitation). PI indi-

cates a composition near the highest experimental utility composition because it possesses a high chance of very minor improvement. The EI predicted optimal composition for the first iteration was 74 wt% rGO, 14.5 wt% ANF, and 11.5 wt% CNT wt%. As shown in Figure 2.3, the predicted composition is synthesized experimentally and mechanical and electrochemical properties are characterized according to the methods described in section 2.2.3.1. The properties of the new composition are then used to update the mean and variance of the utility predictions. This process constitutes one iteration and is repeated to find the composition with the highest utility.

The first iteration was found to have the highest utility of the predicted compositions at U= 0.875 for 74 wt% rGO, 15.5 wt% ANF, and 11.5 wt% CNT, Figure 2.7b. Not only was this the highest predicted utility, it was also higher than the utilities obtained from the initial experimental data. The model was able to find a composition that had a 5.5 % improvement in utility over the best performing composite (92.625 wt% rGO, 4.875 wt% ANF, and 2.5 wt% CNT) from the initial experimental data. The new composition also had Youngs modulus of 18.9 GPa and a strength of 66.3 MPa, which corresponds to an increase of 78.8% and 34.0%, respectively, relative to the highest performing initial experimental composition. However, the capacitance at 1 mV s^{-1} was 117.2 F g^{-1}, representing a 29.6% decrease. This is because the model equally weighs mechanical and electrochemical performance while the initial experimental data prioritized electrochemical performance over mechanical performance due to being focused around high rGO loadings.

The model next explored relatively high ANF content compositions (such as 70 wt% rGO, 22 wt% ANF, and 8 wt% CNT) only to find the utility in those areas to be fairly low. This is due to low surface area of electrically conductive material in the composite resulting from the low rGO content. This caused low capacitance values and poor cycle stability leading to a reduced ECU. The model then recommended relatively high CNT content compositions (such as 70 wt% rGO, 0 wt% ANF, and 30 wt% CNT). While the high CNT content electrodes performed well electrochemically (due to the CNTs contribution to the capacitance), the mechanical properties were found to be low due to the lack of a mechanical nanofiller. This led to reduced interactions between the electrode components and a reduced mechanical utility.

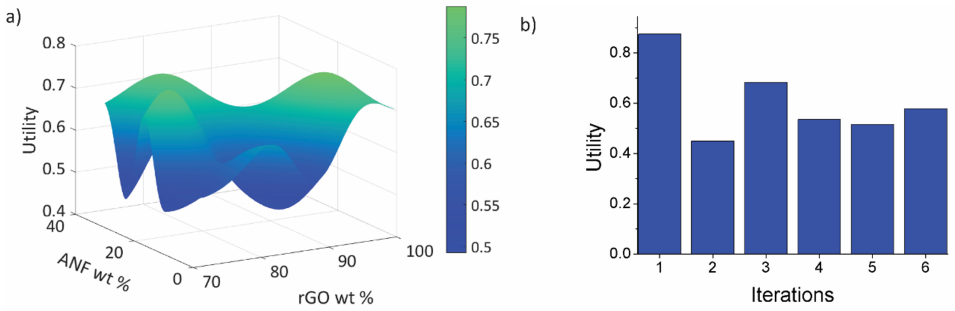

Figure 2.7: (a) Predicted utility function after 6 iterations and (b) utility of samples with composition predicted by EI at each iteration.

After 6 iterations, the utility surface predicted by the model, Figure 2.7a, changed drastically as compared to the predicted utility using only initial experimental data, Figure 2.6a. These results are significant because we were able to find the highest utility composition (74 wt% rGO, 15.5 wt% ANF, and 11.5 wt% CNT) in an area of the design space that would not have been explored as rapidly when using only experimental approaches. The use of materials informatics reduced the number of experiments that would have been required to find this optimal composition when compared to systematically exploring the design space. Furthermore, the model gives additional insight into the tradeoffs between electrochemical and mechanical performance when considering composite materials by predicting maxima and minima in the response surface at certain compositions.

2.4 Conclusions

In summary, functional analysis was used to identify the variables that control the electrochemical and mechanical properties of the composite electrode. With these properties, a utility function was developed for evaluating the performance of the multifunctional material. The utility incorporated material properties such as specific capacitance, strength, Young's modulus, ultimate strain, and toughness. These properties were combined in a weighted fashion to allow for adaptation to user preferences of the electrode's electrochemical or mechanical properties. Next, feature selection, using leave-one-out cross validation, was performed to find the subset of features that

captured the response surface most accurately. From this feature set analysis, a Gaussian process regression model that used rGO wt%, ANF wt%, and CNT wt% as features was selected and fit to the data by tuning the hyperparameters. EI was used as the acquisition method for predicting the next best composition to test experimentally. After 6 iterations, the model identified a maximum in the design space in a previously unexplored area. The model was able to find a composition with higher overall utility (5.5% increase), Youngs modulus (78.8% increase), and strength (34.0% increase) than the best initial experimental composition. This approach can be used to map out the design space in an optimal manner reducing the number of experiments required to find the optimal combination of rGO, ANFs, and CNTs for multifunctional structural energy and power.

3. SENSITIVITY ANALYSES OF A PROCESS PRESCRIPTION FRAMEWORK FOR INTEGRATION WITH ICME DESIGN METHODS

3.1 Introduction

The overall product design process is a complicated iterative task that relies on the effective transfer of information between the various aspects of the components design. The incorporation of materials/manufacturing optimization into this engineering design process is the main goal of the Integrated Computational Materials Engineering (ICME) movement in materials science [11, 10]. To accomplish this, the ICME community focuses on the development of computational material modeling tools that describe the relationships between the various levels of the process-structure-property (PSP) hierarchy. Such relationships in practice focus on the *forward* problem of establishing quantitative relationships along the PSP chain. These descriptive bottom-up models, however, are not goal-oriented and in order to use them in the actual design of materials it is necessary to invert them into *prescriptive* top-down models which allow for the design of materials specific to the applications they will be used in, thereby elevating and expanding the design space of the overall component. More specifically, material design frameworks seek to prescribe microstructures and their particular processing schedules based on desired material properties.

While there are many examples of descriptive and prescriptive models for the link between mechanical properties and microstructure [144, 16, 145], top-down links between microstructure and processing have not been explored extensively. One of the drawbacks of neglecting this important connection is that, often times, the regions in the materials design space that correspond to *optimal* microstructures do not overlap with those corresponding to *feasible* ones. That is, what could be deemed as an optimal configuration of the material system to achieve a specific function may not be attainable through conventional processing schemes. In fact, it has already been recognized in some major studies of the field [146] that one of the areas that needs further attention is the devel-

opment of frameworks capable of connecting *desired* microstructures to the *required* processing steps necessary to achieve them.

Recently, the present authors have tackled an example of such problems by trying to invert the process-(micro)structure relationships in alloy systems modified through secondary solid-state precipitation processes. The core of the framework [84], developed in a previous paper, prescribes the times and temperatures of multi-stage heat treatments necessary to produce desired Ni_4Ti_3 precipitate microstructure in a 52-NiTi [at%] shape memory alloy. Near equi-atomic NiTi-based SMAs are at the core of many research efforts because of their direct applicability as compact and weight-saving actuation mechanisms in biomedical and aerospace designs [147, 148, 7, 149, 150].

Specifically, the previous work linked a thermodynamically- and kineticaly-consistent model for the precipitation of secondary phases out of a matrix accounting for nucleation, growth and coarsening of the secondary phases with a black-box optimization framework finding the process parameter region (in the two-stage four-dimensional temperature-time space) leading to a target precipitate distribution. While the framework was shown to produce solutions to the *inverse* process-structure problem, it was limited in that it did not account for the *uncertainty* in the inputs to the models linking temperature-time histories to precipitate size distributions nor properly scoped the available process design space as it focused on a fixed initial composition of the matrix.

This paper addresses these two issues by adding the initial alloy composition as a design variable and by performing a sensitivity analysis linking the inputs and outputs of the process model. The addition of initial alloy composition as a design variable will allow for the model to be applied to a broader range of potential applications as it expands the design space. The sensitivity analysis, on the other hand, provides the material scientist and process engineer a better sense of how robust the model is and which variables and parameters are the most important. This type of quantification is very useful for real world engineering applications and is cited as one of the key issues facing the ICME community [151, 152, 15, 146]. In addition to the quantitative benefit typically associated with sensitivity analysis results, there is also a qualitative benefit associated with their use as an interdisciplinary communication tool. This communication aspect is something that is

essential to creating effective teams in an ICME setting and will be discussed in more detail in the sensitivity analysis section of the paper.

The main body of this paper is split into two sections. The first section describes the prescription framework used to establish the top-down link between structure and processing and second section describes the thought process and methodology of the sensitivity analysis taken in this research. After the main body, the paper is wrapped up with a results & conclusions section that contains an analysis and discussion of outputs of the sensitivity analysis for a representative problem.

3.2 Prescription Framework

To understand the framework described in this section, it is important to understand the thought process behind establishing a top-down relationship in the process-structure-property hierarchy. The first step is establish a forward (descriptive) model that can accurately calculate outputs when given the appropriate inputs. After that descriptive model is established, it must be inverted so that inputs can be calculated from given outputs. If there is a 1:1 analytical solution that describes the relationship, it is possible to mathematically invert the equations. Unfortunately, this is almost never the case in physics-based material models since the outputs of those models cannot be calculated without knowledge of the initial conditions. In fact, the initial conditions (i.e. model inputs) are what the top-down design approach is meant to find in the first place. A popular approach to overcome this issue is to iteratively evaluate the forward model with varying initial conditions until the correct set of values is found. The usefulness of this iterative approach is reliant on two other concepts: developing a way to efficiently select initial guesses, and finding model outputs (i.e. figure(s)-of-merit) that accurately represent the validity of the input values. In the prescriptive framework described below, an NKW precipitation model is used as the forward model, a Mesh Adapted Direct Search (MADS) based optimization tool is the initial guess selector, and the precipitate size distribution is the figure-of-merit (FOM). An illustration of how information and variables are passed through this system can be seen in Figure 3.1 below.

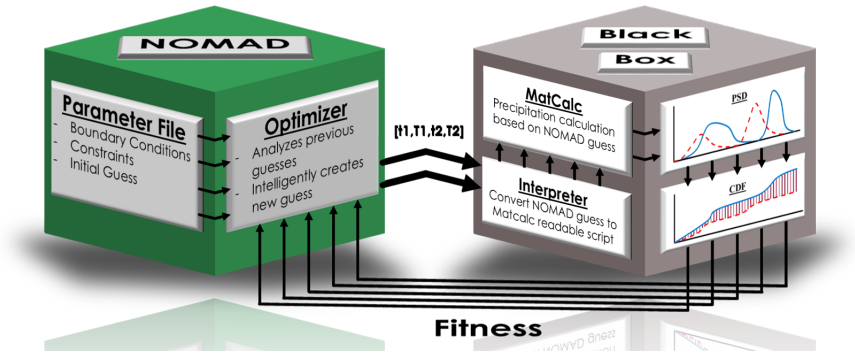

Figure 3.1: Workflow overview of the iterative framework used to prescribe thermal processing. The optimizer *Nomad* [153] sends a guess through an interpreter to MatCalc which calculates the resulting size distribution of particles. That distribution is then compared to a target distribution and the fitness value is returned to *Nomad* which analyzes that value in order to make an educated guess for the set of input variables in the next iteration. This process is continued until a set of inputs that result in a fitness value below a user defined threshold is found.

The basics underlying theories and assumptions of each of these framework components will be described throughout the rest of this section. Readers interested in more in-depth descriptions of each component are directed here [84].

3.2.1 Precipitation Model

As mentioned above, the material model in this prescription framework focuses on the process-structure portion of the PSP hierarchy. More specifically, the framework uses a microstructural modeling tool called MatCalc that links process to structure through the description of precipitate evolution [154]. MatCalc is based upon the Numerical Kampmann Wagner (NKW) model which represents the precipitates in a representative volume as a discrete distribution based on precipitate sizes. The evolution of the distribution is governed by equations describing the nucleation, growth and coarsening evaluated for each size class at every time time step. The assumptions and theory behind the equations for these three stages of precipitate evolution will now be discussed. For a more detailed explanation of the principles behind the equations shown below, the interested reader is referred to [155, 84].

In this model, nucleation is described by the transient nucleation rate defined by classical nucleation theory and shown in Equation 3.1.

$$J = NZ\beta^* e^{\frac{-G^*}{k_B T}} e^{\frac{-\tau}{t}} \tag{3.1}$$

This equation includes thermodynamic terms like interfacial energy as well as kinetic terms like the Zeldovich Factor which accounts for the curvature of the Gibbs energy nucleation barrier and its effect on the atomic attachment rate. Growth in the system is governed by the SFFK multicomponent model which is based on the Thermodynamic Extremal Principle which states that systems tend to evolve along the path of maximum entropy production. The set of equations governing this model consist of a Gibbs energy equation G and three dissipative equations, Q_1, Q_2, and Q_3.

$$G = \sum_{i=1}^{n} N_{0i}\mu_{0i} + \sum_{k=1}^{m} \frac{4\pi\rho_k^3}{3}\left(\lambda_k + \sum_{i=1}^{n} c_{ki}\mu_{ki}\right) + \sum_{k=1}^{m} 4\pi\rho_k^2\gamma_k \tag{3.2}$$

$$Q_1 = \sum_{k=1}^{m} \frac{4\pi\rho_k^2}{M_k^{IF}}\dot{\rho}_k^2 \tag{3.3}$$

$$Q_2 = \sum_{k=1}^{m}\sum_{i=1}^{n} \frac{4\pi RT\rho_k^5\dot{c}_{ki}^2}{45c_{ki}D_{ki}} \tag{3.4}$$

$$Q_3 = \sum_{k=1}^{m}\sum_{i=1}^{n} \frac{4\pi RT\rho_k^3(\dot{\rho}_k(c_{ki} - c_{0i}) + \frac{\rho_k\dot{c}_{ki}}{3})^2}{c_{0i}D_{0i}} \tag{3.5}$$

The Gibbs equation (Equation 3.2) uses precipitate radius and concentrations of both the matrix and precipitate phases to calculate energy contributions from the chemical energy of the matrix and precipitate phases as well as the energy of the surface between them. The three dissipative equations describe the energy losses due to interface propagation Q_1, diffusion in the precipitates Q_2, and diffusion within the matrix phase Q_3. These equations are combined into a linear system of equations by taking the derivatives of G with respect to c_{ki}, ρ_k and $Q_{1,2,3}$ with respect to $\dot{c_{ki}}$,

ρ_k. Stoichiometric constraints due to crystallographic ordering can also be added to the system of equations through the use of Lagrange multipliers.

Coarsening is accounted for by calculating a critical radius of dissolution for the system at each time step with the equation:

$$r^*(t) = r_0^* \left[1 + \frac{t}{\tau_D} \right]^{\frac{1}{3}} \tag{3.6}$$

$$where : \tau_D = \gamma_D \left[\frac{(c_B^\beta - c_B^\alpha) RT}{2\gamma c_B^\alpha D_B^\alpha v^\beta} \right] r_0^{*3} \tag{3.7}$$

If a size class falls below this critical radius r_*, the precipitates of that class are dissolved and the solute is added back into the system, allowing the larger precipitates to grow larger, thereby simulating the Gibbs-Thompson effect. Although the equations for r_* and τ_D above stem from the general LSW theory of particle coarsening, any of the modified version of this equation can be used to more accurately model the needs of specific material systems [155].

Incorporating the governing equations above into an NKW model results in a fully defined precipitaton model which describes the three main stages of precipitate evolution. Details of this NKW model are beyond the scope of this paper, but more information can be found at [155]. Now that a material model describing precipitate size distribution evolution as a function of processing conditions like time and temperature has been properly defined, the next step is to invert this model by finding a way to efficiently select these input parameters (i.e. processing steps). In other words, an appropriate optimization algorithm for this design space must be established.

3.2.2 Mesh Adaptive Direct Search (MADS)

Most optimization algorithms can be classified into gradient based and non-gradient based approaches. Selection of an appropriate optimization algorithm for a particular problem depends on the nature of the model and solution that is being optimized. As described in the general description of this materials design framework, it is not possible to have gradient knowledge of the solution space a priori which therefore limits the available options to non-gradient based algorithms. This

framework uses a non-gradient optimization algorithm called Mesh Adaptive Direct Search as implemented in the NOMAD library [153]. This algorithm fits well within this framework because it doesnt require any gradient knowledge and, in fact, treats the model (i.e. MatCalc) as a black box. The question remains: how does a black box optimization algorithm find the most optimal output of a model it knows nothing about?

Mesh Adaptive Direct Search does this by systematically gaining knowledge about the local solution space through evaluations of the black-box model at discrete points surrounding the current point. Once the evaluations are done, the most optimal point is selected and the next iteration begins with a new search centered around new point. In between each iteration, MADS style algorithms refine or expand the grid of local search points based on knowledge of the search space gained during the previous iterations of the algorithm. This process of selection, evaluation, and mesh refinement is performed iteratively until a predefined stopping criteria is met, which is often based on either a threshold solution value or lack of difference in model evaluations during the local search. For more information about the inner workings of NOMAD and its implementation in this framework, the interested reader is directed toward [156, 157, 84], respectively. The following section discusses the physical significance of the inputs and outputs used to to interface the NOMAD search algorithm with the MatCalc material model.

3.2.3 Interfacing Material Model and Optimization Algorithm

Non-gradient based optimization algorithms need a way to interface with the model that can effectively capture the underlying physical relationships between model inputs and outputs (i.e. process and structure). This section discusses the theory behind the selection of those representative input and output values. Finding appropriate output values is often much more challenging and as such is discussed in much more detail.

3.2.3.1 Figure-of-Merit

In a materials design framework like the one described here, the figure-of-merit (FOM) serves as the common language between the material model and the optimization algorithm. In other

words, it is a mapping from the physical properties of the material model outputs into a numerical value that is interpretable by the algorithm. The most common mapping approach is to simply use single-valued output variables that are representative of the material properties being optimized. This is sufficient in most cases, but can lead to degenerate solution spaces if the output variables dont completely describe the underlying physical phenomena. For example, if the FOM in this framework was based solely on precipitate phase fraction, there would be a near infinite number of appropriate solutions since so many different processing pathways can result in the same singular value for that physical property. This degeneracy can be reduced by combining multiple single-valued outputs into a representative vector (e.g. [phase fraction, average radius]), but this doesnt eliminate the issue completely.

For this framework, a more robust FOM based on the precipitate size distribution output of the model was developed. Representing physical features as distributions is a more complete and physically realistic mapping technique that reduces degeneracy of the solution space [84]. In certain systems, the distribution representations of the system also encapsulate the single-valued features of less descriptive output features sets. This can be illustrated using the volume fraction example from the previous paragraph. The two single value metrics, average radius and volume fraction, are represented by the statistical mean and integrated area of a precipitate size distribution, respectively [84]. Now that an appropriate FOM has been established, the task of defining model input values can be discussed.

3.2.3.2 Extending the Model

As mentioned earlier, the overarching goal of the top-down prescription framework is to discover values of input variables that will result in previously defined outputs. It is at this point that the process variables to be designed/prescribed are encoded into the framework as inputs of the material model. In a previous paper, model inputs representing a two stage heat treatment were encoded as a vector of two times and two temperatures [t1, T1, t2, T2]. The framework was then used to prescribe the values of [t1, T1, t2, T2] which would result in the desired microstructural features. In this current research, the four element input vector mentioned above is extended with

an additional term representing the initial chemical composition of the material [t1, T1, t2, T2, Ni]. The addition of this extra input means that the framework has additional design freedom when prescribing the processing steps required to produce a desired microstructure.

Increasing the design space of a framework in this way allows it to be applied to a wider range of more realistic design problems. Unfortunately, increasing the complexity of the framework makes it harder to understand the relationships between the inputs and outputs of the model. If one wants to achieve the main ICME goal of complete material design integration, these relationships need to be understood in a fairly rigorous way so that any sensitivities in the material model can be accounted for in the overall uncertainty used to design the component. A method to uncover and illustrate these sensitivity relationships is discussed in the following section.

3.3 Sensitivity Framework

Now that the prescriptive framework has been established for linking structure to processing, the focus of the discussion will now shift toward describing an approach for quantifying the sensitivity of the framework. Although applied to this specific framework, the technique detailed below is material and model agnostic so it should be applicable to any model used in a top-down prescriptive design framework. This section begins with a brief discussion of the role of sensitivity analysis in ICME applications, followed by a description of the issues faced when using said techniques to analyze inverse frameworks. After that, the approach developed for this specific framework is described.

In a broad sense, the goal of most sensitivity analyses is to quantify how small changes in individual inputs of a model affect the values of its outputs. This type of analysis is an essential step for full ICME integration of material models because its results inform design and research decisions made within design teams in the overall design process. For example, expected variations in physical properties are incredibly important when developing safety tolerances for mechanical components. Likewise, the sensitivity analysis results can help process engineering teams identify which material processing steps are most critical in the manufacturing process, allowing them to allocate portions of their budget in a more cost effective manner. In an academic setting, decisions

about which characterization experiments to perform can be made easier by analyzing which model calibration parameters create the largest variability in relevant model outputs.

One often overlooked benefit of sensitivity analysis results is their use as a communication tool that essentially summarizes the complex behavior of the model as a direct mapping from input design space to output solution space. This input/output mapping is particularly useful in the multi-scale multi-component design processes encountered in ICME-based frameworks that incorporate many individual design components with their own inputs, outputs, and uncertainties which affect the final overall design. In addition to the basic necessity of quantifying overall design uncertainty, SA results can also be used as a qualitative talking point which enhances communication between subteams in the design process by providing a common language. Bridging the knowledge gap between disciplines is an issue which is ubiquitous within all multi-disciplinary projects. In order to be a good common language in an ICME design context SA results should do three main things: i) group inputs according to their sources of uncertainty, ii) effectively capture the lack of knowledge about the system, and iii) visually represent input/output relationships in an easy to understand format. The details of how this particular sensitivity analysis addresses these three goals are addressed in the following sections of the paper.

Since the framework in this paper centers around a precipitation model, it makes sense to group relevant inputs into model parameters and process variables. These two input variable groups were chosen because of their relevance to two major teams involved in the design process: R&D engineering, and process engineering. As for model outputs, characteristic variables such as volume fraction transformed, mean precipitate diameter, and matrix Ni content were chosen because of their relevance to the overall design process in terms of mechanical and phase transformation properties.

Although, the basic theory behind the precipitation model is presented in the previous section, exact form of those equations inside MatCalc is unknown. This means that the material model is essentially a black box with no analytical gradient information available. Additionally, no uncertainty information is available for either the model parameter inputs or process variable inputs.

Lack of knowledge in these key areas can be overcome by using a non-gradient based sensitivity analysis technique and by calculating the sensitivity of the model over a wide range of input uncertainties. The rest of this section will describe the details of how the analysis was performed.

Monte Carlo (MC) based non-gradient approaches to sensitivity analysis sample a predetermined distribution of values representing the assumed uncertainty of an input variable. The model is then run with these sampled input values and the output variable values are recorded and summarized a corresponding distribution. The shape and size of each output variable distributions is an indication of that outputs sensitivity to the sampled input. For example, in a sensitivity analysis of the overall top-down framework above, an MC technique would vary the precipitate size distribution (input) and record the resulting thermo-chemical process (output). However, MC based sensitivity analysis of the entire design framework is extremely time intensive due to the fact that the evaluation of each MC sample point requires hundreds of forward material model evaluations. Since the material model is the key source of uncertainty in the framework, computational costs can be reduced by analyzing the forward material model alone. This approach only requires one evaluation per MC sample point and should produce similar results to the top-down approach with the only difference being that the labels of inputs and outputs are inverted. This is consistent with the idea that sensitivity analyses are essentially wrappers which create a mapping of inputs and outputs for a model. In this case, the analysis is still mapping characteristic microstructural features to process variables and material model parameters.

Since the uncertainty in each input value is unknown, multiple MC analyses are performed with systematically increasing variance in the assumed input value distributions. The sensitivity to each individual input is analyzed by performing 10 separate MC sensitivity analyses with a systematically increasing width representing an assumed percentage uncertainty in the input variable/parameter. To further increase the computational efficiency, results from previous MC analyses with lesser width are incorporated into the current MC analysis of that variable and new input values are only taken from the range of input values not sampled by the prior MC analyses. A schematic of this sampling strategy is shown in Figure 3.2a.

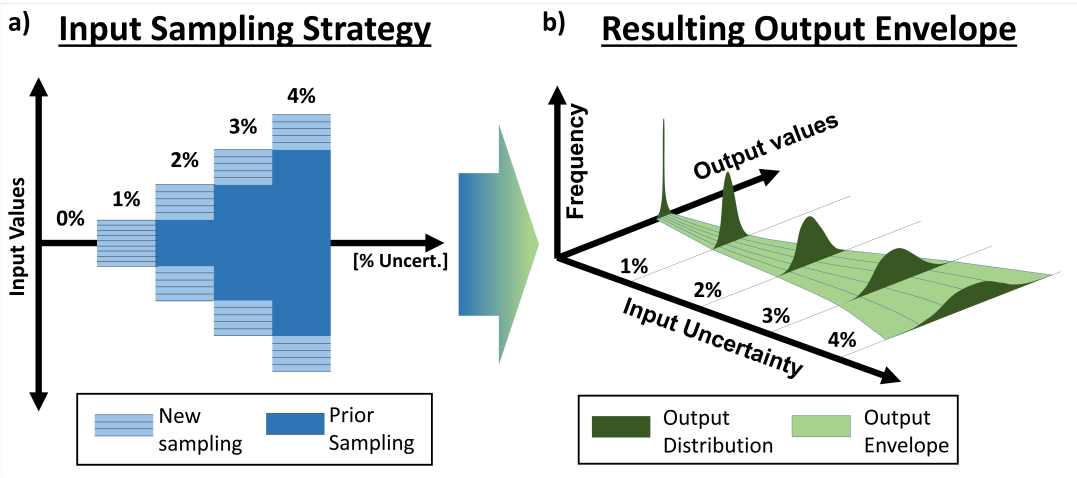

Figure 3.2: Strategy used to create output envelopes of uncertainty based on input distribution sampling. a) Input values are sampled at multiple input error percentages. To increase computational efficiency, input values are only sampled from range of values not covered by previous input value range (light blue boxes). b) The upper and lower limits of each output variable's distribution are plotted as a function input uncertainty to create an envelope of uncertainty for that output variable.

The resulting output distributions from each of these MC analyses is then characterized and the maximum and minimum output values corresponding to a 95% confidence interval are recorded. The resulting 20 output values (10 maximum and 10 minimum values) are then plotted as a function of percent uncertainty in the input value. Since these 20 values represent the upper and lower bounds of the expected output values, the area between them is filled, creating an "envelope of expected values", as seen in Figure 3.2b.

This sampling and envelope creation process is repeated for each input-output combination separately. All envelopes are then grouped together based on output variable so that the effect of each input can be graphically compared. Combined grids of plots showing every output uncertainty envelope grouped by model parameter or process variable can be seen in Figures 3.3 and 3.4, respectively.

This input sampling and envelope creation process is repeated for each input-output combination separately. Figures 3.3 and 3.4 in the results section show model parameter and process

variable envelopes, respectively. Within each figure, the envelopes of uncertainty are grouped according to output variable so that the effect of input values can be compared for every output separately.

3.4 Results and Discussion

This section contains plots showing the envelopes of uncertainty which are created for each input-output combination separately and then grouped into two large groups corresponding to model parameters (Figure 3.3) and process variables (Figure 3.4). Within each figure, the envelopes are grouped and plotted together according to characteristic microstructural feature.

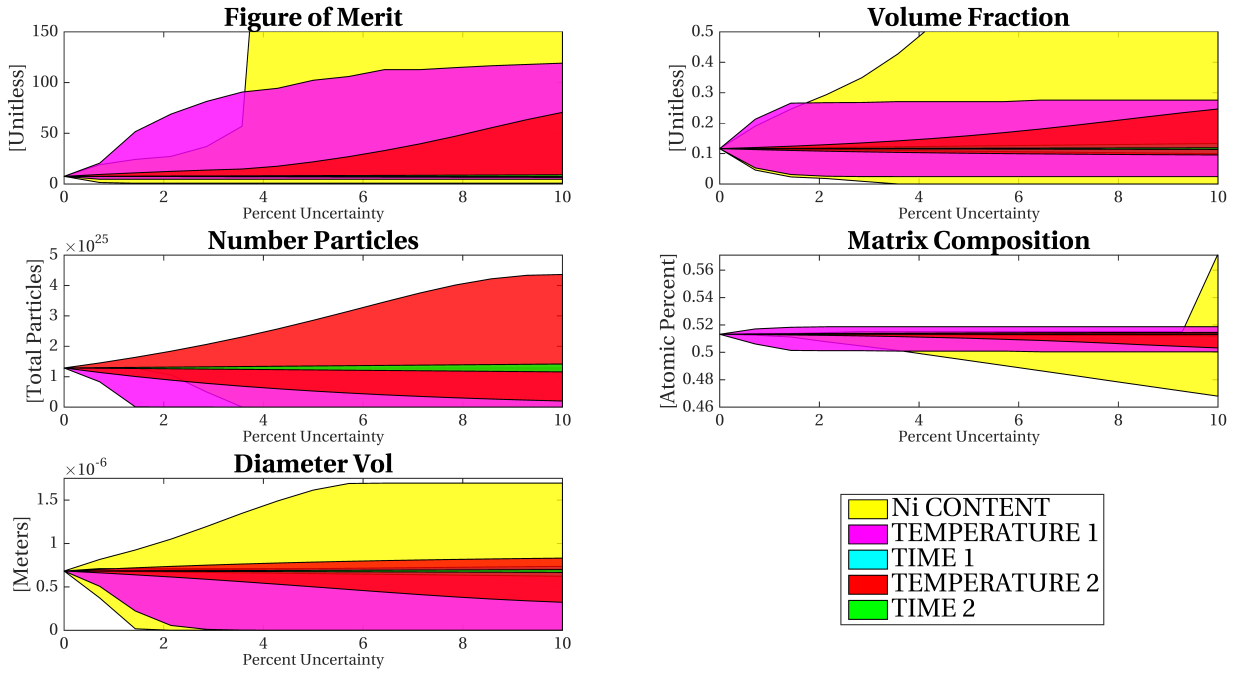

Figure 3.3: Envelope of uncertainty plots showing the expected spread of output values for varying degrees of uncertainty in each *process variable*.

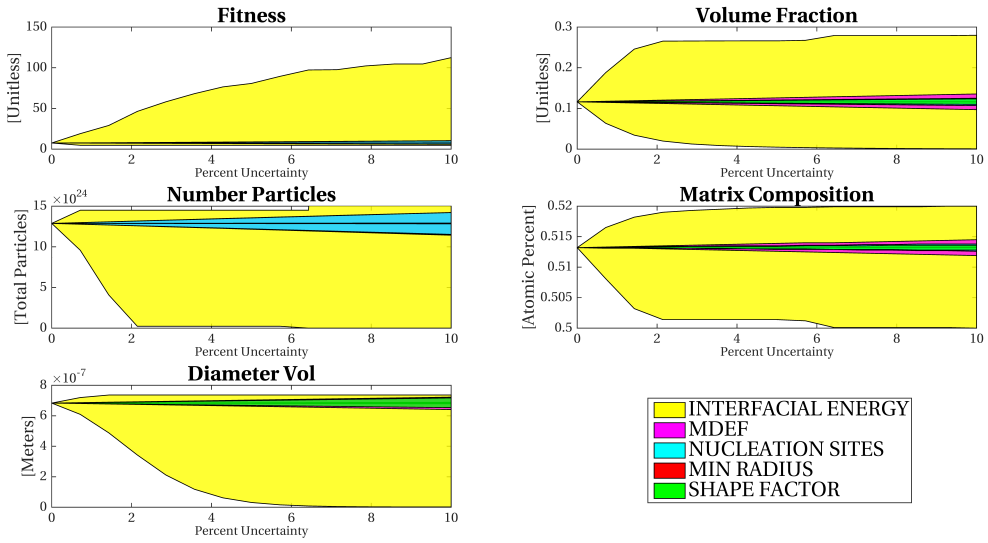

Figure 3.4: Envelope of uncertainty plots showing the expected spread of output values for varying degrees of uncertainty in each *model parameter*.

The sizes and shapes of the envelopes in each plot show which model parameters and process variables have the most influence. Figure 3.4 clearly shows that interfacial energy is the most influential model parameter while Figure 3.3 shows that initial Ni content is the most influential process variable. It can be argued that nominal Ni content and interfacial energy are the most influential inputs because they influence the initial state and early stages of the process dependent microstructural evolution model. This trend of earlier stage process variables being more influential can also be seen by the fact that the first stage time (t_1) and temperature (T_1) typically have the next largest envelopes in relation to nominal Ni content, followed finally by the later stage time (t_2) and temperature (T_2). As with differential equations governing the microstructural evolution models, the initial conditions and earlier stages have a larger effect on the overall outcome of the simulation.

This emphasis on earlier stages of the precipitation process makes sense in systems with irreversible phase transformations since one cannot easily reverse the process to recover from a processing step that takes the system to a region of the design space that severely limits the ability to reach the final desired microstructure. For example, if a NiTi system is subject to a precipitation heat treatment that reduces the Ni content matrix composition below the desired value, the system

will have to be heated to a solutionizing temperature to dissolve some of the Ni_4Ti_3 precipitates, a process which is costly, inefficient, and outside any reasonable temperature bounds that would be set for a precipitation simulation.

More information than just the most influential terms can be gathered from these plots as well. The shapes of the envelopes indicate what threshold percentage uncertainty is required to keep any or all of the output values within a certain range. In other words, the largest x-axis value that corresponds to a user-defined acceptable range of output envelope values is the maximum allowable uncertainty in that input value.

3.5 Conclusions

In this paper, weve expanded the capabilities of a previously published material design framework and conducted a sensitivity analysis of the material model on which the framework is based. The overarching of this work was to make the framework more suitable for use in an ICME-style design context through the introduction of more design variables and a characterization of the uncertainties inherent to the model. The design variables available to the precipitation controlled NiTi shape memory alloy framework now include times and temperatures of two isothermal heat treatment stages as well as the initial chemical composition of the material [t1, T1, t2, T2, Ni].

The sensitivity analysis portion of the paper focuses on characterizing output uncertainty for a wide range of input uncertainty since the inverse design nature of the process imposes a lack of prior knowledge of input uncertainties. The sensitivity framework described here effectively quantifies the effect of thermo-chemical process variability on the resulting microstructural features, opening the door for material design considerations to be considered during safety factor calculations in the overall component design process. This ultimately leads to a higher-dimensional design space for the component allowing for the possibility of even more optimal solutions to be reached through co-optimized mechanical and material design. In addition to the quantitative benefits of the sensitivity analysis, the envelope-of-uncertainty style results shown here provide qualitative visual talking points to promote communication with other disciplines, an essential piece of the ICME puzzle.

4. PREDICTING SPATIAL VARIATIONS OF PRECIPITATES IN METAL ADDITIVE MANUFACTURING USING A SYMMETRY-ENHANCED FINITE ELEMENT THERMAL MODEL

4.1 Introduction

Laser powder bed fusion additive manufacturing (L-PBF AM) is a complicated process during which the processed material undergoes extreme physical transformations, conditions, and gradients relative to traditional manufacturing techniques. For example, the cooling rates near the laser-powder interface (commonly known as the melt pool) are incredibly fast, and each location within the fabricated part will typically experience these extreme transient conditions multiple times as the laser successively passes over and adjacent to that location throughout the course of the build. These rapid cooling rates and multiple thermal cycles lead to very complicated thermal histories, which in turn affect local microstructure and result in spatial variations in material properties throughout the fabricated part. Many research efforts have focused on mitigating these variations, since engineering applications traditionally call for parts with isotropic material properties [158, 30, 69, 159, 160, 161]. One possible alternative is to embrace the spatial variation as a new degree of freedom for engineers and manufacturers to utilize in the design process [32, 31].

For instance, a recent study reports that local control in manufacturing processing parameters during L-PBF, such as the laser hatch distance, can be leveraged to spatially modulate and tailor shape memory effect in as-built nickel-titanium shape memory alloy parts [158, 29, 162]. The $Ni_{50.9}Ti_{49.1}$ (at.%) alloy in those studies (and the current one) was originally selected since the extreme sensitivity of its transformation behavior to minute changes in microstructure and composition made it an ideal platform to investigate the variability in process conditions and (resulting) microstructures and properties during metals AM. The extreme sensitivity of NiTi to process variation was thus the leverage used to demonstrate the spatial control of functional behavior in AM.

While our previous work demonstrated the potential to control the behavior of NiTi-based SMAs on a location-by-location basis, there is still considerable work that must be carried out if one is to leverage this to design additive manufacturable active components with location-based functionality. Indeed, in order to use this spatial control of properties in a design context we need to create models that can predict and explore the effects of process parameters on transformation properties throughout the entire part. Knowledge gained from these computational methodologies can in-turn be used to predict and guide new experiments toward more optimal designs, locally, or other interesting areas of the design space, globally. This computational-experimental coupling accelerates the overall materials design process and is in line with the goals of both the Integrated Computational Materials Engineering (ICME) and Materials Genome (MGI) initiatives. The research detailed in this paper establishes the forward (bottom-up) link between process and microstructure through coupling 3D simulation results of a finite element-based thermal model to a precipitation model that predicts values of characteristic microstructural features, like phase fraction, at discrete points throughout the part.

The finite element thermal model is implemented in COMSOL Multiphysics, and its simulations were validated through comparisons with experimental temperature measurements using in-situ pyrometry and SEM characterization of single-track melt pool cross sections in the same method as shown in [163]. Parameters of the precipitation model, on the other hand, were calibrated for a range of different heat treatments through a Bayesian calibration framework which used Ni content of the matrix as a comparative metric between the model and experiments [18, 164].

In coupling the two models, the key challenge is to overcome the computational burden associated with performing finite element simulations at the level of detail required for accurate and meaningful results from the precipitation model. The kinetically active temperature range of the Ni_4Ti_3 precipitates in which we are interested is approximately 300-700 [°C] [165, 60], which implies that most of the meaningful precipitation will occur multiple microns (and therefore processing layers) beneath the top surface of the material being processed, and will depend on the

processing of every single layer above it. Clearly, modeling multiple laser tracks throughout multiple layers of material is extremely difficulty and time consuming. This is further exacerbated by the fact that the sharp thermal gradients near the melt pool require very fine element meshing to ensure accurate results.

While it is common practice to address this challenge by applying a mirror symmetry operation on the vertical plane that coincides with the laser track, this type of symmetry can only be applied to single track simulations because multiple successive tracks violate the mirror-plane symmetry about the melt pool. Recent work by Wei et. al. [64] demonstrates a method of stamping steady-state simulation results into multiple layer for the purpose of predicting solidification structure in the build direction. In contrast, this paper presents a technique whereby multiple non-mirror-plane symmetry operations are applied to 3-dimensional transient simulation results from a small representative domain to construct the full thermal history of a much larger domain. With this new technique, finite element simulations of just a few laser tracks in a single layer can be extended to a domain consisting of multiple layers and multiple laser tracks within each layer. This full domain is commensurate with a representative volume of a material subject to non-trivial AM fabrication protocols.

Details of these symmetry operations and the FEM simulations to which they are applied are provided in the beginning of the methodology section of the paper. After the larger domain with full thermal histories has been established, the methodology section presents a brief discussion of the precipitation model, followed by a description of how it is applied at discrete points throughout the full domain. The results section consists of precipitation predictions from the coupled models for two sets of processing parameters used in [158, 29]. These two sets of results are then compared and analyzed in the context of the experimentally determined transformation behavior detailed in those papers.

4.2 Methodology

For the framework proposed in this paper, a finite element based thermal model (FEM) is coupled to a precipitation model to predict the spatial distribution of precipitates throughout a the-

oretical build volume. With precipitation prediction in mind, we can estimate the computational time necessary to accurately capture the complex thermal histories that occur in an as-built part. All discussions of simulation times apply to calculations performed on a 20-core compute node within the Ada Supercomputing Cluster located at Texas A&M University. The node consists of two 10-core Intel Xeon 2.5GHz E5-2670 v2 processors linked via FDR-10 Infiniband interconnections. As a representative example, it takes approximately 5 days for the current FEM to simulate a single build layer consisting of 23 laser passes (or hatches) within a 2.83mm x 2.83mm x 0.5mm domain. The precipitation temperature regime of Ni_4Ti_3 (300-700 [°C]) occurs at a depth of approximately 150μm, meaning that at least five 30μm build layers need to be simulated. Hence, this multi-layer simulation would take at 25 days. Obviously, a 25 day simulation is not feasible, but symmetries of the domain can be leveraged to reduce the simulation wall-time to less than 1 day. This approach is inspired by the mirror-plane symmetry operations applied to the centerlines of single track simulations, but uses more complicated symmetry operations like glide planes and n-fold rotations more often found crystallography and first-principles calculations [166, 167, 168].

4.2.1 Representative Domain

Before the symmetry operations can be applied, we first need to define the smaller representative domain to which these symmetry operations will be applied. This involves defining details of this domain including its shape and size, boundary conditions, meshing techniques, and the relevant physics within the domain and at the boundaries. The schematic in Figure 4.1 shows the 5.0mm x 1.0mm rectangular domain that is divided into a 30μm thick powder layer on top of a 500μm thick solid substrate. Physical properties of the NiTi alloy powder and substrate have been determined using techniques established in prior work [163], so the majority of the discussion will revolve around domain considerations such as geometry, meshing and boundary conditions.

The 5.0mm x 2.5mm x 0.5mm size of the representative domain in Figure 4.1 was used because it was the smallest possible domain that can contain the full simulation up to the point where a steady state is achieved. Steady state is defined as the point at which no appreciable difference can be found between the thermal profile of two successive laser hatches. Adequate steady-state

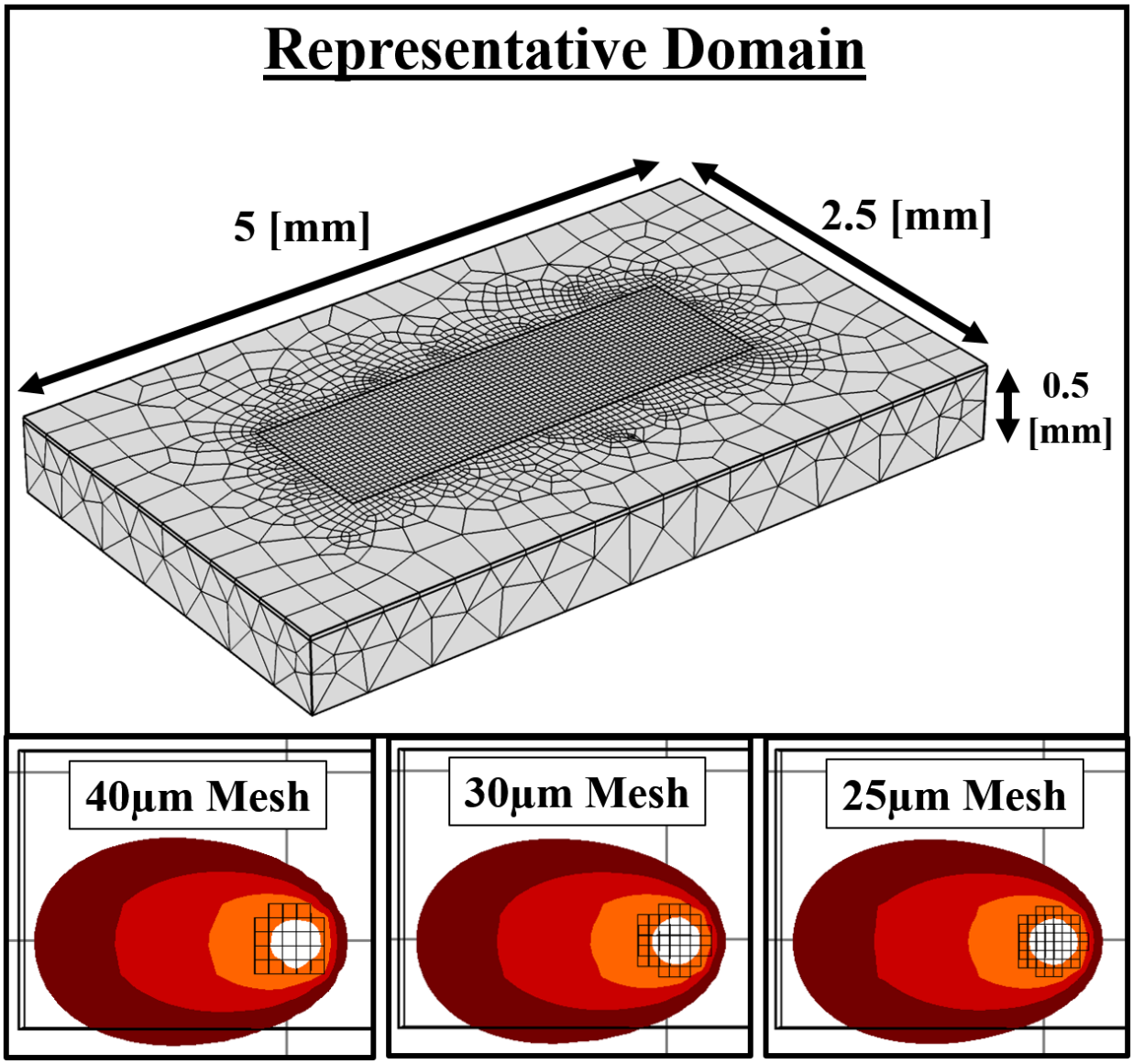

Figure 4.1: a) An example of the representative domains used in the finite element simulations for this research. A non-uniform mesh approach is used to balance domain size and simulation accuracy while minimizing the number of elements for the sake of computation time. b) Comparison of thermal contours for different mesh sizes in the fine mesh region. The 40μm mesh was used for the final results of this paper.

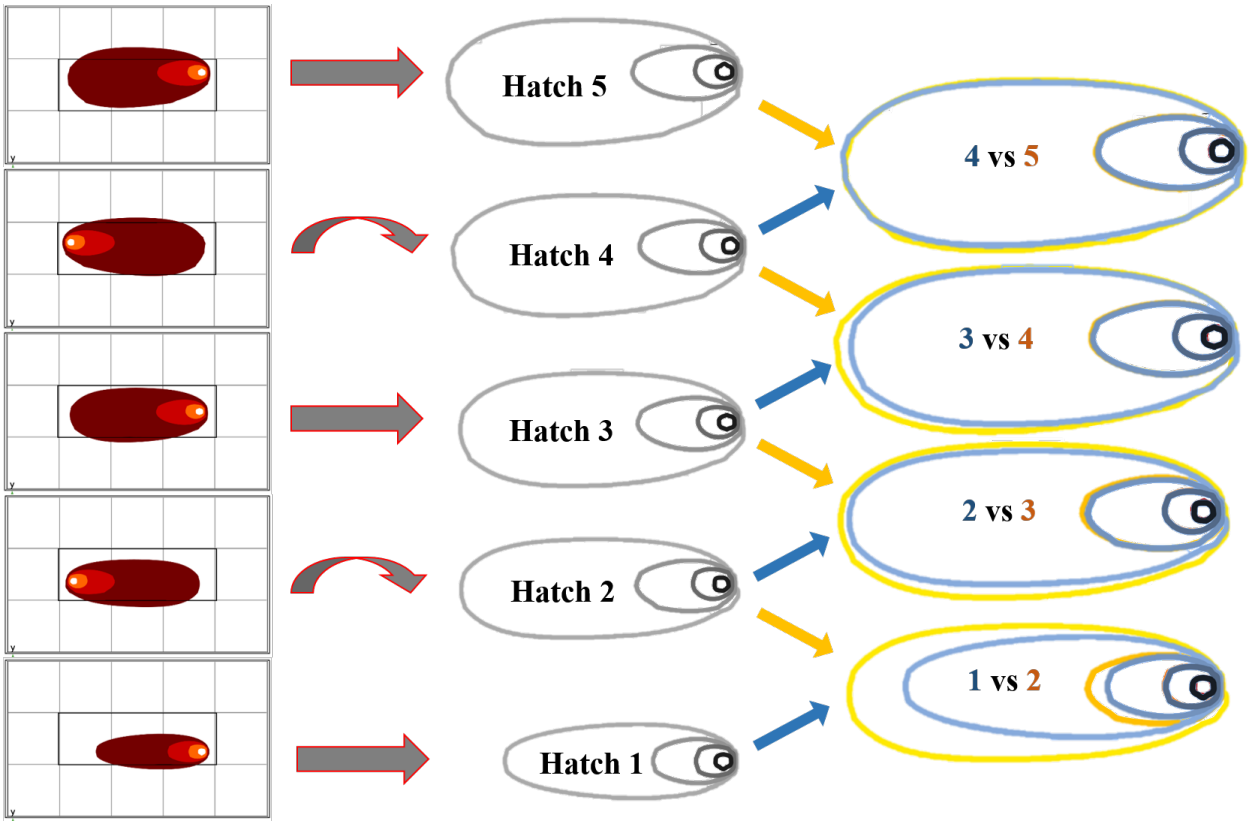

Figure 4.2: Steady state analysis of the first five laser hatches for a finite element simulation within the representative domain. Temperature contour plots of each hatch are overlaid to compare the difference in temperature profiles of each consecutive hatch. Every other laser hatch profile is mirrored to make temperature contours for alternating hatch directions comparable.

numbers of hatches were determined by comparing isotherms within the domain at the end of each simulated hatch. An example of this approach can be seen in Figure 4.2.

In addition to the steady state analysis, it is important to ensure that the boundary conditions and mesh size do not have significant effects on the simulation results. To this end, temperature profiles near the boundary were systematically checked throughout the simulation to ensure that temperature gradients smoothly approached room temperature. This smooth transition to room temperature indicates that the boundaries (held constant at 298 [K]) on the sides and bottom of the domain were sufficiently far such that they do not affect simulation results. The top boundary of the domain absorbs the moving Gaussian laser heat source throughout the simulation and releases energy following standard radiation and convection heat transfer laws. Inclusion of energy loss

through vaporization was also implemented, based on prior work with a similar model [163, 18]. Accounting for heat loss due to evaporation keeps the temperatures of the melt pool to physically realistic numbers without artificial heat sinks, a problem that is frequently reported in many previous FEM efforts in L-PBF AM.

The size of this representative domain relative to the sharpness of the thermal gradients seen in L-PBF AM necessitates the use of a non-uniform mesh similar to the one shown in Figure 4.1a. This particular approach was used to balance the need for a fine mesh to capture steep thermal gradients near the melt pool, and the need for a larger domain to capture longer thermal gradients. Comparisons of temperature profiles for different mesh sizes in the fine mesh region, Figure 4.1b, showed an optimal mesh size of 40μm. This size is small enough to capture the same thermal profile as the smaller meshes with significantly fewer degrees of freedom in the system, leading to a 30% decrease in computation time compared to the case with a fine mesh size of 25μm.

To this end, the representative domain has been fully defined and simulations within that domain have been performed. The resulting thermal history of these representative hatches in a single layer can now be extended via symmetry operations to construct the full domain.

4.2.2 Full Domain

For clarity, we emphasize that the symmetry operations detailed in this section are applied to the thermal history of the entire representative domain during the last hatch of the simulation. The thermal history of this last hatch represents the steady state thermal history that every subsequent hatch should produce. The steady state hatch selection is performed using the analysis shown in Figure 4.2 and detailed in section 4.2.1. There are two main symmetry operations that must be applied to the representative domain in order to construct the full domain. These operations are schematically depicted in Figure 4.3.

The first symmetry operation applied to the representative domain is a vertical glide plane perpendicular to the laser path, and passing through the centerline of the laser tracks, as shown in Figure 4.3a. The glide plane has a mirror operation at a spacing equal to the hatch distance used in the representative domain simulations. In this way, temperatures from the single steady

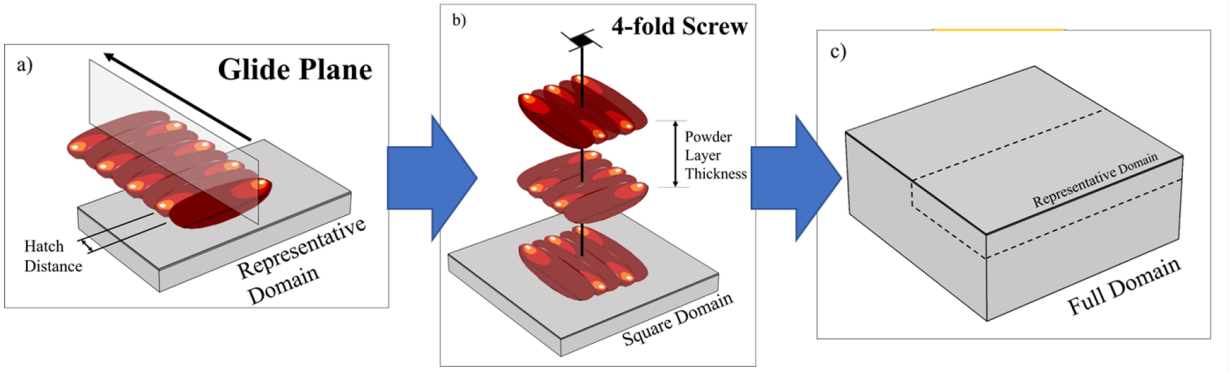

Figure 4.3: Schematic of the two symmetry operations used to construct the full domain based on the representative domain. The first symmetry operation is the vertically oriented glide-plane which passes through the centerline of the laser tracks. The second operation is a 4-fold screw axis in the z-direction which is centered in the middle of the xy-plane.

state hatch are translated one hatch further and mirrored to construct the next hatch in the opposite direction. The mirror and translation operations along the glide plane are halted once the domain projection in the XY-plane resembles a square. This extended domain from the first symmetry operation represents the full thermal processing of a single layer within a build. The next symmetry operation is then applied to this extended domain in order to construct the full thermal history of a multi-layer build.

The square shape of the extended domain in the XY-plane is necessitated by the next symmetry operation: a 4-fold screw rotation with 30μm spacing in the negative Z-direction centered in the XY-plane of the extended domain (Figure 4.3b). The 4-fold nature of the symmetry operation rotates the thermal history of each layer by 90 degrees in order to simulate the experimental scan strategy which rotates that hatch direction on every layer. The 30μm spacing along the Z-direction is dictated by the powder layer thickness. Figure 4.4 shows the un-rotated temperature profiles at certain depths of the extended square domain spaced at 30μm intervals.

The full thermal histories at each of these depths within the extended domain, shown in Figure 4.4 are the building blocks used to construct the multi-layered thermal histories of the full domain. The thermal history of each layer is rotated based on the 4-fold screw symmetry oper-

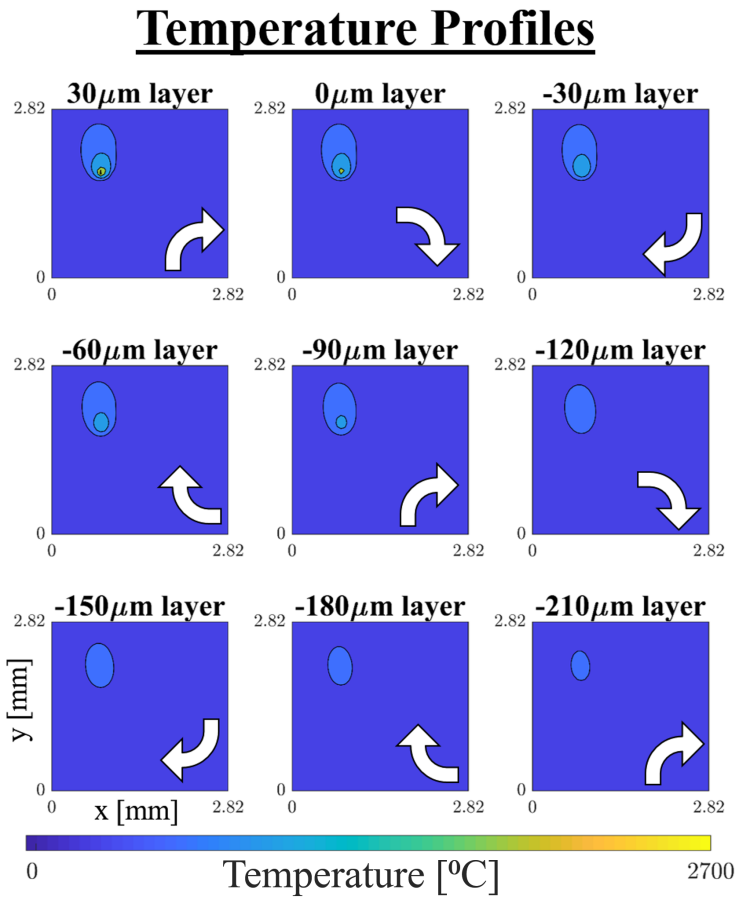

Figure 4.4: Temperature profiles taken at depths spaced 30μm apart. As part of the symmetry operations, every layer is rotated 90 degrees clockwise from the previous layer and these results are prepended the the thermal history of the layer below it. This process of rotation and prepending allows for the construction of multi-layer thermal histories in the full domain.

ation and prepended to the thermal history of the layer below it. After this symmetry operation is performed, each layer of the extended domain has the rotated thermal histories of every layer above it prepended to its own thermal history. For example, the 9th layer (at -210μm) will have the rotated thermal histories of the 8 layers above it added to the beginning of its own history. This is consistent with the fact that the 9th layer was the top layer of the build at one point but has since undergone 8 layers of processing.

With these two symmetry operation performed, we have constructed the complete multi-layer thermal history of the 2.83mm x 2.83mm x 1mm domain. The complicated thermal histories throughout this full domain can now be passed to the precipitation model used in this framework to predict phase fraction of Ni_4Ti_3 precipitates for any arbitrary hatch distance.

4.2.3 Precipitate Model

The precipitation model used in this study is implemented within the precipitation modeling software MatCalc. Microstructural evolution within this software is based on the Numerical Kampmann-Wagner (NKW) approach for precipitate modeling. In general, NKW modeling describes the evolution of precipitates within a material using a user defined thermal processing schedule as input to the model. The NKW technique models the evolution of precipitates within the system by subjecting each class of a discretized size distribution to mean-field equations (Equations 4.1-4.5) which govern nucleation, growth and coarsening. The rate of nucleation for new precipitates in a matrix material is modeled with classical nucleation theory using the transient nucleation equation:

$$J = NZ\beta^* e^{\frac{-G^*}{k_B T}} e^{\frac{-\tau}{t}} \tag{4.1}$$

The equation above includes traditional nucleation terms like critical nucleation energy (G^*) and the number of nucleation sites (N), as well as non-equilibrium modifications like the Zeldovich factor (Z) and (β^*) which account for random thermal fluctuations and atomic attachment rate respectively. Transience is dictated by the incubation time (τ) which can be calculated from Z

and β^*. After nucleation the Gibbs free energy of the system is calculated at each time step using Equation 4.2 which contains three major contributions from the matrix, particle, and interface.

$$G = \sum_{i=1}^{n} N_{0i}\mu_{0i} + \sum_{k=1}^{m} \frac{4\pi\rho_k^3}{3}\left(\lambda_k + \sum_{i=1}^{n} c_{ki}\mu_{ki}\right) + \sum_{k=1}^{m} 4\pi\rho_k^2\gamma_k \tag{4.2}$$

The first term describes chemical energy contributions from (n) elemental constituents in the matrix material. The second term accounts for chemical and volumetric-misfit contributions for each of the (m) precipitate size classes. The third term adds interfacial energy associated with those same (m) size classes. Dissipative factors are also considered with the inclusion of interface migration (Equation 4.3), precipitate diffusion (Equation 4.4), and matrix diffusion (Equation 4.5).

$$Q_1 = \sum_{k=1}^{m} \frac{4\pi\rho_k^2}{M_k^{IF}}\dot{\rho}_k^2 \tag{4.3}$$

$$Q_2 = \sum_{k=1}^{m}\sum_{i=1}^{n} \frac{4\pi RT\rho_k^5\dot{c}_{ki}^2}{45c_{ki}D_{ki}} \tag{4.4}$$

$$Q_3 = \sum_{k=1}^{m}\sum_{i=1}^{n} \frac{4\pi RT\rho_k^3(\dot{\rho}_k(c_{ki} - c_{0i}) + \frac{\rho_k\dot{c}_{ki}}{3})^2}{c_{0i}D_{0i}} \tag{4.5}$$

The number of precipitates in each size class is re-evaluated at each time step and the distribution is adjusted to reflect these changes. This cycle of mean-field equation evaluations and redistribution of precipitates continues until the end of the defined heat treatment. The evolution of this precipitate size distribution can be used to calculate single-valued metrics associated with the precipitates like phase-fraction and mean particle size over the entire course of the thermal treatment. Readers interested in further details of NKW modeling and its implementation within MatCalc are referred to a comprehensive description of the theory and methodology in [169].

Material properties and parameters used in the governing equations mentioned above were chosen for this particular $Ni_{50.9}Ti_{49.1}$ (at.%) shape memory alloy based on a Bayesian calibration procedure detailed in a previous paper [18]. The models predictions of matrix composition were used to calibrate against a number of heat treatments at various times and temperatures [164].

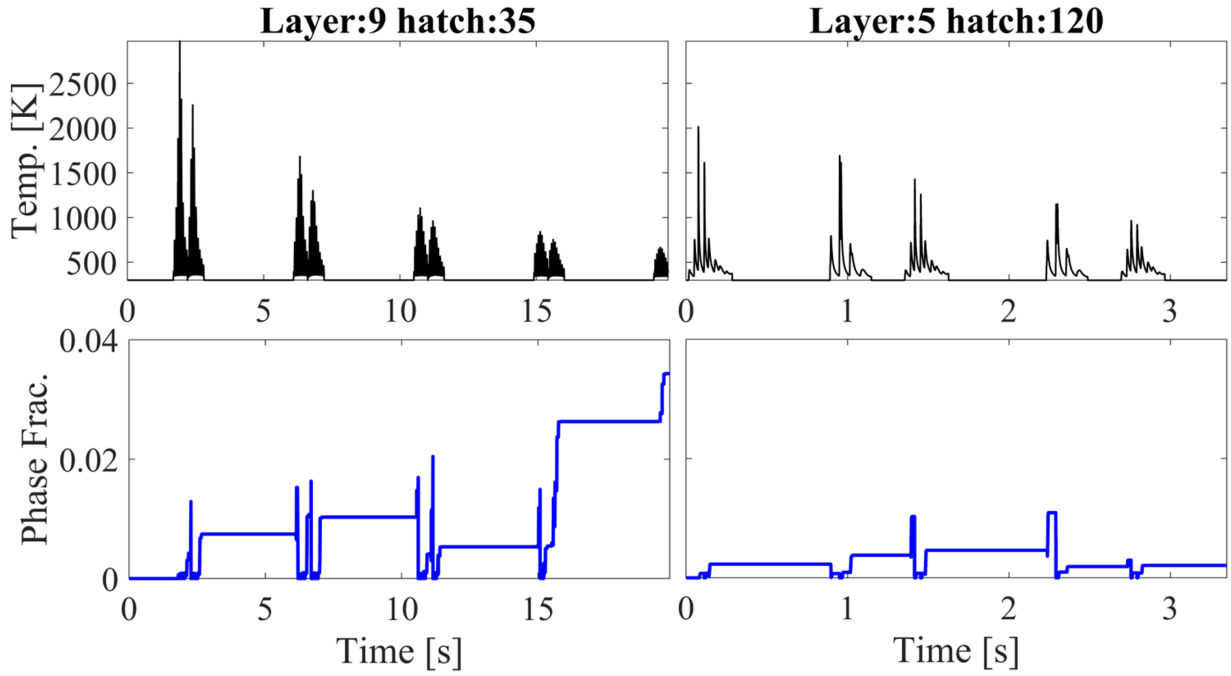

Figure 4.5: Comparison of phase fraction evolution over time for different points in two separate additive manufacturing processes. Each dip and plateau is due to the dissolution and subsequent growth of each layer. Lack of dissolution during the 8th layer of the 35 μm hatch case at 15 seconds corresponds to the dramatic increase in phase fraction shown in the left column of Figure 4.6.

Individual instances of this fully calibrated precipitation model can now be applied to unique thermal histories at discrete locations within the domain to determine the precipitate evolution at that point over the course of the entire thermal simulation. Results from these simulations at each node can be plotted and the resulting spatial variations can be analyzed to show trends in microstructural evolution throughout the domain. Examples of single-point predictions for two different processing strategies can be seen in Figure 4.5. The hatch distances and layers for both cases were chosen to showcase general differences in the thermal profiles associated with each hatch as well as the onset of lack of dissolution in the 8^{th} layer of the 35μm hatch case.

4.3 Results and Discussion

We now have a complete framework that can calculate the full multi-layer thermal histories coupled to a precipitation model that can predict phase fraction at discrete points throughout a

domain. This framework is used to calculate spatial distribution of precipitates for two processing strategies that vary only in hatch distance (120μm and 35μm).

The results of these calculations can be seen in Figure 4.6 where phase fraction distributions of Ni_4Ti_3 are shown for layers located between 150μm to 210μm beneath the surface of the build. Close proximity to the melt pool for layers shallower than 150μm leads to thermal histories that traverse the precipitation regime of 300-700 [°C] too fast to show significant precipitation. At layers deeper than 210μm, the material does not reach temperature values sufficient to significantly change the distribution of precipitates. This notion of significant precipitation occurring only at certain depths can be generalized to state that any point between 150μm and 210μm away of the melt pool at any given time is within a shell-like precipitation active region.

The thickness of the precipitation active shell described in the previous paragraph can be used to explain the differences in precipitate homogeneity between the 35μm and 120μm hatch cases shown in Figure 4.6. The 35μm case shows considerably more homogeneous spatial distribution of Ni_4Ti_3 precipitates than the 120μm case. Lack of homogeneity in the 120μm case is attributed to the fact that the hatch distance is much larger than the thickness of the precipitate active shell (60μm). A schematic of this concept is shown in Figure 4.7a.

Essentially, the laser hatches in the 120μm case are too far apart for their precipitation active shells to overlap, which results in certain regions of the domain spending more time in the precipitate active region than others. This leads to the peak-and-valley type distributions observed in the 120μm hatch case. However, in the 35μm case, the hatches are close enough to one another such that significant overlapping of the precipitation-active regions occurs, leading to a more homogeneous distribution of Ni_4Ti_3 precipitates.

The difference in spatial distributions of precipitates between these two cases can be used to explain the experimentally determined differences in the thermal and mechanical responses of the two processing conditions. In the experimental differential scanning calorimetry DSC results (see Figure 4.7b), we observe sharper peaks in the DSC curves of the 35μm hatch samples due to more homogeneous transformation behavior throughout the material [29]. Conversely, the increased

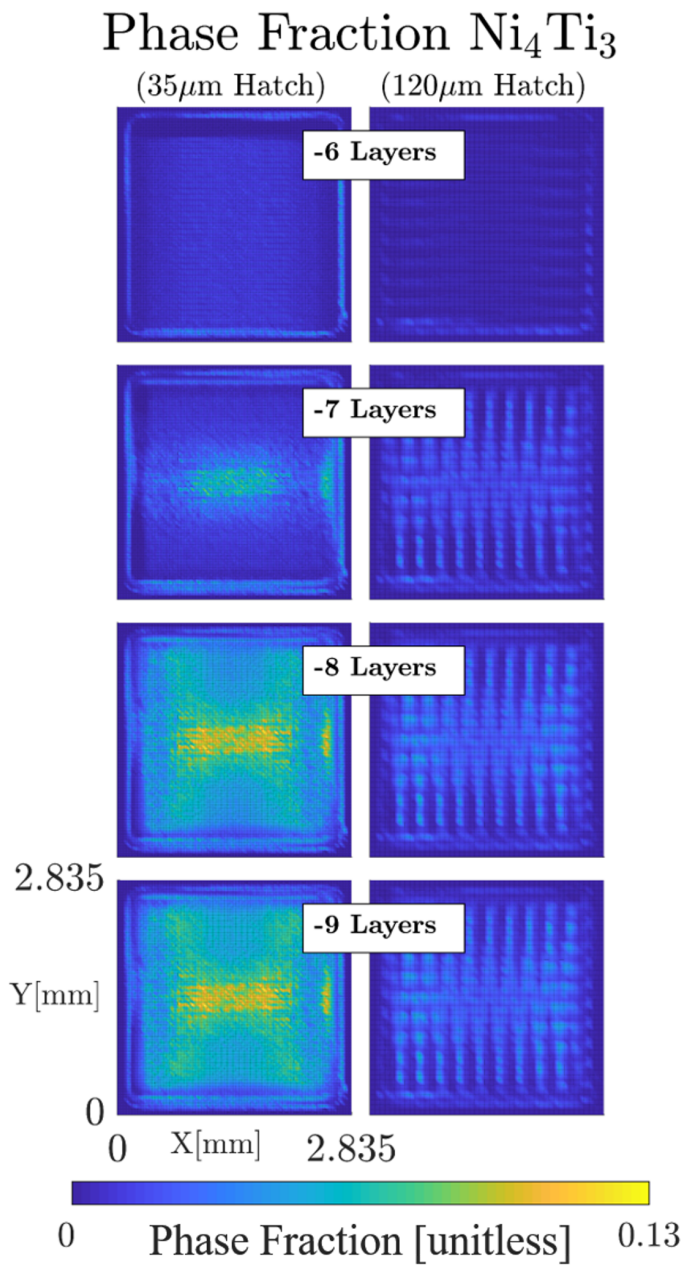

Figure 4.6: Comparing the effect of hatch distance on precipitate morphology through multiple layers. Differences in spatial homogeneity can be attributed to the lack of overlap in the precipitation active region of adjacent laser tracks in the 120μm case.

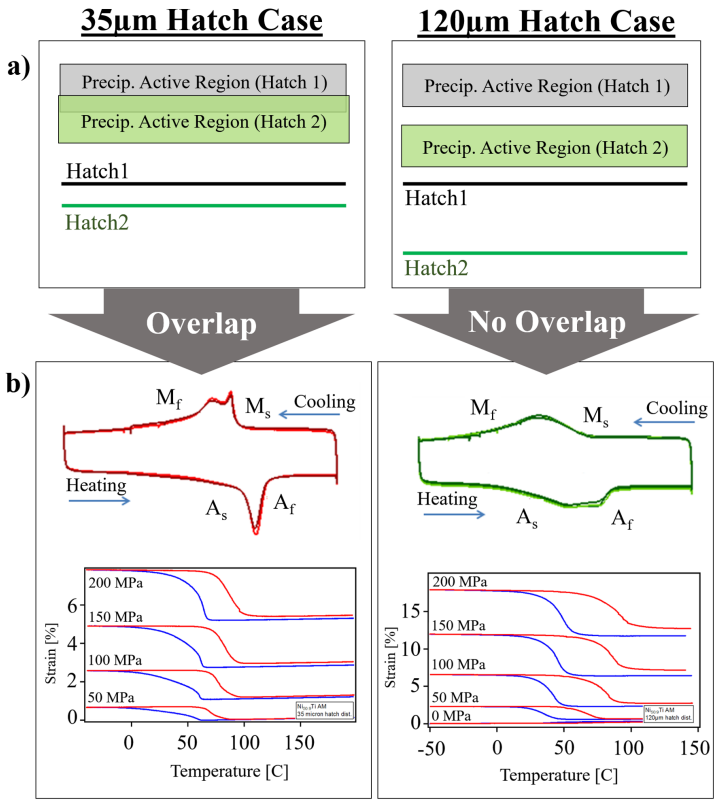

Figure 4.7: Explanation of experimentally observed differences [29, 162] in shape-memory transformation behavior for hatch distances of 35μm and 120μm. a) Distance between the laser hatch and precipitation active shell effects spatial homogeneity of precipitates. Certain regions of the domain will never encounter the precipitate active shell region if hatch distance is larger than the thickness of the shell. b) Process parameters that lead to overlap have sharper peaks and stiffer shape-memory responses due to the homogeneous spatial distribution of precipitates, as shown in Figure 4.6.

spatial variation in the 120μm hatch case leads to regions within the sample transforming at different temperatures, thereby broadening the range of temperatures over which the transformation occurs.

In addition to differences in transformation behaviors between the two cases, differences in mechanical response of the two samples shown in Figure 4.7b can be explained as well [162]. The larger phase fraction and increased homogeneity in the 35μm samples lead to increased energy dissipation during dislocation movement and propagation of the martensitic transformation front. These interactions between deformation mechanisms and precipitate structure lead to a stiffer material in the 35μm case indicated by smaller recoverable and irrecoverable strains. Spatial variation in the 120μm case, as well as a smaller volume fraction of precipitates overall, lead to less interaction between the precipitates and deformation mechanisms. The precipitate-poor regions in the 120μm case allow for larger regions of the build to accommodate deformation via detwinning, thereby increasing the recoverable and irrecoverable strain over that of the 35μm hatch case.

4.4 Conclusion

The overarching goal of this study was to investigate whether precipitation modeling can be used to explain experimentally observed effect of processing parameters on transformation properties in $Ni_{50.9}Ti_{49.1}$ (at.%) shape memory alloy parts fabricated using L-PBF AM. To accomplish this, thermal evolution simulations from an FEM of this domain were used as input to a precipitation model which predicts phase fraction of Ni_4Ti_3 throughout said domain. Relevant physical properties within both models have been calibrated in previous studies by the co-authors [18].

In order to capture the true precipitate distributions of an as-built part, the finite element model needed to predict the thermal evolution for multiple layers of processing with different hatch patterns for each layer. Steep thermal gradients within the domain necessitated a fine mesh and led to calculation times of 5 days for a single layer, meaning that full multi-layer calculations would take well over a month in the ideal case. To address this, symmetries of the laser processing pattern were used to reduce the multi-layer full domain to the smallest possible representative domain consisting of just a few hatches in a single layer. Symmetry operations were then applied to the

simulation results of this representative domain to construct the complete thermal history of the full multi-layer domain. Simulation time of this representative sub-domain was approximately 12 hours, i.e. over 60x faster than the fastest full multi-layer simulation.

The full thermal history of the domain was then passed to a precipitation model which calculated phase fractions throughout the build volume. Differences in the resulting spatial distributions of precipitate phase fractions for 35μm and 120μm hatch distance conditions were used to explain the differences in experimental DSC and stress-strain curves. More homogeneous precipitation and larger phase fraction of Ni_4Ti_3 in the 35μm case explain the narrower DSC peak and stiffer mechanical behavior as compared to the 120μm case. The broader DSC peaks in the 120μm case (Figure 4.7b) occur due to local variations in transformation temp, as indicated by the peak-and-valley pattern distribution of Ni_4Ti_3 seen in Figure 4.6.

Moving beyond the explanation of current experimental results, the increase in computational efficiency of the thermal model developed during the creation of this framework has enabled the exploration of the process design space. With simulations taking less than a day, it is now possible to establish a mapping from process parameters such as hatch distance, laser power, and powder layer thickness, to the spatial variation of precipitates. As an example, rapid iteration with multiple parallel instances of this framework can be used to determine possible adjustments to manufacturing processing parameters at different locations within a part in order to avoid the precipitation of undesirable phases at these locations. Different simulations may be necessary for each location due to variations in the length of each laser track. This ratio of laser track length to hatch distance may be an important parameter and is one of the topics currently being analyzed for a future investigation.

5. PREDICTIVE PRINTABILITY MAPS IN ADDITIVE MANUFACTURING OF METAL ALLOYS

5.1 Introduction

Despite known unique capabilities of metal-based Additive Manufacturing (AM) and the advances it has undergone over the past two decades, significant gaps are yet to be bridged in order to bring it to full maturity. A major roadblock is the high degree of variability in metal AM-fabricated parts, which poses serious challenges related to the qualification and certification (Q&C) of critical AM components [170]. Challenges to Q&C efforts are only compounded by the fact that metal AM has focused only on a handful of major alloy classes, with the bulk of the focus on titanium [171, 172, 173] (mostly Ti-6Al-4V), nickel [174, 175, 176] (IN625, IN718), stainless steels [177, 178] and other alloying systems that were not initially designed to be manufactured using AM technologies such as shape memory alloys [179, 162, 158, 29].

High variability in the quality and performance of metal AM parts can be attributed to the use of different processing schemes, energy source, raw materials, etc. Even when considering a single AM technology—such as laser powder bed fusion (L-PBF)—variability from the use of different machines, intrinsic variability in processing conditions, variance in local thermal histories, part geometry, and form of feedstock can have a significant impact [69, 180]. The early stages of research on metal AM focused on identifying machine-specific process conditions capable of yielding AM parts from conventional alloy feedstock with properties comparable to their as-cast or wrought counterparts [181, 182, 183, 184]. More recently, and motivated by the challenges associated with variability, the underlying paradigm for metal AM is shifting towards one that emphasizes control: it is no longer necessary to merely match the properties of conventional alloys, but rather to satisfy properties that enable Q&C of critical AM components for a specific application. As such, the processing routes (AM parameters, pre-or post-processing) selected must ensure that part performance is met on a *repeatable* basis.

In order to gain a better grasp of the ultimate causes for variability in AM, research efforts have been spent on developing strategies for improved process monitoring and control [185].*In-situ* monitoring approaches have already achieved a considerable degree of sophistication [186] and these approaches have moved beyond real-time measurement of melt pool dynamics [187] to monitoring the transfer of energy to the material [35]. *In-situ* monitoring has also begun to be used as a way to assess the quality of AM builds [188, 189]. Considerable challenges persist in this approach as some aspects of the thermal history associated with the solidification process (such as cooling rates, thermal gradients, etc.) are still exceedingly difficult to measure, although progress has been made in AM processes at moderate solidification rates [190].

A closed-loop control system capable of adjusting process conditions upon detection the onset of defect formation in real time remains highly challenging. However, some efforts have attempted to use lower resolution, lower temperature imaging techniques [161, 186, 185] as a strategy to monitor the AM process. These techniques are useful in controlling longer range physical phenomena like residual stress, but the time and length scales of the thermal gradients they capture are too slow and large to provide adequate data for controlling extremely fast phenomena like melt pool instabilities. In addition to visual imaging, acoustic signal analysis has shown some potential for detecting keyhole and crack formation [191, 186]. Further development of monitoring technologies will eventually lead to a better control of the AM process, particularly in light of the considerable sensitivity of most metal AM feedstock to variations in AM process conditions.

An admittedly less developed, but arguably more promising path forward from the materials perspective is to design alloys that are less sensitive to variations in AM processing conditions in the first place. Looking at the problem from this materials-centric viewpoint inevitably leads to the consideration of materials-inherent "printability" and the subsequent question of how to define such a metric.

In this paper, we propose a printability metric defined as the (hyper)volume in process parameter space for a laser powder bed fusion (L-PBF) metal AM process. Specifically we attempt to identify regions in the laser power vs scan speed space associated with builds that are free of major

defects, limiting our analysis to single tracks. We proceed to define this feasibility region in terms of the geometry of the melt pool in a way that is alloy agnostic by first carrying out predictions of melt pool dimensions using finite element methods within the COMSOL Multiphysics®heat transfer module. The thermal model includes phase-dependent thermo-physical properties which are used to approximate heat and mass transport phenomena such as melting, solidification, vaporization, and keyhole formation. By combining best estimates of thermo-physical properties with the high-fidelity thermal models we predict the *printability map* of two alloys: a Ni-5wt.%Nb (NiNb) alloy as a binary proxy for IN718 as well as a prototypical equiatomic CoCrFeMnNi high entroy alloy (HEA). The predicted printability maps are compared to an exhaustive exploration of the process space via experiments. The impact of using simplified thermal models as well as the effect of uncertainty in the thermo-physical properties are also examined.

5.2 On the Printability of Metal Alloys

The notion that different alloy chemistries are more/less suitable to processing via AM should not be surprising as historically this has been the case with other processing technologies/materials combinations. The influence of alloy composition on the quality of AM parts was illustrated early on by Childs *et al.* [192], who investigated the effect of process parameters on the build quality of stainless and tool steels printed with L-PBF techniques. Their results suggest that even small changes in the composition of the printed material can result in significant changes to the region in the process parameter space corresponding to successful prints. In agreement with this early work, Tomus *et al.* [193] recently investigated the suceptibility of Hastelloy alloys to hot-cracking and found that minor modifications to the C and Si content of the alloy reduced the tendency for hot-cracking. Harrison *et al.* [194] followed a different approach and modified a baseline Hastelloy formulation to increase solid solution strengthening and thus provide higher resistance to cracking. Martin *et al.* [14] successfully printed otherwise unprintable aluminum alloys by extrinsically doping the powder feedstock with tailored inoculants to control the solidification.

In a simplified manner, one could consider two different types of factors that control the degree to which a given alloy can be printed: *intrinsic* features of the alloy itself, such as solidification

range, presence of competing secondary solid phases, etc. can affect the microstructural morphology or texture of the printed material, while *extrinsic* factors such as process conditions affect the overall consistency of the fabricated part. AM research has primarily focused on finding useful combinations of these extrinsic factors such as laser power and speed [195], or linear energy density which is the ratio of these two parameters [179]. Both intrinsic/extrinsic factors are affected not only by the local processing conditions but by the alloy's thermodynamic and thermo-physical characteristics. Feasible regions in the alloy-process space can be identified in terms of their **printability**, which could be considered to be a global indicator for the resistance of an alloy-process combination to the formation of microscopic/macroscopic defects that compromise the integrity of the print. Questions remain as to how to properly quantify the printability of an alloy-process combination although there are some recent efforts in this direction.

Mukerjee *et al.* [196], for example, identified different dimensionless parameters that were used to estimate the susceptibility of an alloy-process combination to thermally-induced part distortion, composition heterogeneity due to differential evaporation, as well as incomplete inter-layer fusion and the resulting porosity due to incomplete penetration of the melt pool into the previous layers. These printability indicators were constructed from a combination of materials properties (such as melting, boiling points, thermal diffusivities, heat capacities, etc.), process conditions (such as linear energy density) as well as characteristics of the melt pool (width, depth, volume, area) and thus provide a way to evaluate the impact of process conditions on specific alloy formulations.

Using their printability criteria, Mukherjee *et al.* [196] investigated some of the most common metal alloys used in AM (IN718, SS316, Ti64) and found some correlation between their printability indicators and the presence of different kinds of issues such as thermal distortion, porosity or lack of composition control (due to differential evaporation) for three different processing conditions. This approach is useful for evaluating printability on a point-by-point basis, but it does not characterize the holistic printability of the alloy across all combinations of laser powers and scan speeds. As such it cannot take issues such as process variability into account. In a related (earlier)

work, Juechter *et al.* [197] investigated the processing space for Selective Electron Beam Melting (SEBM) with the goal of identifying combinations of scanning speed and linear energy density that resulted in minimal porosity and reduced composition changes due to differential evaporation. Through a combination of in-situ thermal monitoring and post-fabrication characterization, Scime and Beuth [189] have recently developed a method for mapping melt pool defects to laser powers and scan speeds, and related the incidence of such defects to major characteristics of the melt pool geometry.

The quality of the solidified structure during AM ultimately depends on the characteristics of the melt pool and it is thus reasonable to expect that criteria based on melt pool geometry can be used to establish thresholds for the onset of melt-pool related defects such as lack-of-fusion, balling, and keyhole formation [196, 198], which are some of the most dominant defect modes in L-PBF [199]. Lack-of-fusion occurs when the incident energy is insufficient to melt the substrate to a significant depth, which can result in large and/or very sharp voids within the as-built part. Balling is a periodic oscillation in the size and shape of a solidified track caused by capillary-driven instabilities of the melt pool and this oscillation leads to surface variations that can affect powder spreading during processing of the subsequent layer and that can lead to void formation. Keyholing is the formation of a depression in the surface of the melt pool due to recoil pressure from intense vaporization directly under the laser. The criteria for the onset of balling can be constructed from criteria used in welding and laser processing [200]. The lack-of-fusion threshold can be determined by comparing the melt pool depth and the powder layer thickness [196], while the onset of keyhole formation can be accounted for by considering the aspect ratio of the melt pool—further discussion of the criteria is described in 5.3.3.

Process parameter combinations that lie beyond established threshold values for the above criteria are eliminated from the feasible process space and the remaining region is regarded as the printable region or printability map. The size and shape of this remaining region/volume can be used as a *criteria for the design of an alloy suitable for AM*. In this context, a large predicted successful build region is an indication that some alloy of interest is insensitive to variations in

process parameters. This approach can potentially be quite significant as it implies the possibility of establishing a given alloy's printability map both before the onset of an experimental campaign and during each costly synthesis and characterization iteration.

Beyond size-based design metrics, selecting process conditions at points furthest from the boundaries of this printable area (i.e. robust design) provides maximum protection from inherent variability in machine processing conditions [201, 202, 203, 204]. Instead of eliminating or reducing variability, the design parameters of interest are guided to a region where the variability has less of an impact on the successful outcome of the build. Variability in machine parameters such as laser power and scan speed can be directly incorporated via constant-valued offsets to the boundaries based on the predicted or measured uncertainties. Incorporation of uncertainty in thermo-physical properties is accomplished through the use of surrogate model based uncertainty quantification [19, 180].

In this work, we explore the use of melt pool geometry-based criteria constructed by combining high-fidelity thermal models with best-estimates for the values of thermo-physical properties of two different alloy systems. A Ni-5wt.%Nb binary alloy is selected as it can be considered to be a proxy for IN718, particularly with regards to the segregation of Nb into interdendritic regions. Due to the small amounts of Nb it is to be expected that the thermo-physical properties of this alloy are relatively close to those of Ni and thus it is expected that the uncertainty in the values of these properties would be small. On the other hand, the CoCrFeMnNi high entropy alloy was chosen since it is very likely that HEAs, due to their phase stability characteristics—i.e. reduced competition of secondary solid phases upon solidification and significantly reduced diffusion kinetics—could become a very important feedstock for metal AM.

5.3 Methodology

The general workflow for predicting printability (Figure 5.1) starts with thermal model-based calculations of temperature profiles and subsequent melt pool dimensions for laser powers and speeds that span the process space. Gaussian Process response surfaces are then constructed for each of the three major melt pool dimensions and subsequently used to calculate ratios L/W,

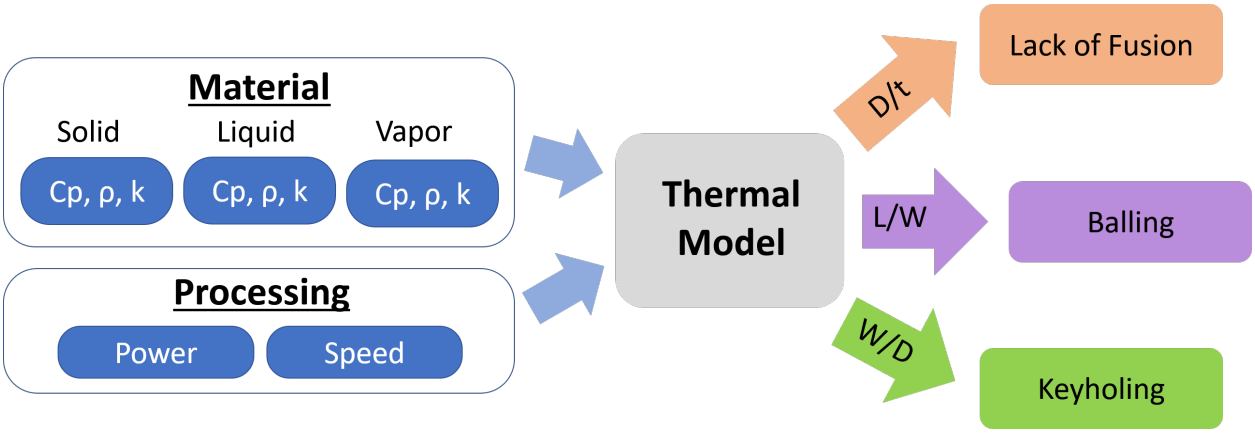

Figure 5.1: A general workflow for the printability framework described in this chapter. Processing parameters and phase-dependent material properties such as specific heat (C_p), density (ρ), and thermal conductivity (k) are provided to the thermal model. Melt pool dimensions calculated from the thermal model (L,W,D) and user prescribed powder layer thickness (t) are then used in the determination of defect formation using the ratios seen in the orange, purple, and green arrows. Any process parameters that do not belong to a defect are considered to be in a region of good quality.

W/D, D/t throughout the entire design space—L, W and D correspond to the length, width and depth of the melt pool while t corresponds to the powder bed layer thickness. Regions of process space with $D/t < 1.5$, $L/W > 2.3$ and $W/D > 1.5$ are labeled as regions susceptible to lack of fusion, balling, or keyhole formation, respectively. These threshold values are based on geometrical considerations and empirically determined values from literature [198, 205, 182]. Any area of the process space that is not labeled with a specific defect is considered to be a feasible combination of print parameters. Details of each step in this workflow are presented in subsequent sections.

5.3.1 Thermal Model

There is a plethora of approaches to modeling laser interactions with matter, from high-fidelity powder-scale methods [83, 82, 206] requiring thousands of simulation hours on a super-computing cluster to semi-analytical based models [80] that take minutes to run on a laptop. Finite element based methods are somewhere in between these two extremes with varying degrees of computational efficiency and fidelity based on the physical assumptions of the particular model. Selecting

which approach to use depends on the physical phenomena being studied, required accuracy, access to computational resources, and the desired frequency of feedback/iteration between computational and experimental methods.

The method for assessing printability presented in this study requires $O(10)$ simulations that are accurate throughout process space while maintaining relatively low computational cost such that the method could feasibly be introduced into an iterative optimization/design scheme. An Eagar-Tsai model [80] can rapidly conduct many simulations throughout the entire process space, but its many simplifications—including the neglect of phase transformation effects as well as the use of temperature-independent properties [80]—limit the predictive accuracy to narrow ranges of the process parameter space. A powder-scale model including fluid flow would be the most physically accurate, but the computational time per simulation renders the approach unable to sample the entire process space in a reasonable time. With this in mind, a conduction based finite-element thermal model was developed with the Comsol Multiphysics® heat transfer module.

The general form of the heat transfer equation below describes the transient evolution of temperature (T) within a material domain as it is subject to some thermal load(s) (Q).

$$\rho C_p \frac{\partial T}{\partial t} + \nabla(-k\nabla T) = Q \tag{5.1}$$

The rate of temperature evolution within the domain is governed by the thermo-physical properties of the material, namely density (ρ), specific heat (C_p), and conductivity (k). In this model, we modify and expand the model to account for additional physical phenomena such as energy contributions from phase transformations and temperature/phase-dependent thermo-physical properties. A coordinate transformation is also applied to the transient term:

$$\frac{\partial T}{\partial t} = \frac{\partial T}{\partial x}\frac{\partial x}{\partial t} + \frac{\partial T}{\partial y}\frac{\partial y}{\partial t} + \frac{\partial T}{\partial z}\frac{\partial z}{\partial t} = \nabla T \vec{v} \tag{5.2}$$

This transformation shifts the reference frame from a Lagrangian reference frame fixed on the material substrate to an Eulerian reference frame fixed to the laser heat source moving at a

constant scan speed $\vec{v}$. The elimination of the transient term in the heat transfer equation comes at the expense of introducing nonlinearity in the form of an advective term:

$$\rho C_p \nabla T \vec{v} + \nabla(-k\nabla T) = Q \tag{5.3}$$

Equation 5.3 represents the steady-state form of the equation which can be solved an order of magnitude faster, even with a very fine 2 μm mesh in and around the melt pool. This fine mesh significantly reduces mesh size effects and convergence issues associated with the nonlinear nature of the problem. A schematic of the Finite Element domain and a representative melt pool can be seen in Figure 5.2. Boundary effect testing showed that a domain size of 6mm x 1.5mm x 1.5mm was sufficient for all laser power and scan speed combinations.

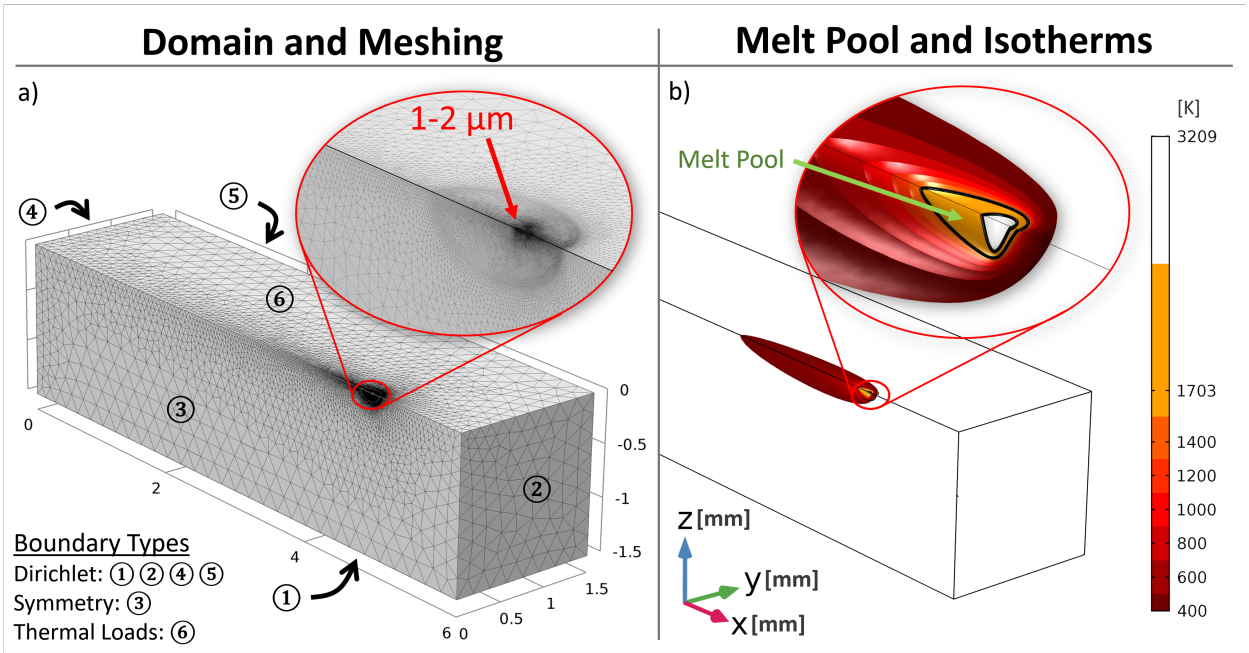

Figure 5.2: Schematic showing the Finite Element model's a) domain size, meshing technique, boundary conditions and b) isotherms from a representative melt pool simulation with the laser traveling in the positive x-direction.

Boundary conditions for this model consist of mirror plane symmetry on boundary 3 and Dirichlet conditions on boundaries 1, 2, 4, and 5 with a fixed temperature of $T_0 = 298K$. The surface (boundary 6) contains all of the heat transfer phenomena that contribute to the source term (Q) in Equation 5.3.

$$Q = q_{rad} + q_{conv} + q_{vap} + q_{beam} \tag{5.4}$$

$$q_{rad} = \varepsilon\sigma_B(T_{amb}^4 - T^4) \tag{5.5}$$

$$q_{conv} = h(T_{amb} - T) \tag{5.6}$$

$$q_{vap} = L_v \sum_{i=1}^{n} X_i 44.331 p_i(T)\sqrt{\frac{MW_i}{T}} \tag{5.7}$$

$$q_{beam} = a(T)P\Big[\frac{1}{2\pi\sigma^2}exp\Big(-\frac{(r-r_0)^2}{2\sigma^2}\Big)\Big] \tag{5.8}$$

Equations 5.5-5.8 describe surface radiation, natural surface convection, vaporization, and deposited beam power, respectively. The radiation and convection terms are of the form typically implemented in finite element modeling of L-PBF. The evaporative energy loss q_{vap} and beam deposition q_{beam} include modifications that account for mass transport and energy transport within the vapor phase, respectively. Equation 5.7 is a Bolten-Block/Eagar model [207] that has been slightly modified to include temperature dependent partial pressure relationships calculated using equations described in [208]. Equation 5.8 includes a phase-dependent absorptivity term that allows for the incorporation of keyhole formation without the need to consider more computationally expensive fluid dynamics. Details of the parameters contained within these equations are included in the next section.

5.3.2 Model Parameters

The parameters in Equations 5.3-5.8 can be generally categorized into temperature/phase-dependent and non-temperature/phase-dependent properties. Physical parameters considered to be constant within each simulation are: Stefan-Boltzmann constant (σ_B), ambient temperature

($T_{amb} = 298K$), molecular weights of each element (MW_i), and emissivity ($\varepsilon = 0.7$). We note that the value for emissivity is based on an average of many alloys and is not a parameter of interest since the radiative contribution to the energy balance at the surface is orders of magnitude smaller than that of vaporization. Laser process parameters such as laser power (P), scan speed ($\vec{v}$), standard deviation (σ), and centerpoint (r_0) are also considered to be constant during each simulation. σ is calculated as 1/4 of the beam diameter as is common throughout the literature. The set of temperature-dependent properties consists of: density (ρ), specific heat (C_p), thermal conductivity (k), absorptivity (a) and partial pressure of each element (p_i). Phase-dependent values for all of these properties can be found in Table 5.1. The natural convection coefficient (h) in Equation 5.6 is calculated within Comsol based on domain geometry and orientation.

5.3.2.1 Phase Transitions

Smooth transitions between the phase-dependent thermo-physical property values (ρ, C_p, k, α) in Table 5.1 are realized by averaging the properties of each phase based on their respective fractions during the transformation. Latent heats of fusion and vaporization (L_m and L_v, respectively) are included in the model through addition of an equivalent heat capacity during their respective transformations. Details of this effective property approach were explained in a previous publication [163].

5.3.2.2 Property Calculations

Due to a lack of experimental thermo-physical property data, values for the Ni-5wt.%Nb alloy in Table 5.1 were calculated using a weighted average of Ni and Nb elemental properties found in [209]. A weighted average is sufficiently accurate in this case due to the dilute nature of this single-phase solid-solution alloy. The values of the thermo-physical properties of the HEA are taken directly from the literature sources cited in Table 5.1. For both alloys, vapor phase conductivity and absorptivity values are selected to approximate the transmission and subsequent reflection of the laser within the vapor void present during keyhole-mode melt pools.

5.3.2.3 Variable Absorptivity

Absorptivity values for all phases are chosen based on a recent study from Lawrence Livermore National Lab that shows experimental evidence for low effective absorptivity of the solid/liquid phases and high effective absorptivity upon vaporization and keyhole formation [35]. Conductivity of the vapor phase in the vertical z-direction was increased by an order of magnitude to approximate the transmission of electromagnetic laser energy *through* the vapor phase. The combined increases in absorptivity and conductivity lead to a more realistic representation of laser-matter interaction at the point of incidence over a wide range of laser powers and scan speeds. Laser penetration of the vapor phase allows the system to transition seamlessly between surface and volumetric heating conditions without any changes to the laser source term which eliminates the need to select between the two approaches *a priori*. Low energy densities do not form a significant amount of vapor, so the laser does not penetrate the substrate and the simulation converges to a conduction-mode melt pool. Conversely, process parameters with high energy density lead to simulations with a stable region of vapor and the laser energy is transferred deeper into the substrate via the enhanced vapor conductivity.

This vapor/keyhole based laser absorption model is in direct contrast with current absorption methods common in AM literature that focus primarily on powder layer effects. Volumetric heat sources are typically used to represent the penetration and absorption of laser energy within the thin layer of powder above the substrate. While this laser-powder interaction is valid prior to melt pool formation, it fails to represent the primary incidence of the laser upon molten metal once the melt pool has formed during normal operations [35, 212]. As such, the powder layer and the effective material properties associated with it are not directly modeled.

5.3.3 Printability Predictions

Results of the fully developed thermal model must be extended, analyzed and post-processed in order to predict various defect prone regions of the process parameter space. Any portion of the

Table 5.1: Phase-dependent thermo-physical properties used in the thermal modeling of the Ni-5wt.%Nb and the CoCrFeMnNi HEA studied in this work. For the Ni-5wt.%Nb alloy, property values for each phase are calculated using a weighted average of the pure elemental properties of each constituent. HEA properties directly taken from literature as cited.

Phase (*i*)	**Solid (*S*)**		**Liquid (*L*)**		**Vapor (*V*)**	
	NiNb	**HEA**	**NiNb**	**HEA**	**NiNb**	**HEA**
ρ_i [kg/m^3]	8900 [M]	7700 [210]	8450 [209]	7400 [209]	$\rho(T)$ [207]	$\rho(T)$ [207]
C_p^i [J/kgK]	550 [209]	600 [209]	650 [209]	650 [211]	$C_p(T)$ [211]	$C_p(T)$ [211]
α_i [unitless]	0.3 [35]	0.3 [35]	0.3 [35]	0.3 [35]	0.6 [35]	0.6 [35]
k_i [W/mK]	85 [209]	20 [209]	120 [209]	40 [209]	5 [211]	5 [211]
k_{iz} [W/mK]					1000 [A]	1000 [A]

Transf. (*t*)	**Solid $\leftrightarrow$ Liquid (*m*)**		**Liquid $\leftrightarrow$ Vapor (*v*)**	
	NiNb	**HEA**	**NiNb**	**HEA**
T_t [K]	1703 [M]	1644 [210]	3209 [211]	3086 [210]
ΔT_t [K]	50 [209]	100 [209]	200 [A]	500 [A]
L_t [kJ/kg]	290 [211]	232 [211]	7100 [211]	4961 [210]

[M] value taken from powder supplier Material Safety Datasheet
[A] Artificially enhanced as described in Section 5.3.2.2

process space that is not part of a defect prone region is defined as printable. This section describes the steps necessary to predict those regions and the uncertainty bounds on their boundaries.

5.3.3.1 Response Surface Modeling

The Matlab®based OODace Toolbox [213] was used to calibrate three Gaussian Process (GP) models to melt pool length, width, and depth predictions from a grid of 30 thermal model simulations that spanned the full ranges of laser power and speed available on a 3D Systems®ProX DMP 200 L-PBF system. The resulting GP response surfaces can be used as computationally inexpensive surrogates [19] for calculating critical ratios (L/W, W/D, D/t) of melt pool dimensions and powder layer thickness. Since GP predictions are inexpensive, these calculations can be performed on a much finer grid of laser powers and scan speeds which results in more refined definitions of the boundaries between each print region in the process space.

5.3.3.2 *Printability Criteria*

Regions of the process space are defined through comparisons of critical ratio response surface values to the threshold criteria ($L/W < 2.3$, $W/D < 1.5$, $D/t > 1.5$), which are derived from empirical observations, physical principles, and pure geometrical considerations. The threshold value $L/W < 2.3$ is related to melt pool "balling" or "humping"; a phenomenon that is widely considered to be the result of Plateau-Rayleigh instabilities in the molten metal [205, 182]. Although there is no agreed upon value for the L/W ratio threshold in the literature, values typically range between $2 < L/W < \pi$ [182, 205]. The criteria associated with keyholing can be derived from the assumption of a semi-circular melt pool in the vertical cross section perpendicular to the direction of laser motion. A keyhole criteria of $W/D > 2$ would be a reasonable approximation for a half-circle melt pool in conduction mode laser processing with isotropic material parameters and heat flow. In practice, the presence of other heat transfer modes such as radiation, convection, and vaporization dissipate heat at the surface which results in a decrease in depth of conduction mode cross sections. As such, a keyhole threshold of $W/D > 1.5$ is a better predictor. In comparison, the lack of fusion criteria ($D/t > 1.5$) is quite simple. If the depth of the melt pool D does not exceed the prescribed powder layer thickness t, the melt pool will not fully fuse to the substrate.

These criteria are meant to be approximate guidelines for the comparison of alloy printability and optimization of their compositions/processing. As such, the threshold values are subject to change according the the risk tolerance of the alloy-process designer. In addition to changing the threshold values, some assessment of potential risks can be incorporated through the propagation of uncertainty in the parameters of the thermal model.

5.3.3.3 *Uncertainty Propagation*

The effect of material property uncertainty on the location of successful print region boundaries is calculated via surrogate model based uncertainty propagation [19]. A Gaussian Process based surrogate model is calibrated to the melt pool dimension results from a set of 300 Latin-Hypercube samples over the 6 critical material parameters (K_S, K_L, K_V, $K_V z$, $\alpha_{s/l}$, α_V). Con-

ductivities and absorptivities were chosen as the parameters of interest due to their significant influence on the results and the relatively high degree of uncertainty in their values. Of the three primary thermo-physical properties (C_p,ρ,k), conductivity values are much more difficult to measure/calculate [214], especially in the liquid and vapor phases due to the high temperatures and the confounding effects of natural convection during the measurement process [215]. Additionally, the liquid conductivity is often artificially elevated in AM thermal modeling to approximate the effect of convection.

Once the surrogate model has been calibrated to the thermal model, all material parameters are fixed except one, which is subjected to 10,000 Monte Carlo samples. 95% confidence intervals of the resultant distributions for melt pool length, width and depth are then used to find confidence intervals for the print-region boundaries.

5.3.4 Experimental

The materials used to manufacture L-PBF specimens were gas atomized equiatomic CoCrFeMnNi powder and Ni-5wt.%Nb powder provided by Nanoval GmbH & Co. KG. Single tracks were printed using a 3D Systems ProX DMP 200 Laser Type (fiber laser with a Gausian profile, λ = 1070 nm, and beam size = 100 μm). CoCrFeMnNi single tracks were printed on an arc melted CoCrFeMnNi base plate. The tracks were 15 mm in length with 1.5 mm spacing between each track. The Ni-5wt.%Nb alloy was subject to two separate experiments with the only difference being the substrate material. The first experiment (Exp1 in Figures 5.3 and 5.6), consisted of printing the Ni-5wt.%Nb alloy on a pure nickel substrate, whereas the second experiment (Exp2 in Figures 5.3 and 5.6) was printed on a base plate formed from Ni-5wt.%Nb. In Exp2, the base plate was homogenized (1100 ^{o}C for 1 hour, then air cooled). These tracks were 10 mm in length with 1 mm spacing between tracks.

Cross sections of the single tracks were wire cut using wire electrical discharge machining (EDM). The specimens were polished down to 0.25 μm, then vibratory polished in colloidal silica. A mixture of 10 ml H2O, 1 ml HNO3, 5 ml HCl, and 1 g FeCl3 was used to etch HEA single tracks for metallographic investigation. Kalling's Solution No. 2 (5 g CuCl2, 100 mL HCl, and 100 mL

ethanol) was used to etch the Ni-5wt.%Nb single tracks. Optical Microscopy was carried out using a Keyence VH-X digital microscope equiped with a VH-Z100 wide range zoom lense. Width and depth measurements were conducted using the VH-X microscope software. Three cross sections were cut and measured from each track. The displayed width and depth values are averaged from these three measurements.

5.4 Results and Discussion

In additive manufacturing, as with other manufacturing techniques, it is of utmost importance to develop an understanding of the feasible conditions for processing the material. This section presents and discusses printability predictions from the above methodology for Ni-5wt.%Nb and CoCrFeMnNi HEA, and compares the resultant maps against systematic experimental investigation of the process parameter space for those alloys carried out as part of this work. It is important to emphasize that **the experimental investigation of the process parameter space was not used in any way to fit the material properties or model parameters used in the computational methodology or the subsequent construction of the predicted printability maps**.

Maps labeled *Finite Element* in the figures presented below are constructed through the application of the printability criteria to melt pool dimension predictions from the Finite Element model developed herein. The same criteria were applied to Eagar-Tsai melt pool dimension predictions for comparison. Cross sectional images of representative melt pool morphologies from each process parameter region, identified by the criteria above, are also shown in these figures beside each set of maps. The observed morphologies of every experimental track are indicated by markers of different color and shape.

After a comparison of the predictions and experiments for each alloy, boundary uncertainty plots, determined according to the methodology discussed in 5.3.3.3, for key parameters of the Finite Element model are analyzed. Comparisons of the boundary widths in each plot indicate the relative importance of each thermo-physical parameter and identify potential sources of improvement in the Finite Element model and its assumptions.

5.4.1 Printability Maps for Ni-5wt.%Nb alloy

Figure 5.3 shows the predicted printability map for the Ni-5wt.%Nb alloy in comparison with experiments. The top printability map was determined using FE-based predictions of the geometric characteristics of the melt pool under different processing conditions. Different regions are labeled after the dominant type of defect (or their absence) to be expected based on the criteria described above. At low powers and (generally) at high velocities it is evident that the dominant defect is lack-of-fusion (light brown/orange). At relatively low scan speeds and high power the predicted dominant defect is keyholing (green). On the other hand, in the high scan speed-high power region of the process space the dominant defect is balling (magenta) due to capillary-based instabilities of the melt pool. The so-called printable region (blue) in power-scan speed space thus results from the subtraction of these three defect-prone regions from the power-scan speed space.

As is evident from the figure, there is overall an acceptable level of agreement between the predicted and the actual measured printability maps for the Ni-5wt.%Nb alloy investigated in this work, with the majority of the experimental points falling within the correct predicted region. However, there are a few exceptions near the keyhole and balling boundaries. There is a clear delineation between the experimentally observed keyhole and good quality melt pool results, but the slope of the predicted border is too horizontal. Two experimentally observed balling conditions are also mis-classified as printable by the Finite Element model. These misclassifications near the keyhole and balling borders are likely due to the lack of free-surface fluid-flow modeling which can more accurately predict laser penetration, viscosity, and surface tension effects that are important during keyholing and balling phenomena.

Beyond comparisons between models and overall experimental results for the Ni-5wt.%Nb printability map, we note that there are also minor disagreements between the two sets of experimental observations near the keyhole and balling boundaries in the Ni-5wt.%Nb map. The most obvious discrepancy is an observation of a good single track in the *Exp1* dataset (hollow markers, Figure 5.3) at a higher laser power and similar scan speed (P=200 W, v=1275 mm/s) than two single tracks with balling morphologies (P=178 W , v=1154 mm/s and P=178 W, v=1515 mm/s)

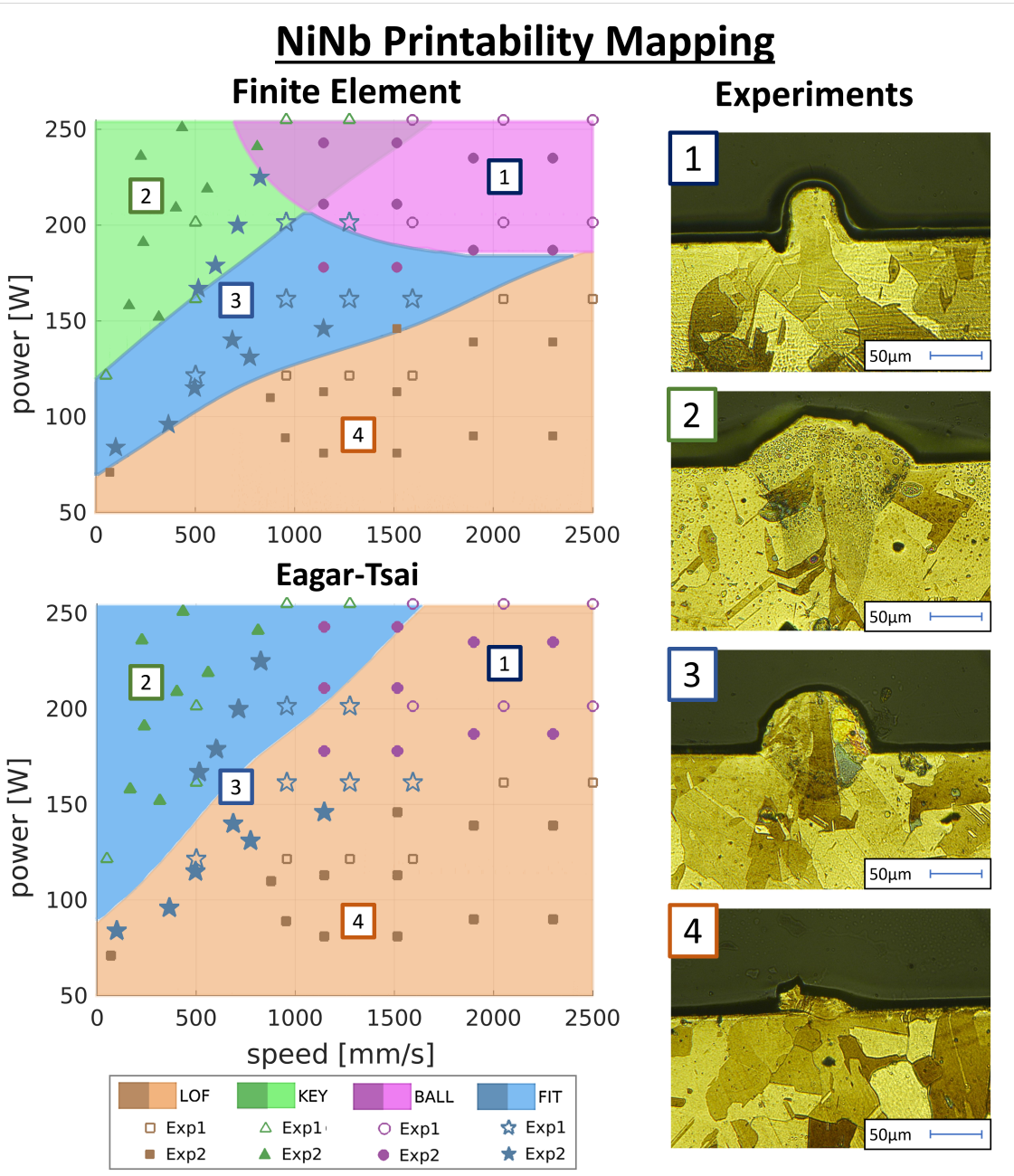

Figure 5.3: Printability maps that predict melt pool morphology regions for a Ni-5wt.%Nb alloy. Predicted regions are as follows: good quality (blue,G), keyholing (green,KEY), balling (purple,BALL), and Lack of Fusion(orange,LOF). Experimentally observed morphologies throughout the process parameters space are indicated by markers of different shapes following the same color scheme as the predicted regions. Hollow and filled markers indicate if the data is from Exp1 or Exp2, respectively. Four representative melt pool cross sections from each region can be seen on the right. Eagar-Tsai predictions are essentially uninformative in this case due to constant material properties and the neglect of phase transformation effects.

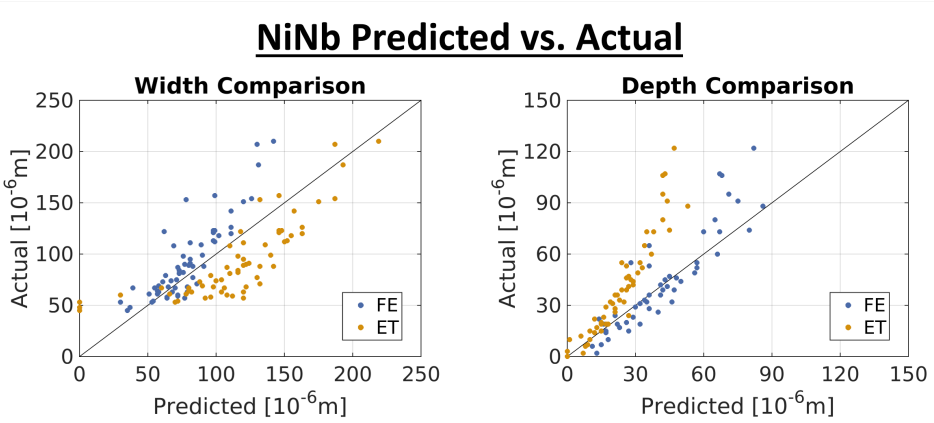

Figure 5.4: Diagnostic plots showing the predictive accuracy of the Finite Element and Eagar-Tsai models for both melt pool width and depth for the Ni-5wt.%Nb alloy. The Finite Element model has much better agreement with the depth as would be expected with the improved laser source term. The Eagar-Tsai model over-predicts width and under-predicts depth.

in the *Exp2* dataset (solid markers, Figure 5.3). This shift in the onset of balling to lower laser powers and scan speeds in *Exp2* can be attributed to the slight differences in the experimental conditions due to the differences in powder handling and substrate material. *Exp1* single tracks were deposited on a pure Ni substrate whereas *Exp2* tracks were deposited on a Ni-5wt.%Nb substrate.

In contrast to the Finite Element thermal model, the Eagar-Tsai model possesses almost no predictive capability with these printability criteria. It drastically overestimates the size of the lack-of-fusion region and fails to identify the keyhole and balling regions entirely. The uninformative nature of this Eagar-Tsai-based printability map is due to two key simplifying assumptions with the model itself: i) constant thermo-physical properties and ii)surface-only energy deposition for all processing conditions. These assumptions render the model unable to capture phase change phenomena and the transition to laser penetration during keyholing, respetively. The result is an inability to predict the drastic changes in melt pool aspect ratios that are so critical to melt pool stability and the printability criteria used herein. This also makes it difficult to calibrate the Eagar-Tsai model to both depth and width over the entire parameter space; an issue which can be seen in the predicted-actual plots in Figure 5.4.

Further examination of the performance of the Eagar-Tsai (ET) and Finite Element thermal models relative to experiments can be observed in Figure 5.4, which shows that the ET model over-predicts the melt pool width and under-predicts the melt pool depth for this set of material parameters. Since the model assumes constant thermo-physical properties (ρ,C_p,k), changes to any one of them will uniformly affect the melt pool dimensions and calibrating for the width will ultimately shift the depth predictions further astray. Changing multiple thermo-physical properties at once offers more flexibility, but the effect is still limited. In contrast, the Finite Element model has phase-dependent thermo-physical properties and includes additional heat transfer considerations like the transition from surface to volumetric heating, described in the methodology section. This allows for more accurate predictions over a wider range of the process parameter space and results in better width predictions and very good agreement with depth measurements, also seen in Figure 5.4.

While the results presented so far suggest a very good agreement between the predicted printability regions and the independent experimentally determined melt pool geometry maps, further verification of the proposed framework can be provided by comparing these results with those of Scime and Beuth [189]. The motivation for Scime and Beuth was to develop a framework for the identification of melt pool signatures indicative of flaw formation in L-PBF processed Inconel 718. They used in-situ thermal monitoring combined with post-fabrication characterization to establish relationships (via machine learning) between process conditions and melt pool characteristics. Remarkably, they settled **on exactly the same characteristics** (balling, lack-of-fusion, keyhole formation) as the ones used in the present work—and arrived at independently—to construct the predicted printability maps. By comparing Figures 5.3 and 5.5, it is seen that the agreement between the predicted Ni-5wt.%Nb printability map and the printability map determined by Scime and Beuth [189] is extremely good, showing the same topology and even presenting a reasonable quantitative agreement with regards to the actual position of the feasible, keyholing, lack-of-fusion and balling regions. This agreement with experimental results from a different research group and L-PBF system (EOS M290) highlights the generalizability of the computational methodology

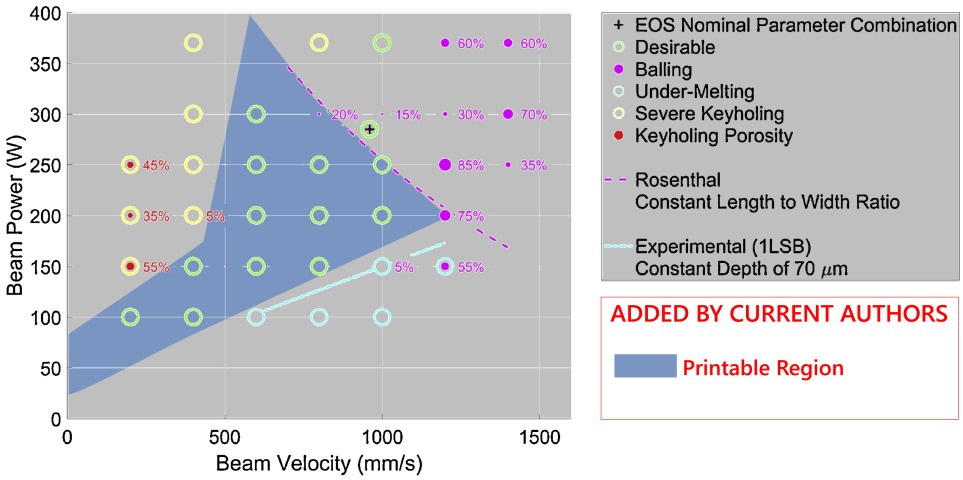

Figure 5.5: Experimentally determined melt pool morphology map for an Inconel718 alloy [1]. The reader is encouraged to read the original work for in-depth explanations of the notation in this figure. Similar to the current study, various markers indicate experimentally observed melt pool morphologies as desireable, keyholing, undermelting (i.e. lack-of-fusion), and balling. The topology of the different melt pool morphology regions in the map agree with the predicted printability regions for Ni-5wt.%Nb in the current work shown in Figure 5.3. Printabilty predictions are assumed system-agnostic since these observations are from an EOS M290 printer.

herein. Ideally, an experimental methodology like the one described in [189] could be combined with the computational methods of this framework to create a single synergistic workflow for iterative optimization of printability. Experimental process characterization for an existing alloy would inform this computational framework which would then be used to search for promising alloy modifications to test in the next iteration of the design process.

5.4.1.1 Boundary Uncertainties for Ni-5wt.%Nb Map

The additional physics included in the Finite Element model comes at the price of increased number of parameters. In order to establish which of these parameters have the most effect on the predicted printability maps, we propagate uncertainty from key thermo-physical properties to the print region boundaries of the printability map itself, shown as the shaded regions surrounding each boundary in Figure 5.6.

[1]Reprinted from Additive Manufacturing, Vol 25, L. Scime and J. Beuth, "Using machine learning to identify in-situ melt pool signatures indicative of flaw formation in a laser powder bed fusion additive manufacturing process", Pages 151-165, Copyright 2019 with permission from Elsevier.

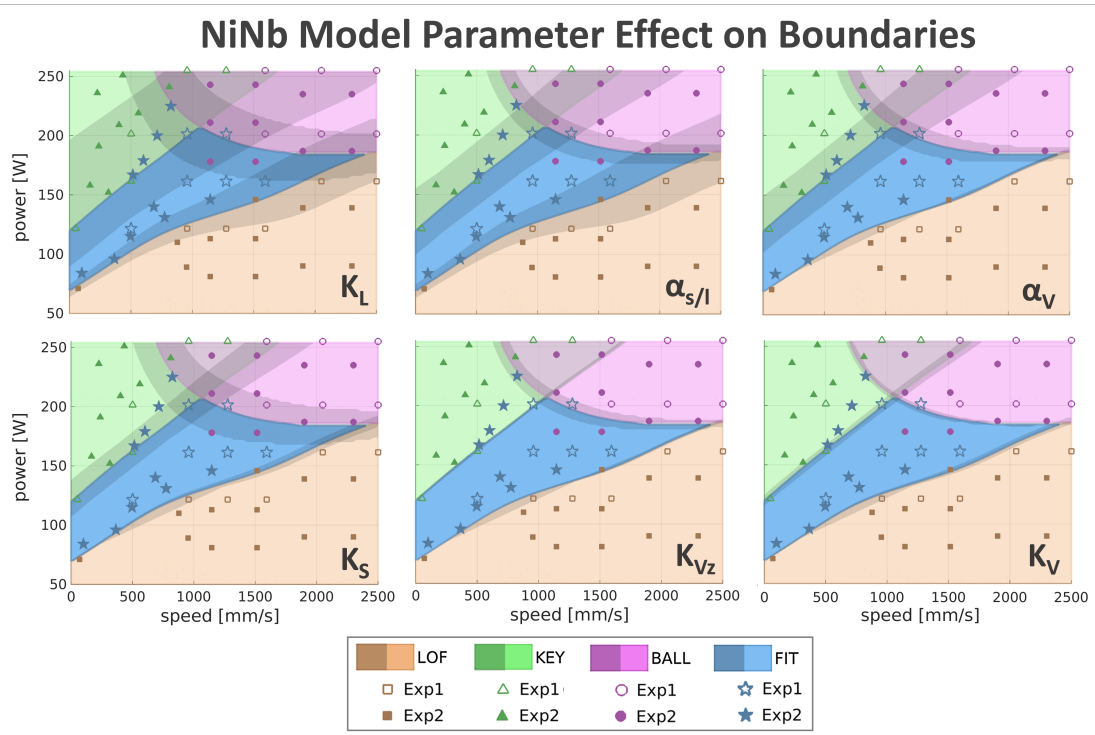

Figure 5.6: Uncertainty bounds calculated from a Monte Carlo based uncertainty propagation. Predicted regions are as follows: good quality (blue,G), keyholing (green,KEY), balling (purple,BALL), and Lack of Fusion(orange,LOF). Experimentally observed morphologies throughout the process parameters space are indicated by markers of different shapes that following the same color scheme as the predicted regions. Hollow and filled markers indicate if the data is from Exp1 or Exp2, respectively. The 6 plots correspond to the 6 key thermo-physical properties listed in the lower right corners. Liquid conductivity K_L has the largest impact on all boundaries while the the two absorptivity parameters ($\alpha_{S/L}$ and α_V) have the largest impact on the keyhole boundary which agrees with their intended purpose. Solid conductivity K_S affects balling the most and the two vapor conductivities (K_V and K_{Vz}) have little to no impact.

The parameters are arranged in order of their influence on the boundaries with liquid conductivity K_L being the most influential and K_V being the least influential. Some interesting observations can be made when comparing the relative boundary thicknesses within each map. For example, K_S has a relatively strong influence on the balling boundary as compared to the keyhole and lack-of-fusion boundaries. This can be interpreted as K_s having a stronger influence on length, rather than width or depth of the melt pool. Conversely, $\alpha_{s/l}$ preferentially influences the keyhole and lack-of-fusion boundaries, meaning that it does not affect melt pool length as much. The primary

influence of α_v is on the keyhole boundary which is consistent with its implementation as a method for approximating increased laser absorptivity during keyhole formation.

When comparing boundary uncertainties among different parameters, K_L is quite clearly the most influential for all boundaries. Unfortunately, K_L is the least understood conductivity value and varies significantly between different Finite Element models found in the literature. This issue stems from a general lack of experimental conductivity measurements of liquid metal alloys, as well as the artificial increase of the parameter in Finite Element models as a proxy for convective heat transfer within the melt pool. The small influence of vapor conductivity values K_V and K_{Vz} are the result of the relatively narrow ranges of input values provided for the uncertainty propagation.

5.4.2 Printability Maps for CoCrFeMnNi High Entropy Alloy

The same process used to predict the printability map for the Ni-5wt.%Nb alloy was applied to an equiatomic CoCrFeMnNi high entropy alloy system. The resulting printability maps can be seen in Figure 5.7. These maps have the same general topology as the Ni-5wt.%Nb maps above, but the spacing and relative size of the regions is completely different and further highlights the strong coupling between alloy and process parameter space when determining suitable protocols for AM.

In contrast to the Ni-5wt.%Nb alloy, the investigation of HEA was not as comprehensive and its printability was only investigated in a rather narrow region of the processing space. While there are not as many single track observations to indicate exactly where each print region is located experimentally, there is an obvious over-prediction of the balling region in the Finite Element map. Taking a lesson from the uncertainty analysis performed in the Ni-5wt.%Nb system, this can be attributed to uncertainty in the liquid conductivity of this system. Nevertheless, predictions of the keyhole and lack-of-fusion boundaries agree very well with experimentally determined morphologies, shown as markers of different colors and shapes in Figure 5.7.

Again, the Finite Element model outperforms the predictive capability of the Eagar-Tsai model for the same reasons discussed in the Ni-5wt.%Nb case. In the Eagar-Tsai model, oversimplifica-

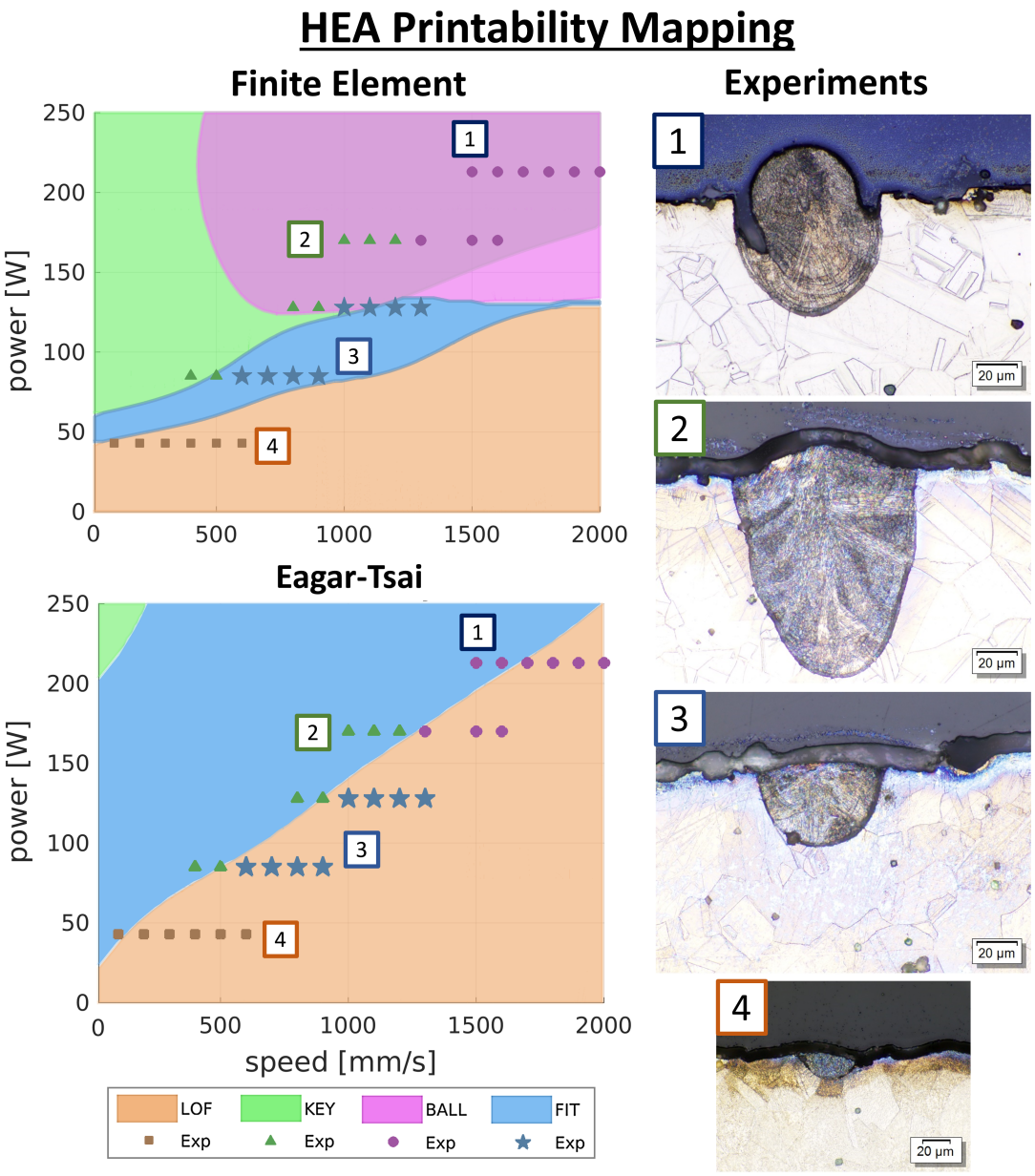

Figure 5.7: Printability maps that predict melt pool morphology regions for a CoCrFeMnNi high entropy alloy. Predicted regions are as follows: good quality (blue,G), keyholing (green,KEY), balling (purple,BALL), and Lack of Fusion(orange,LOF). Experimentally observed morphologies throughout the process parameters space are indicated by markers of different shapes that following the same color scheme as the predicted regions. There is generally good agreement between computations and experiments here, but the size of the balling region seems to be over predicted. Four representative melt pool cross sections from each region can be seen on the right. Eagar-Tsai predictions are essentially uninformative in this case due to constant material properties and no phase transformation considerations.

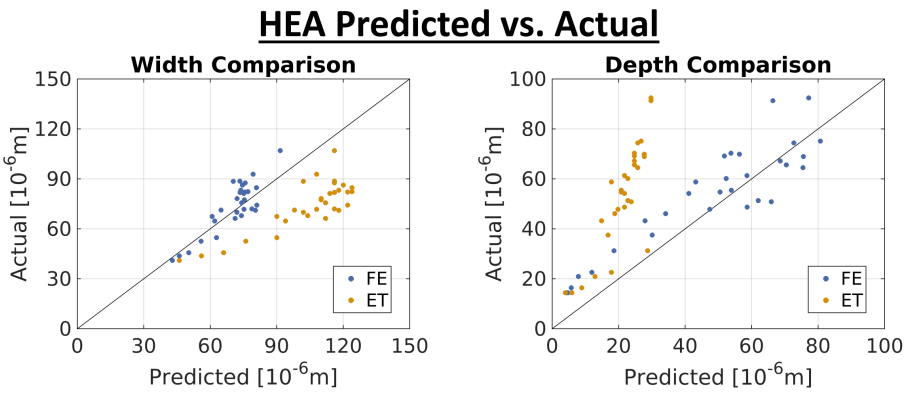

Figure 5.8: Diagnostic plots showing the predictive accuracy of the Finite Element and Eagar-Tsai models for both melt pool width and depth for the CoCrFeMnNi high entropy alloy. The Finite Element model has much better agreement with the depth as would be expected with the improved laser source term. The Eagar-Tsai model over predicts width and under predicts depth.

tion of assumptions regarding the material properties and the physics involved leads to melt pool dimensions that cannot be accurately calibrated over the entire process space. This is further corroborated by the predicted-actual comparison of the two models shown in Figure 5.8. The melt pool width is significantly significantly over-predicted, while the melt pool depth is under-predicted by the Eagar-Tsai model. The width comparison also shows the ability of the Finite Element model to capture the experimentally determined limit of melt pool width at 80-90 μm. This is attributed to the Finite Element model's ability to transition from surface to volumetric heating via inclusion of the vapor phase transformation and subsequent penetration of the laser deeper into the substrate.

5.4.3 Comparison of Printability

In addition to internal comparisons within each map, a direct comparison of printability between two materials in this study can also provide valuable insight. From both predictions **and** experiments, it is evident that Ni-5wt.%Nb has a larger printable region, under L-PBF conditions, than the CoCrFeMnNi HEA. The shape and orientation of the printable region can also tell us about the sensitivity of the material to variations in either laser power or scan speed. The more equiaxed printable region in the Ni-5wt.%Nb case indicates an equal sensitivity to both processing parameters whereas the elongated print region in the HEA case indicates a higher sensitivity

to laser power than scan speed. With this in mind we can readily conclude that the Ni-5wt.%Nb alloy is the more printable alloy in this case, based on the available evidence and computational framework.

5.5 Summary and Conclusions

The Finite Element model and melt pool dimension based methodology presented here leads to L-PBF printability maps that agree well with experiments. The consistency and accuracy of the framework applied to two drastically different alloy systems with only minor modifications is a strong indication that the approach is applicable for a wide range of materials. This is significant as this suggests that it is possible to use the proposed computational methodology for *a priori* evaluation of the suitability of an arbitrary alloy as an AM feedstock via identification of successful processing parameters, thus providing a plausible route for the *design of alloys with reduced sensitivity to machine variability during the AM process*.

The predictive capability of this printability framework can be increased through more accurate predictions of uncertainty. If experimental melt pool measurements exist for a particular alloy *a priori*, the uncertainty surrounding these boundaries can be more accurately defined by performing a Bayesian calibration of the thermo-physical parameters of the model [19]. This would result in input value distributions that are specifically defined for the particular problem at hand. This option is not necessarily viable when considering computational alloy design since the alloy being optimized has, by definition, never been experimentally tested. However better definitions of the uncertainty prior to optimization increase the chances of success.

In addition to better understanding of the uncertainty, accuracy of the printable region boundaries may be increased with the inclusion of additional physics such as free surface fluid flow modeling. However, this increase in model complexity will result in an increase in computational expense that may preclude its use in an iterative optimization scheme. With this in mind, the Finite Element based thermal model presented in this work represents a good middle ground between the fast but less accurate Eagar-Tsai approach and the slow but more accurate models that incorporate fluid dynamics.

The direct connection between the composition and resultant printability of an alloy can be incorporated into an iterative optimization scheme by utilizing quantitative measurements of the size and shape of the blue printable regions in Figures 5.3 and 5.7 as design metrics. For example, one could increase the robustness of an existing alloy to variations in processing parameters and environmental conditions by using such an optimization scheme to determine adjustments in alloy composition that would maximize the size of the printable region. Development of a more accurate method to link composition and phase-dependent thermo-physical properties (i.e. more complicated than the rule-of-mixture model used in the Ni-5wt.%Nb case above) will need to be considered if the optimization extends beyond regions where a dilute solution approximations can be used.

We would like to note that defining the printable region is just the first step in optimizing the performance of AM processed parts. Once the printable region is defined, selection of a particular set of process parameters within that region can be determined through optimization of other important material phenomena such as solidification front morphology, secondary phase evolution, and evaporative control of alloy composition. Furthermore, quantifying the uncertainty in boundary locations as shown in Figure 5.6 is important when optimizing within the printable region itself and could provide further input as to the most effective uncertainty quantification exercise to carry out based on the effect of a specific quantity of interest on the variance in the printability map of a given alloy.

6. CONCLUSIONS AND FUTURE WORK

The work detailed in this dissertation has emphasized the importance of design methodologies in the development and discovery of materials. As a discipline, design provides formalized methods for quantifying and optimizing the behaviour of complex systems. One can apply design methodologies to materials by thinking of them as a hierarchical system of interrelated physical phenomena; the elemental makeup and processing of a material results in a specific microstructure which in-turn possesses particular properties. In order to formulate a design problem, the relationships between these physical phenomena must be quantified in some way. Identifying important phenomena and decisions about what levels of detail they should be modeled at are some of the primary use cases for design. At its best, this approach results in the construction of a common theoretical understanding of the problem, which lowers the communication barrier between computational and experimental-minded persons and allows for more time and energy to be focused on solving the problem at hand. The result is faster identification of potential areas of improvement for existing materials along with improved chances of discovering new materials when using more exploratory techniques. Both local optimization and global exploration are aided by considering the uncertainty and/or variability in both the current state of knowledge and the predictive models trained on that knowledge.

After discussion of the four works contained herein it is apparent that aspects from each can be combined to create a more holistic framework for the design of materials and processes for additive manufacturing. The Efficient Global Optimization techniques from Chapter 2 can be combined with the steady state and transient thermal simulations from Chapters 4 and 5 to optimize material properties and processing pathways, while the sensitivity analysis from Chapter 3 can be used to more accurately gauge the certainty in those designs. To guide the way forward, the current chapter will be broken into a brief overview of the current methods and how they can be extended and combined, with the discussion focusing primarily on application of the concepts within the

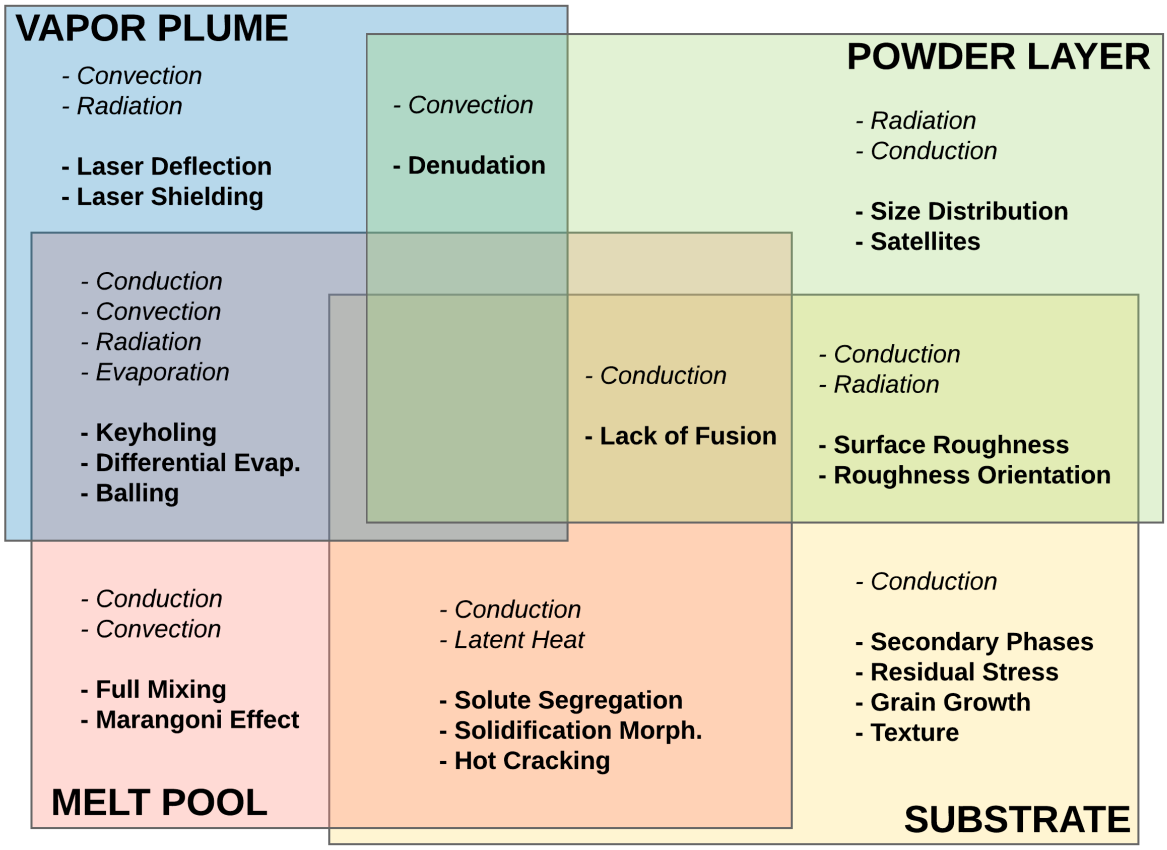

Figure 6.1: Graphic showing the relevant physical phenomena during laser-matter interactions. Each colored square represents a different domain while the overlapping regions corresponding to the interactions between those domains. Relevant transport phenomena are *italicized* and the resultant phenomena are **bolded**.

context of additive manufacturing. A graphic summarizing the physical phenomena relevant to additive manufacturing can be seen in Figure 6.1

While the finite element based methods presented in Chapters 4 and 5 are useful, there are many more physical phenomena which need to be included in order to truly design materials for use additive manufacturing, as can be seen in Figure 6.1. These phenomena, shown in relationship to material domains they are associated with, can also be placed into two main categories: short range effects within the melt pool and its interfaces, and long range effects that occur in the solid. These phenomena have a significant impact (both positive and negative) on the potential performance

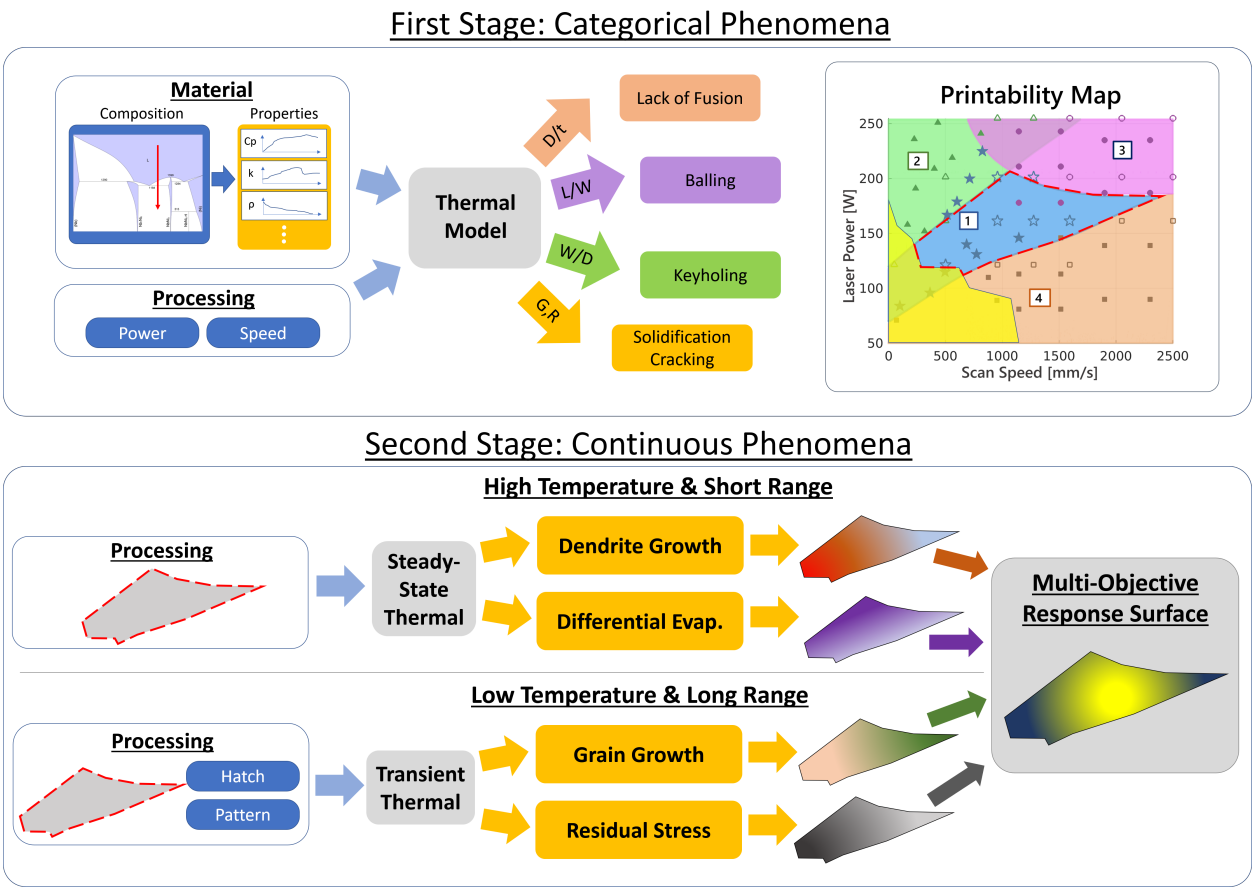

Figure 6.2: Summary of a more holistic framework that extends the framework developed in Chapter 5 by including additional phenomena and a two-stage approach to optimizing the material itself. The first stage defines the defect-free region in process parameter space while the second stage searches this feasible region in order to optimize some multi-objective design metric. Orange items in the workflow have yet to be fully implemented.

of any additively manufactured alloy. It was shown in Chapter 5 that adding constraints to avoid regions of the design space where these phenomena occur can help narrow down the feasible operating range of a potential alloy before any experiments have been performed. In order to include the additional phenomena, the framework of that chapter should be extended and refined. A schematic of this more holistic framework is shown in Figure 6.2.

There are two main areas of improvement that should be considered during the next steps of developing this framework for alloy design in additive manufacturing. The first step should be a more accurate model for the prediction of thermophysical properties from composition. The second goal

should be the extension of the framework into a two stage process involving categorical exclusion of phenomena followed by iterative optimization of the continuously varying phenomena.

6.1 Thermophysical Properties

The dependence of thermophysical properties on composition needs to be extended beyond the simple rule of mixtures shown in Chapter 5 if the framework is to be used for the exploration of new materials. This is because materials exploration will, by definition, drive the alloy composition away from the dilute regions of composition space where a rule of mixtures approach is valid. Toda-Carballo et. al. have an excellent paper detailing the difficulties of this pursuit in which they group thermophysical properties into different categories, based on how difficult they are to calculate [214]. In that paper, they use machine learning methods such as principle component analysis to show that properties like density and specific heat are relatively easy to calculate while thermal conductivity is much more difficult, due to its dependence on microstructure as well as composition.

Beyond thermophysical properties of the solid phase, measurement of liquid and vapor conductivities is inherently difficult, due to an inability to remove the convective effects of gravity and surface tension during experimental measurements. The most precise measurements are taken in microgravity experienced either during parabolic flights or on the International Space Station [216]. These complicated experiments require a tremendous amount of effort to ascertain the true thermophysical property values associated with the liquid alloy, and may not be necessary for the purposes of additive manufacturing, which primarily takes place under the influence of the earth's gravitational field. From the modeling and prediction perspective, the Wiedmann-Franz relationship is a good first approximation relating the thermal and electrical conductivities of a material at high temperatures. This useful since electrical conductivity is often easier to measure directly and is not strongly influenced by convective flow in the liquid [217]. In addition to thermal conductivity, surface tension and its dependence on temperature play an important role in Marangoni convection, which can significantly change the shape of the melt pool profile [57]. As such, it must be predicted as accurately as possible during the optimization of any new alloy.

A summary of thermophysical property values and physics-based calculation methods can be found in the many reference books on the subject [217, 215, 218, 209]. Additionally, it has been shown that machine learning methods can be used to link alloy composition to thermophysical properties like conductivity, specific heat and density [219, 220, 221, 215, 222]. Similar methods have been used to predict mechanical properties of materials as well [223]. Regardless of the type of model, experimental measurements of these properties should be included as often as possible. The ASM handbook chapter by Valencia and Quested contains the most concise descriptions of these phenomena and is a great source of references in addition to property values for pure metals and a select set of alloys [217]. The book(s) by Iida and Guthrie on the thermophysical properties of liquid metal are particularly enlightening and provide a good context for understanding the relevant phenomena within the liquid phase [215, 218]. Smithell's reference book has the most comprehensive set of data in terms of breadth across many alloy systems [209]. Preliminary research, in collaboration with Citrine Informatics, has produced a machine learning model for the prediction of thermal conductivity, density, and melting point across a wide range of materials. The dataset associated with this model consists of data extracted from Smithell's reference book [209] and Citrine's own internal database (accessed through the citrination platform at citrination.com).

6.2 Hierarchical Material Design

The idea of this hierarchical or two-stage design stems from the fact that the phenomena listed in Figure 6.1 can be sorted into either categorical or continuous data. Categorical phenomena can be eliminated outright in the first step through the use of constraints within the design space. Subsequently, the continuous phenomena can be used to optimize the performance of the as-printed part within the constraints imposed by that first step. Fortunately, this delineation between continuous and categorical phenomena is aligned with the separation between high temp melt pool considerations and low temp long range phenomena seen in the solid part/substrate. This means that relatively cheap steady-state calculations constrain the feasible design space which reduces the range of values that the more expensive long-range transient calculations must span, thus in-

creasing the overall efficiency of the framework. Sections 6.2.1 and 6.2.2 discuss the details of including additional phenomena into the framework.

6.2.1 Categorical Phenomena

Keyholing, Balling, Lack-of-fusion, and Solidification Cracking (SC) are all the result of interactions between the melt pool and its surrounding environment. It is important to consider these categorically removable phenomena first, since there is no point in optimizing over process parameters combinations that result in unstable melt pools which are prone to defect formation. Additionally, these issues are not typically the result of transient melt pool conditions so they can be modeled using a steady-state simulation technique like the one detailed in Chapter 5. In fact, solidification cracking can simply be added on as an additional constraint, which begs the question of how to identify regions prone to SC within the process parameter space of laser power and scan speed. In order to develop an answer for this, one can turn to the welding research community, which has been studying this issue for much longer than the AM community.

6.2.1.1 Solidification Cracking

The various types of cracking during solidification can be categorized as either grain or subgrain effects. In both cases, SC is generally considered to occur as the result of internal stress build up which is primarily a function of solid-liquid interface morphology [224]. Pockets of liquid surrounded by solidified metal act as stress concentrators for the internal stresses that build up during thermal cycling of the as-printed part [225]. SC and brittle phase formation become stress concentrations that significantly reduce the performance-life of the weld.

At the grain level, the shape of the melt pool plays an important role in eliminating centerline SC. Teardrop shaped weld pools promote grain growth perpendicular to the path of the melt pool, leading to liquid entrapment and crack formation at the centerline where the two opposing solidification fronts meet. At the subgrain level, the issue is not between solidification fronts, but interdendritic regions within the so-called "mushy zone" of the solid liquid interface. Furthermore, partitioning of solute elements between the solid and liquid can lead to localized enrichment of the

last liquid to solidify, which increases the likelihood of forming unwanted brittle secondary phases in those centerline or interdendritic regions.

Taking a step back, SC can generally be explained by considering the evolution of solid phase-fraction during the transition across solidus, liquidus, coherency and critical temperatures within the 2-phase region of the phase diagram. Each region enclosed by these transition temperatures has a proposed solidification mechanism that manifests as different forms of SC. The high temperature range (above the coherent temperature) is mostly liquid and as such has no issues. The region between coherency and critical temperatures still has enough liquid to repair any cracks that form. Below the critical temperature, there is still liquid in the system, but the pores are not interconnected and internal stresses begin to build due to thermal contraction and dendrite bridging. Clyne proposed a metric for crack susceptibility that considers the ratio between time spent in the safe and vulnerable temperature ranges of the two-phase region [226]. Obviously, minimizing the amount of time spent in the vulnerable region reduces the chances of SC formation.

Calculations of this ratio of times can be accomplished through implementation of solidification models as simple as Scheil solidification or as complicated as a full phase field simulation of the solid-liquid interface. Kou has two very detailed papers discussing all of these issues and proposing yet another model for predicting the susceptibility of a alloy to hot cracking [227, 228]. These articles take a mass balance approach to modeling hot crack susceptibility by defining a representative domain between two grains/cells/dendrites, then calculating conditions for hot cracking as an imbalance of liquid influx and solid outflux. The main point of that work is that hot cracking can be reduced by reducing the maximum slope of the transformation dT/df_s near complete solidification $f_s = 1$. The reasoning is that these late slopes in the transformation rate lead to long liquid channels between grains which increases the chances of liquid enclosure and limits backfilling. The article by Kou also mentions the effect of filler metals on the phase transformation slopes to show that changes in composition can have a significant effect on SC. This alloy modification approach has been successfully used many times in welding cases [229] and is the key

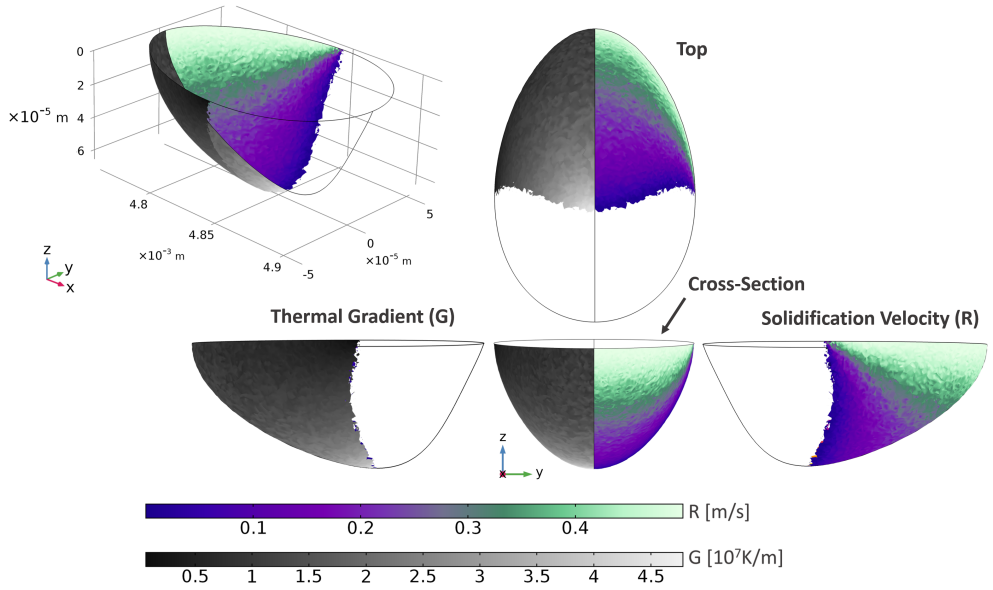

Figure 6.3: Diagram showing the spatial variation of thermal gradient G and solidification speed R across the solidification boundary. The boundary is defined as the T_{melt} isotherm within a representative finite element simulation for a laser power of 162 [W] and 500 [mm/s] for a Ni-5wt.%Nb alloy. These predicted values can be used to predict phenomena at the solid-liquid interface such as solidification cracking and cellular, dendrite, or planar growth.

consideration in a recent highly cited publication that used a Zirconium based inoculant to modify the phase-fraction evolution of a previously unweldable high strength Aluminum alloy [14].

Any of the SC prediction techniques discussed above could be applied to the melt pool thermal profiles generated from the framework described in Chapter 5. The results for each combination of laser power and scan speed should be expressed as a percentage of the melt pool boundary that is susceptible to SC phenomena. This percentage of SC susceptibility should be calculated from pointwise applications of one of the above models at each point on the solidification front since the size of the mushy zone varies throughout the melt pool boundary. Selection of the appropriate model will be based on a balance between the required speed and accuracy. An example of the predicted solidification boundary from these Finite Element simulations can be seen in Figure 6.3, with color maps representing the predicted solidification speed R and thermal gradient G at each point along the melt pool boundary.

6.2.2 Continuous Phenomena

Once all undesired phenomena have been categorically eliminated (First Stage in Figure 6.2), one can begin to optimize the performance of an as-built part within the remaining feasible region in processing space (Second Stage in Figure 6.2). The second stage of Figure 6.2 lists some examples of high temperature phenomena (Dendrite Growth and Differential Evaporation) that can be optimized by altering process parameters such as laser power, scan speed; and low temperature phenomena (Grain Growth and Residual Stress) that are subject to the additional influences of scan strategy parameters such as hatch distance and hatch patterning. The rest of this section will be devoted to the general discussion of models used to predict these phenomena, as well as preliminary results in the case of solidification morphology.

6.2.2.1 Solidification Morphology

In addition to providing information for the calculation of SC susceptibility, the location specific G and R values seen in Figure 6.3 can be used to predict whether the solidification front at a specific point will be columnar, dendritic, or planar [64]. If a higher level of detail is required, this gradient and velocity data can also be fed to high fidelity phase-field simulations which can calculate the spatial microstructural evolution of the transformation front. These simulations produce quantitative predictions of microstructural length scales and composition, while also automatically transitioning between planar, cellular and dendritic solidification modes. Preliminary results from this work can be seen in Figure 6.4.

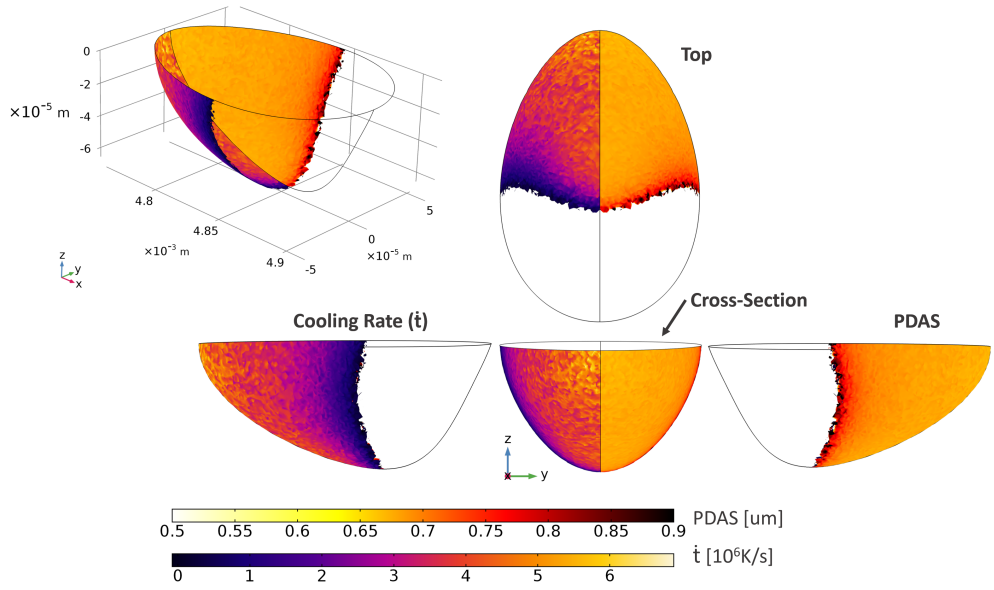

Figure 6.4: Diagram showing the spatial variation of cooling rate $\dot{t}$ and primary dendrite arm spacing $PDAS$ across the solidification boundary. The boundary is defined as the T_{melt} isotherm within a representative finite element simulation for a laser power of 162 [W] and 500 [mm/s] for a Ni-5wt.%Nb alloy. Statistics summarizing the range of $PDAS$ across the solidification boundary can be used to guide the selection of optimal processing parameters.

Predicted primary dendrite arm spacing (PDAS) in Figure 6.4 is calculated across the solidification front via an exponential relationship between PDAS and cooling rate ($PDAS = 125.1\dot{t}^{-0.5027} + 0.1671$) which is derived from phase-field simulations of the NiNb system. Maps showing how PDAS varies with laser power and scan speed can be established by applying this calculation to steady-state FE simulation results throughout the feasible region in processing space.

6.2.2.2 Differential Evaporation

Differential evaporation is a useful phenomena that enables localized composition control as a design variable. Simple representations of this phenomena are already implemented within the existing Finite Element models through the equations used to approximate evaporative cooling. The temperature dependent vapor pressures of individual elements in the melt can be used to calculate a rough approximation of the change in composition due to differential evaporation [230,

231]. For steady-state simulations, an approximation of the total compositional change associated with a single melt pool cycle can be calculated by performing a double integral of the mass flow rate $\dot{m}$ that has been subject to transformation from spatial to temporal coordinate by diving all x-values by the scan speed V. Mapping of differential evaporation onto the process parameter space will consist of extracting the evaporation rate predictions of each element from individual steady state FE simulations throughout the feasible region.

6.2.2.3 Grain Growth and Residual Stress

Other continuous phenomena of interest such as residual stress and grain growth/texture evolution occur at lower temperature and longer length scales associated with the conduction of thermal energy through the solid part/substrate. As such, transient models like the one detailed in Chapter 4 must be used to predict thermal histories resulting from multiple laser passes and multiple layers.

6.3 Concluding Remarks

One of the key barriers to widespread adoption of additively manufactured parts in load-bearing engineering applications is the lack of consistent performance across as-printed components. With this in mind, research efforts (both academic and industrial) should be focused on understanding this issue of variability. While most scientists and engineers agree with this statement, there is a distinct lack of a consensus on what aspects of the problem to actually focus on. A large portion of this dissonance stems from disagreements about the validity of certain assumptions about crucial steps in the entire additive manufacturing process. For example, many Much of this can be attributed to the fact that we dont fully understand the fundamental phenomena associated with turning metallic powder into end-use parts. *Before trying to optimize the AM process as a whole, researchers should first focus on verifying the assumptions related to the most likely sources of variability throughout the process*. The entire manufacturing process can be broken into pieces through the use of a functional diagram that provides a detailed accounting of the flow of materials and energy through the machine, from initial powderization of the feedstock alloy, through transportation/storage/loading of the powder into the machine, all the way to the extraction and post

processing of the as-built part. Breaking the process into its basic subprocesses helps formalize the task of identifying key sources of variability that should be the topics of future research. Abstracting the complicated full process into its basic subprocesses also helps expand the search for existing literature to other disciplines that may have already studied that problem. For example, modifying a common search term like "selective laser melting" into more generalized terms associated with "depositing energy to melt metal" will return literature from laser processing and welding communities which much more complete and formalized understanding of the process of localized melting with a moving heat source interactions due to their longer histories [21, 200, 40, 39].

Once the key subprocesses that lead to high variability have been identified, the task should shift to reducing or mitigating that variability. To accomplish this, the majority of additive manufacturing research projects today (including the works contained within this dissertation) simplifies the problem considerably by trying to identify an optimal set of process parameters that remain static throughout the entire build. One must always be careful when simplifying a problem to this extent; taking this approach contains a very optimistic assumption that one set of process parameters are applicable throughout the entire build. This mindset is likely an artifact of comparisons commonly made between additive manufacturing and subtractive methods such as CNC milling. At first glance, this analogy makes sense: both methods are automated material processing techniques that create complicated components of similar size for similar end-use applications. While these two technologies do compete in terms of their ability to create end-use parts for specific applications, the technical challenges of each process are completely different from a materials processing perspective. This stems from the fact that additive processes fundamentally alter the intrinsic material properties within the as-built parts upon melting and solidification. A more apt comparison is that of an industrial material processing plant, such as a steel mill, which requires constant inline monitoring and feedback controls to maintain consistency of the outgoing product. With this in mind, another key area of research for the future of additive manufacturing is the development of inline monitoring and control techniques. The goal of this type of research should be to shift away from end-to-end processing modeling of an entire build in favor of developing in-situ

monitoring and process control techniques that can calculate the real-time susceptibility of defect generation and adjust the process parameters accordingly. An approach of this type would likely be enhanced by additional background research on Control Theory and/or close collaborations with other researchers familiar with the topic.

REFERENCES

[1] G. Pahl and W. Beitz, *Engineering design: a systematic approach*. Springer Science & Business Media, 2013.

[2] G. B. Olson, "Computational design of hierarchically structured materials," *Science*, vol. 277, no. 5330, pp. 1237–1242, 1997.

[3] M. F. Ashby, S. F. Bush, N. Swindells, R. Bullough, G. Ellison, Y. Lindblom, R. W. Cahn, and J. F. Barnes, "Technology of the 1990s: Advanced materials and predictive design [and discussion]," *Philosophical Transactions of the Royal Society of London. Series A, Mathematical and Physical Sciences*, vol. 322, no. 1567, pp. 393–407, 1987.

[4] G. B. Olson, "Designing a new material world," *Science*, vol. 288, no. 5468, pp. 993–998, 2000.

[5] B. Cantor, I. T. H. Chang, P. Knight, and A. J. B. Vincent, "Microstructural development in equiatomic multicomponent alloys," *Materials Science and Engineering: A*, vol. 375-377, pp. 213–218, 2004.

[6] Y. Brif, M. Thomas, and I. Todd, "The use of high-entropy alloys in additive manufacturing," *Scripta Materialia*, vol. 99, pp. 93–96, 2015.

[7] K. Otsuka and X. Ren, "Physical metallurgy of TiNi-based shape memory alloys," *Progress in Materials Science*, vol. 50, no. 5, pp. 511–678, 2005.

[8] D. T. Fullwood, S. R. Niezgoda, and S. R. Kalidindi, "Microstructure reconstructions from 2-point statistics using phase-recovery algorithms," *Acta Materialia*, vol. 56, no. 5, pp. 942–948, 2008.

[9] D. T. Fullwood, S. R. Niezgoda, B. L. Adams, and S. R. Kalidindi, "Microstructure sensitive design for performance optimization," *Progress in Materials Science*, vol. 55, no. 6, pp. 477–562, 2010.

[10] J. P. Holdren, "Materials genome initiative for global competitiveness," *National Science and Technology Council OSTP. Washington, USA*, 2011.

[11] J. Allison, "Integrated computational materials engineering: A perspective on progress and future steps," *JOM*, vol. 63, pp. 15–18, 04 2011.

[12] A. Agrawal and A. Choudhary, "Perspective: Materials informatics and big data: Realization of the fourth paradigm of science in materials science," *APL Materials*, vol. 4, no. 5, p. 053208, 2016.

[13] B. Meredig, A. Agrawal, S. Kirklin, J. E. Saal, J. W. Doak, A. Thompson, K. Zhang, A. Choudhary, and C. Wolverton, "Combinatorial screening for new materials in unconstrained composition space with machine learning," *Physical Review B*, vol. 89, no. 9, p. 094104, 2014.

[14] J. H. Martin, B. D. Yahata, J. M. Hundley, J. A. Mayer, T. A. Schaedler, and T. M. Pollock, "3d printing of high-strength aluminium alloys," *Nature*, vol. 549, no. 7672, pp. 365–369, 2017.

[15] B. Cowles, L. Cowles Consulting, C. Tolland, D. Backman, and R. Dutton, "The development and implementation of integrated computational materials engineering (icme) for aerospace applications," *Models, Databases and Simulation Tools Needed for Realization of Integrated Computational Mat. Eng.(ICME 2010)*, p. 44, 2014.

[16] D. McDowell and F. Dunne, "Microstructure-sensitive computational modeling of fatigue crack formation," *International journal of fatigue*, vol. 32, no. 9, pp. 1521–1542, 2010.

[17] T. Lookman, F. J. Alexander, and K. Rajan, eds., *Information Science for Materials Discovery and Design*. Springer Series in Materials Science, Springer International Publishing, 2016.

[18] G. Tapia, L. Johnson, B. Franco, K. Karayagiz, J. Ma, R. Arroyave, I. Karaman, and A. Elwany, "Bayesian Calibration and Uncertainty Quantification for a Physics-Based Precipitation Model of NickelTitanium Shape-Memory Alloys," *Journal of Manufacturing Science and Engineering*, vol. 139, no. 7, pp. 071002–071002–13, 2017.

[19] M. Mahmoudi, G. Tapia, K. Karayagiz, B. Franco, J. Ma, R. Arroyave, I. Karaman, and A. Elwany, "Multivariate Calibration and Experimental Validation of a 3d Finite Element Thermal Model for Laser Powder Bed Fusion Metal Additive Manufacturing," *Integrating Materials and Manufacturing Innovation*, vol. 7, no. 3, pp. 116–135, 2018.

[20] J. Elmer, P. Hochanadel, K. Lachenberg, and T. Webber, "Introduction to High Energy Density Electron and Laser Beam Welding," in *ASM Handook*, vol. 6a, pp. 507–513, ASM International, 3rd ed., 2011.

[21] J. Ion, *Laser processing of engineering materials: principles, procedure and industrial application*. Elsevier, 2005.

[22] C. R. Deckard, "Method and apparatus for producing parts by selective sintering," 1989. US Patent 4,863,538.

[23] H. Smith, "Ge aviation to grow better fuel nozzles using 3d printing. 3d printing news and trends," 2013.

[24] V. Petrovic, J. V. H. Gonzalez, O. J. Ferrando, J. D. Gordillo, J. R. B. Puchades, and L. P. Griñan, "Additive layered manufacturing: sectors of industrial application shown through case studies," *International Journal of Production Research*, vol. 49, no. 4, pp. 1061–1079, 2011.

[25] L.-E. Rännar, A. Glad, and C.-G. Gustafson, "Efficient cooling with tool inserts manufactured by electron beam melting," *Rapid Prototyping Journal*, vol. 13, no. 3, pp. 128–135, 2007.

[26] D. Brackett, I. Ashcroft, and R. Hague, "Topology optimization for additive manufacturing," in *Proceedings of the solid freeform fabrication symposium, Austin, TX*, vol. 1, pp. 348–362, S, 2011.

[27] L. D. Bobbio, R. A. Otis, J. P. Borgonia, R. P. Dillon, A. A. Shapiro, Z.-K. Liu, and A. M. Beese, "Additive manufacturing of a functionally graded material from ti-6al-4v to invar: Experimental characterization and thermodynamic calculations," *Acta Materialia*, vol. 127, pp. 133–142, 2017.

[28] D. C. Hofmann, J. Kolodziejska, S. Roberts, R. Otis, R. P. Dillon, J.-O. Suh, Z.-K. Liu, and J.-P. Borgonia, "Compositionally graded metals: A new frontier of additive manufacturing," *Journal of Materials Research*, vol. 29, no. 17, pp. 1899–1910, 2014.

[29] J. Ma, B. Franco, G. Tapia, K. Karayagiz, L. Johnson, J. Liu, R. Arroyave, I. Karaman, and A. Elwany, "Spatial Control of Functional Response in 4d-Printed Active Metallic Structures," *Scientific Reports*, vol. 7, p. srep46707, 2017.

[30] S. Dadbakhsh, M. Speirs, J.-P. Kruth, J. Schrooten, J. Luyten, and J. Van Humbeeck, "Effect of SLM Parameters on Transformation Temperatures of Shape Memory Nickel Titanium Parts," *Advanced Engineering Materials*, vol. 16, no. 9, pp. 1140–1146, 2014.

[31] R. R. Dehoff, M. M. Kirka, F. A. List, K. A. Unocic, and W. J. Sames, "Crystallographic texture engineering through novel melt strategies via electron beam melting: Inconel 718," *Materials Science and Technology*, vol. 31, no. 8, pp. 939–944, 2015.

[32] R. R. Dehoff, M. M. Kirka, W. J. Sames, H. Bilheux, A. S. Tremsin, L. E. Lowe, and S. S. Babu, "Site specific control of crystallographic grain orientation through electron beam additive manufacturing," *Materials Science and Technology*, vol. 31, no. 8, pp. 931–938, 2015.

[33] W. J. Sames, F. A. List, S. Pannala, R. R. Dehoff, and S. S. Babu, "The metallurgy and processing science of metal additive manufacturing," *International Materials Reviews*, vol. 61, no. 5, pp. 315–360, 2016.

[34] S. A. Khairallah, A. T. Anderson, A. Rubenchik, and W. E. King, "Laser powder-bed fusion additive manufacturing: Physics of complex melt flow and formation mechanisms of pores, spatter, and denudation zones," *Acta Materialia*, vol. 108, pp. 36–45, 2016.

[35] J. Trapp, A. M. Rubenchik, G. Guss, and M. J. Matthews, "In situ absorptivity measurements of metallic powders during laser powder-bed fusion additive manufacturing," *Applied Materials Today*, vol. 9, pp. 341–349, 2017.

[36] M. Foster, R. Beaulieu, L. Blais, G. Caron, and M. Langlois, "Experimental investigation on stainless steel welding with a 15 kW fibre laser," *Canadian Journal of Physics*, vol. 92, no. 3, pp. 246–252, 2013.

[37] Y. Kawahito, K. Kinoshita, N. Matsumoto, M. Mizutani, and S. Katayama, "Effect of weakly ionised plasma on penetration of stainless steel weld produced with ultra high power density fibre laser," *Science and Technology of Welding and Joining*, vol. 13, no. 8, pp. 749–753, 2008.

[38] M. Markl, R. Ammer, U. Rüde, and C. Körner, "Numerical investigations on hatching process strategies for powder-bed-based additive manufacturing using an electron beam," *The International Journal of Advanced Manufacturing Technology*, vol. 78, no. 1-4, pp. 239–247, 2015.

[39] M. Allmen and A. Blatter, *Laser-Beam Interactions with Materials: Physical Principles and Applications*. Springer series in materials science, Berlin, Heidelberg: Springer Berlin Heidelberg, second, updated edition ed., 1995.

[40] S. I. Anisimov and V. A. Khokhlov, *Instabilities in Laser-Matter Interaction*. CRC Press, 1995.

[41] D. Lacroix, G. Jeandel, and C. Boudot, "Spectroscopic characterization of laser-induced plasma created during welding with a pulsed Nd:YAG laser," *Journal of Applied Physics*, vol. 81, pp. 6599–6606, May 1997.

[42] T. J. Rockstroh and J. Mazumder, "Spectroscopic studies of plasma during cw laser materials interaction," *Journal of Applied Physics*, vol. 61, pp. 917–923, Feb. 1987.

[43] R. Lober and J. Mazumder, "Spectroscopic diagnostics of plasma during laser processing of aluminium," *Journal of Physics D: Applied Physics*, vol. 40, pp. 5917–5923, Oct. 2007.

[44] L. Song and J. Mazumder, "Real Time Cr Measurement Using Optical Emission Spectroscopy During Direct Metal Deposition Process," *IEEE Sensors Journal*, vol. 12, no. 5, pp. 958–964, 2012.

[45] A. J. Dunbar and A. R. Nassar, "Assessment of optical emission analysis for in-process monitoring of powder bed fusion additive manufacturing," *Virtual and Physical Prototyping*, vol. 13, no. 1, pp. 14–19, 2018.

[46] K. Bartkowiak, "Direct laser deposition process within spectrographic analysis in situ," *Physics Procedia*, vol. 5, pp. 623–629, 2010.

[47] A. Masmoudi, R. Bolot, and C. Coddet, "Investigation of the laserpowderatmosphere interaction zone during the selective laser melting process," *Journal of Materials Processing Technology*, vol. 225, pp. 122–132, 2015.

[48] M. Matthews, J. Trapp, G. Guss, and A. Rubenchik, "Direct measurements of laser absorptivity during metal melt pool formation associated with powder bed fusion additive manufacturing processes," *Journal of Laser Applications*, vol. 30, p. 032302, Aug. 2018.

[49] J. Xu, Y. Luo, L. Zhu, J. Han, C. Zhang, and D. Chen, "Effect of shielding gas on the plasma plume in pulsed laser welding," *Measurement*, vol. 134, pp. 25–32, 2019.

[50] Y. Luo, X. Tang, F. Lu, Q. Chen, and H. Cui, "Effect of subatmospheric pressure on plasma plume in fiber laser welding," *Journal of Materials Processing Technology*, vol. 215, pp. 219–224, 2015.

[51] C. D. Boley, S. A. Khairallah, and A. M. Rubenchik, "Calculation of laser absorption by metal powders in additive manufacturing," *Applied Optics*, vol. 54, no. 9, pp. 2477–2482, 2015.

[52] A. V. Gusarov and J. P. Kruth, "Modelling of radiation transfer in metallic powders at laser treatment," *International Journal of Heat and Mass Transfer*, vol. 48, no. 16, pp. 3423–3434, 2005.

[53] A. V. Gusarov, I. Yadroitsev, P. Bertrand, and I. Smurov, "Model of radiation and heat transfer in laser-powder interaction zone at selective laser melting," *Journal of Heat Transfer*, vol. 131, no. 7, pp. 072101–072101–10, 2009.

[54] A. Foroozmehr, M. Badrossamay, E. Foroozmehr, and S. Golabi, "Finite Element Simulation of Selective Laser Melting process considering Optical Penetration Depth of laser in powder bed," *Materials & Design*, vol. 89, pp. 255–263, 2016.

[55] T. Heeling, M. Cloots, and K. Wegener, "Melt pool simulation for the evaluation of process parameters in selective laser melting," *Additive Manufacturing*, vol. 14, pp. 116–125, 2017.

[56] S. Pang, X. Chen, J. Zhou, X. Shao, and C. Wang, "3d transient multiphase model for keyhole, vapor plume, and weld pool dynamics in laser welding including the ambient pressure effect," *Optics and Lasers in Engineering*, vol. 74, pp. 47–58, 2015.

[57] S. Lu, H. Fujii, and K. Nogi, "Sensitivity of Marangoni convection and weld shape variations to welding parameters in O2Ar shielded GTA welding," *Scripta Materialia*, vol. 51, no. 3, pp. 271–277, 2004.

[58] Y. Wang and H. L. Tsai, "Impingement of filler droplets and weld pool dynamics during gas metal arc welding process," *International Journal of Heat and Mass Transfer*, vol. 44, no. 11, pp. 2067–2080, 2001.

[59] D. B. Hann, J. Iammi, and J. Folkes, "A simple methodology for predicting laser-weld properties from material and laser parameters," *Journal of Physics D: Applied Physics*, vol. 44, no. 44, p. 445401, 2011.

[60] K. Otsuka and X. Ren, "Physical metallurgy of TiNi-based shape memory alloys," *Progress in Materials Science*, vol. 50, no. 5, pp. 511–678, 2005.

[61] W. E. King, H. D. Barth, V. M. Castillo, G. F. Gallegos, J. W. Gibbs, D. E. Hahn, C. Kamath, and A. M. Rubenchik, "Observation of keyhole-mode laser melting in laser powder-bed fusion additive manufacturing," *Journal of Materials Processing Technology*, vol. 214, no. 12, pp. 2915–2925, 2014.

[62] X. K. Zhu and Y. J. Chao, "Effects of temperature-dependent material properties on welding simulation," *Computers & Structures*, vol. 80, no. 11, pp. 967–976, 2002.

[63] R. Komanduri and Z. B. Hou, "Thermal analysis of the arc welding process: Part II. effect of variation of thermophysical properties with temperature," *Metallurgical and Materials Transactions B*, vol. 32, no. 3, pp. 483–499, 2001.

[64] H. L. Wei, J. Mazumder, and T. DebRoy, "Evolution of solidification texture during additive manufacturing," *Scientific Reports*, vol. 5, p. 16446, 2015-11-10.

[65] P. Prabhakar, W. J. Sames, R. Dehoff, and S. S. Babu, "Computational modeling of residual stress formation during the electron beam melting process for Inconel 718," *Additive Manufacturing*, vol. 7, pp. 83–91, 2015.

[66] A. Plotkowski, O. Rios, N. Sridharan, Z. Sims, K. Unocic, R. T. Ott, R. R. Dehoff, and S. S. Babu, "Evaluation of an Al-Ce alloy for laser additive manufacturing," *Acta Materialia*, vol. 126, pp. 507–519, 2017.

[67] L. Geekie, "Including Simulation in the Additive Manufacturing Workflow," *ANSYS Advantage*, vol. 12, no. 3, p. 5, 2018.

[68] W. J. Sames, K. A. Unocic, G. W. Helmreich, M. M. Kirka, F. Medina, R. R. Dehoff, and S. S. Babu, "Feasibility of in situ controlled heat treatment (ISHT) of Inconel 718 during electron beam melting additive manufacturing," *Additive Manufacturing*, vol. 13, pp. 156–165, Jan. 2017.

[69] J. J. Lewandowski and M. Seifi, "Metal Additive Manufacturing: A Review of Mechanical Properties," *Annual Review of Materials Research*, vol. 46, no. 1, pp. 151–186, 2016.

[70] D. Ding, Z. Pan, D. Cuiuri, and H. Li, "A multi-bead overlapping model for robotic wire and arc additive manufacturing (WAAM)," *Robotics and Computer-Integrated Manufacturing*, vol. 31, pp. 101–110, 2015.

[71] M. F. Zäh and S. Lutzmann, "Modelling and simulation of electron beam melting," *Production Engineering*, vol. 4, no. 1, pp. 15–23, 2010.

[72] J. P. Kruth, L. Froyen, J. Van Vaerenbergh, P. Mercelis, M. Rombouts, and B. Lauwers, "Selective laser melting of iron-based powder," *Journal of Materials Processing Technology*, vol. 149, no. 1, pp. 616–622, 2004.

[73] A. V. Gusarov, I. Yadroitsev, P. Bertrand, and I. Smurov, "Heat transfer modelling and stability analysis of selective laser melting," *Applied Surface Science*, vol. 254, no. 4, pp. 975–979, 2007.

[74] J. Günther, F. Brenne, M. Droste, M. Wendler, O. Volkova, H. Biermann, and T. Niendorf, "Design of novel materials for additive manufacturing - isotropic microstructure and high defect tolerance," *Scientific Reports*, vol. 8, no. 1, p. 1298, 2018.

[75] P. ORegan, P. Prickett, R. Setchi, G. Hankins, and N. Jones, "Metal based additive layer manufacturing: Variations, correlations and process control," *Procedia Computer Science*, vol. 96, pp. 216–224, 2016.

[76] R. Hague, S. Mansour, and N. Saleh, "Material and design considerations for rapid manufacturing," *International Journal of Production Research*, vol. 42, no. 22, pp. 4691–4708, 2004.

[77] J. P. Kruth, G. Levy, F. Klocke, and T. H. C. Childs, "Consolidation phenomena in laser and powder-bed based layered manufacturing," *CIRP Annals*, vol. 56, no. 2, pp. 730–759, 2007.

[78] "Aluminum alloys," 2016.

[79] D. Rosenthal, "The Theory of Moving Sources of Heat and Its Application of Metal Treatments," *Transactions of ASME*, vol. 68, pp. 849–866, 1946.

[80] T. Eagar and N.-S. Tsai, "Temperature fields produced by traveling distributed heat sources," *Welding Journal (Miami, Fla)*, vol. 62, no. 12, pp. 346–355, 1983.

[81] S. Bontha, N. W. Klingbeil, P. A. Kobryn, and H. L. Fraser, "Effects of process variables and size-scale on solidification microstructure in beam-based fabrication of bulky 3d structures," *Materials Science and Engineering: A*, vol. 513-514, pp. 311–318, 2009.

[82] C. R. Noble, A. T. Anderson, N. R. Barton, J. A. Bramwell, A. Capps, M. H. Chang, J. J. Chou, D. M. Dawson, E. R. Diana, and T. A. Dunn, "Ale3d: An arbitrary Lagrangian-Eulerian multi-physics code," tech. rep., Lawrence Livermore National Lab (LLNL), Livermore, CA (United States), 2017.

[83] C. Körner, E. Attar, and P. Heinl, "Mesoscopic simulation of selective beam melting processes," *Journal of Materials Processing Technology*, vol. 211, no. 6, pp. 978–987, 2011.

[84] L. Johnson and R. Arróyave, "An inverse design framework for prescribing precipitation heat treatments from a target microstructure," *Materials & Design*, vol. 107, pp. 7–17, 2016.

[85] Y. Zhu, S. Murali, M. D. Stoller, K. J. Ganesh, W. Cai, P. J. Ferreira, A. Pirkle, R. M. Wallace, K. A. Cychosz, M. Thommes, D. Su, E. A. Stach, and R. S. Ruoff, "Carbon-Based Supercapacitors Produced by Activation of Graphene," *Science*, vol. 332, no. 6037, pp. 1537–1541, 2011.

[86] M. D. Stoller, S. Park, Y. Zhu, J. An, and R. S. Ruoff, "Graphene-Based Ultracapacitors," *Nano Letters*, vol. 8, no. 10, pp. 3498–3502, 2008.

[87] M. Pumera, "Graphene -based nanomaterials for energy storage," *Energy & Environmental Science*, vol. 4, no. 3, pp. 668–674, 2011.

[88] R. Raccichini, A. Varzi, S. Passerini, and B. Scrosati, "The role of graphene for electrochemical energy storage," *Nature Materials*, vol. 14, no. 3, pp. 271–279, 2015.

[89] M. Yang, K. Cao, Y. Q. Lang Sui, J. Zhu, A. Waas, E. M. Arruda, J. Kieffer, M. Thouless, and N. A. Kotov, "Dispersions of aramid nanofibers: a new nanoscale building block," *ACS nano*, vol. 5, no. 9, p. 6945, 2011.

[90] P. G. Balakrishnan, R. Ramesh, and T. Prem Kumar, "Safety mechanisms in lithium-ion batteries," *Journal of Power Sources*, vol. 155, no. 2, pp. 401–414, 2006.

[91] M. Armand and J.-M. Tarascon, "Building better batteries," *Nature*, vol. 451, no. 7179, pp. 652–657, 2008.

[92] J. B. Goodenough and Y. Kim, "Challenges for Rechargeable Li Batteries," *Chemistry of Materials*, vol. 22, no. 3, pp. 587–603, 2010.

[93] N. Shirshova, H. Qian, M. Houllé, J. H. G. Steinke, A. R. J. Kucernak, Q. P. V. Fontana, E. S. Greenhalgh, A. Bismarck, and M. S. P. Shaffer, "Multifunctional structural energy storage composite supercapacitors," *Faraday Discussions*, vol. 172, pp. 81–103, 2014.

[94] J. F. Snyder, R. H. Carter, and E. D. Wetzel, "Electrochemical and Mechanical Behavior in Mechanically Robust Solid Polymer Electrolytes for Use in Multifunctional Structural Batteries," *Chemistry of Materials*, vol. 19, no. 15, pp. 3793–3801, 2007.

[95] Z. Ling, C. E. Ren, M.-Q. Zhao, J. Yang, J. M. Giammarco, J. Qiu, M. W. Barsoum, and Y. Gogotsi, "Flexible and conductive MXene films and nanocomposites with high capacitance," *Proceedings of the National Academy of Sciences of the United States of America*, vol. 111, no. 47, pp. 16676–16681, 2014.

[96] H. An, J. Mike, K. A. Smith, L. Swank, Y.-H. Lin, S. L. Pesek, R. Verduzco, and J. L. Lutkenhaus, "Highly Flexible Self-Assembled V_2O_5 Cathodes Enabled by Conducting Di-block Copolymers," *Scientific Reports*, vol. 5, p. 14166, 2015.

[97] M. F. El-Kady, V. Strong, S. Dubin, and R. B. Kaner, "Laser scribing of high-performance and flexible graphene-based electrochemical capacitors," *Science (New York, N.Y.)*, vol. 335, no. 6074, pp. 1326–1330, 2012.

[98] L. Nyholm, G. Nyström, A. Mihranyan, and M. Strømme, "Toward flexible polymer and paper-based energy storage devices," *Advanced Materials (Deerfield Beach, Fla.)*, vol. 23, no. 33, pp. 3751–3769, 2011.

[99] L. E. Asp and E. S. Greenhalgh, "Structural power composites," *Composites Science and Technology*, vol. 101, pp. 41–61, 2014.

[100] E. Greenhalgh, J. Ankersen, L. Asp, A. Bismarck, Q. Fontana, M. Houlle, G. Kalinka, A. Kucernak, M. Mistry, S. Nguyen, H. Qian, M. Shaffer, N. Shirshova, J. Steinke, and M. Wienrich, "Mechanical, electrical and microstructural characterisation of multifunctional structural power composites," *Journal of Composite Materials*, vol. 49, no. 15, pp. 1823–1834, 2015.

[101] S. R. Kwon, J. Harris, T. Zhou, D. Loufakis, J. G. Boyd, and J. L. Lutkenhaus, "Mechanically Strong Graphene/Aramid Nanofiber Composite Electrodes for Structural Energy and Power," *ACS nano*, vol. 11, no. 7, pp. 6682–6690, 2017.

[102] S. R. Kwon, M. B. Elinski, J. D. Batteas, and J. L. Lutkenhaus, "Robust and Flexible Aramid Nanofiber/Graphene Layer-by-Layer Electrodes," *ACS Applied Materials & Interfaces*, vol. 9, no. 20, pp. 17125–17135, 2017.

[103] N. Shirshova, H. Qian, M. S. P. Shaffer, J. H. G. Steinke, E. S. Greenhalgh, P. T. Curtis, A. Kucernak, and A. Bismarck, "Structural composite supercapacitors," *Composites Part A: Applied Science and Manufacturing*, vol. 46, pp. 96–107, 2013.

[104] D. J. O'Brien, D. M. Baechle, and E. D. Wetzel, "Design and performance of multifunctional structural composite capacitors," *Journal of Composite Materials*, vol. 45, no. 26, pp. 2797–2809, 2011.

[105] R. F. Gibson, "A review of recent research on mechanics of multifunctional composite materials and structures," *Composite Structures*, vol. 92, no. 12, pp. 2793–2810, 2010.

[106] J. P. Thomas and M. A. Qidwai, "The design and application of multifunctional structure-battery materials systems," *JOM*, vol. 57, no. 3, pp. 18–24, 2005.

[107] H. Chen, M. B. Müller, K. J. Gilmore, G. G. Wallace, and D. Li, "Mechanically Strong, Electrically Conductive, and Biocompatible Graphene Paper," *Advanced Materials*, vol. 20, no. 18, pp. 3557–3561, 2008.

[108] Y. Zhu, S. Murali, W. Cai, X. Li, J. W. Suk, J. R. Potts, and R. S. Ruoff, "Graphene and graphene oxide: synthesis, properties, and applications," *Advanced Materials (Deerfield Beach, Fla.)*, vol. 22, no. 35, pp. 3906–3924, 2010.

[109] K. Cao, C. P. Siepermann, M. Yang, A. M. Waas, N. A. Kotov, M. D. Thouless, and E. M. Arruda, "Reactive Aramid Nanostructures as High-Performance Polymeric Building Blocks for Advanced Composites," *Advanced Functional Materials*, vol. 23, no. 16, pp. 2072–2080, 2013.

[110] M. Yang, K. Cao, L. Sui, Y. Qi, J. Zhu, A. Waas, E. M. Arruda, J. Kieffer, M. D. Thouless, and N. A. Kotov, "Dispersions of aramid nanofibers: a new nanoscale building block," *ACS nano*, vol. 5, no. 9, pp. 6945–6954, 2011.

[111] M. Yang, K. Cao, B. Yeom, M. Thouless, A. Waas, E. M. Arruda, and N. A. Kotov, "Aramid nanofiber-reinforced transparent nanocomposites," *Journal of Composite Materials*, vol. 49, no. 15, pp. 1873–1879, 2015.

[112] J. Zhu, W. Cao, M. Yue, Y. Hou, J. Han, and M. Yang, "Strong and stiff aramid nanofiber/carbon nanotube nanocomposites," *ACS nano*, vol. 9, no. 3, pp. 2489–2501, 2015.

[113] J. R. Potts, D. R. Dreyer, C. W. Bielawski, and R. S. Ruoff, "Graphene-based polymer nanocomposites," *Polymer*, vol. 52, no. 1, pp. 5–25, 2011.

[114] M. G. Ghislandi, E. Tkalya, S. Schillinger, C. E. Koning, and D. G. With, "High performance graphene- and MWCTNs-based PS/PPO composites obtained via organic solvent dispersion," *Composites Science and Technology*, vol. 80, pp. 16–22, 2013.

[115] B. Park, W. Lee, E. Lee, S. H. Min, and B.-S. Kim, "Highly Tunable Interfacial Adhesion of Glass Fiber by Hybrid Multilayers of Graphene Oxide and Aramid Nanofiber," *ACS Applied Materials & Interfaces*, vol. 7, no. 5, pp. 3329–3334, 2015.

[116] J. Fan, J. Wang, Z. Shi, S. Yu, and J. Yin, "Kevlar nanofiber-functionalized multiwalled carbon nanotubes for polymer reinforcement," *Materials Chemistry and Physics*, vol. 141, no. 2, pp. 861–868, 2013.

[117] J. Fan, Z. Shi, L. Zhang, J. Wang, and J. Yin, "Aramid nanofiber-functionalized graphene nanosheets for polymer reinforcement," *Nanoscale*, vol. 4, no. 22, pp. 7046–7055, 2012.

[118] J. Fan, Z. Shi, M. Tian, and J. Yin, "Graphenearamid nanofiber nanocomposite paper with high mechanical and electrical performance," *RSC Advances*, vol. 3, no. 39, p. 17664, 2013.

[119] M. Treacy, T. W. Ebbesen, and J. M. Gibson, "Exceptionally high Young's modulus observed for individual carbon nanotubes," *Nature*, vol. 381, no. 6584, pp. 678–680, 1996.

[120] T. W. Ebbesen, H. J. Lezec, H. Hiura, J. W. Bennett, H. F. Ghaemi, and T. Thio, "Electrical conductivity of individual carbon nanotubes," *Nature*, vol. 382, no. 6586, pp. 54–56, 1996.

[121] P. Kim, L. Shi, A. Majumdar, and P. L. McEuen, "Thermal Transport Measurements of Individual Multiwalled Nanotubes," *Physical Review Letters*, vol. 87, no. 21, p. 215502, 2001.

[122] S. Hu, R. Rajamani, and X. Yu, "Flexible solid-state paper based carbon nanotube supercapacitor," *Applied Physics Letters*, vol. 100, no. 10, p. 104103, 2012.

[123] Z. Fan, J. Yan, L. Zhi, Q. Zhang, T. Wei, J. Feng, M. Zhang, W. Qian, and F. Wei, "A three-dimensional carbon nanotube/graphene sandwich and its application as electrode in supercapacitors," *Advanced Materials (Deerfield Beach, Fla.)*, vol. 22, no. 33, pp. 3723–3728, 2010.

[124] D. Yu and L. Dai, "Self-Assembled Graphene/Carbon Nanotube Hybrid Films for Supercapacitors," *The Journal of Physical Chemistry Letters*, vol. 1, no. 2, pp. 467–470, 2010.

[125] V. Gupta and N. Miura, "Polyaniline/single-wall carbon nanotube (PANI/SWCNT) composites for high performance supercapacitors," *Electrochimica Acta*, vol. 52, no. 4, pp. 1721–1726, 2006.

[126] V. Subramanian, H. Zhu, and B. Wei, "Synthesis and electrochemical characterizations of amorphous manganese oxide and single walled carbon nanotube composites as supercapacitor electrode materials," *Electrochemistry Communications*, vol. 8, no. 5, pp. 827–832, 2006.

[127] X. Yang, C. Cheng, Y. Wang, L. Qiu, and D. Li, "Liquid-mediated dense integration of graphene materials for compact capacitive energy storage," *Science (New York, N.Y.)*, vol. 341, no. 6145, pp. 534–537, 2013.

[128] S. Stankovich, D. A. Dikin, R. D. Piner, K. A. Kohlhaas, A. Kleinhammes, Y. Jia, Y. Wu, S. B. T. Nguyen, and R. S. Ruoff, "Synthesis of graphene-based nanosheets via chemical reduction of exfoliated graphite oxide," *Carbon*, vol. 45, no. 7, pp. 1558–1565, 2007.

[129] D. T. Pham, T. H. Lee, D. H. Luong, F. Yao, A. Ghosh, V. T. Le, T. H. Kim, B. Li, J. Chang, and Y. H. Lee, "Carbon nanotube-bridged graphene 3d building blocks for ultrafast compact supercapacitors," *ACS nano*, vol. 9, no. 2, pp. 2018–2027, 2015.

[130] Q. Cheng, J. Tang, J. Ma, H. Zhang, N. Shinya, and L.-C. Q. Qin, "Graphene and carbon nanotube composite electrodes for supercapacitors with ultra-high energy density," *Physical Chemistry Chemical Physics*, vol. 13, no. 39, pp. 17615–17624, 2011.

[131] J. R. Hattrick-Simpers, K. Choudhary, and C. Corgnale, "A simple constrained machine learning model for predicting high-pressure-hydrogen-compressor materials," *Molecular Systems Design & Engineering*, vol. 3, no. 3, pp. 509–517, 2018.

[132] G. Hautier, C. C. Fischer, A. Jain, T. Mueller, and G. Ceder, "Finding Natures Missing Ternary Oxide Compounds Using Machine Learning and Density Functional Theory," *Chemistry of Materials*, vol. 22, no. 12, pp. 3762–3767, 2010.

[133] H. Li, C. R. Collins, T. G. Ribelli, K. Matyjaszewski, G. J. Gordon, T. Kowalewski, and D. J. Yaron, "Tuning the molecular weight distribution from atom transfer radical polymerization using deep reinforcement learning," *Molecular Systems Design & Engineering*, vol. 3, no. 3, pp. 496–508, 2018.

[134] J. Ling, M. Hutchinson, E. Antono, S. Paradiso, and B. Meredig, "High-Dimensional Materials and Process Optimization Using Data-Driven Experimental Design with Well-Calibrated Uncertainty Estimates," *Integrating Materials and Manufacturing Innovation*, vol. 6, no. 3, pp. 207–217, 2017.

[135] B. C. Rinderspacher and J. M. Elward, "Enriched optimization of molecular properties under constraints: an electrochromic example," *Molecular Systems Design & Engineering*, vol. 3, no. 3, pp. 485–495, 2018.

[136] S. K. Suram, J. A. Haber, J. Jin, and J. M. Gregoire, "Generating Information-Rich High-Throughput Experimental Materials Genomes using Functional Clustering via Multitree Genetic Programming and Information Theory," *ACS Combinatorial Science*, vol. 17, no. 4, pp. 224–233, 2015.

[137] R. J. Xu, J. H. Olshansky, P. D. F. Adler, Y. Huang, M. D. Smith, M. Zeller, J. Schrier, and A. J. Norquist, "Understanding structural adaptability: a reactant informatics approach to experiment design," *Molecular Systems Design & Engineering*, vol. 3, no. 3, pp. 473–484, 2018.

[138] D. D. Landis, J. S. Hummelshoj, S. Nestorov, J. Greeley, M. Dulak, T. Bligaard, J. K. Norskov, and K. W. Jacobsen, "The Computational Materials Repository," *Computing in Science & Engineering*, vol. 14, no. 6, pp. 51–57, 2012.

[139] S. Curtarolo, G. L. W. Hart, M. B. Nardelli, N. Mingo, S. Sanvito, and O. Levy, "The high-throughput highway to computational materials design," *Nature Materials*, vol. 12, no. 3, pp. 191–201, 2013.

[140] G. B. Olson, "Computational Design of Hierarchically Structured Materials," *Science*, vol. 277, no. 5330, pp. 1237–1242, 1997.

[141] D. R. Jones, M. Schonlau, and W. J. Welch, "Efficient Global Optimization of Expensive Black-Box Functions," *Journal of Global Optimization*, vol. 13, no. 4, pp. 455–492, 1998.

[142] E. Brochu, V. M. Cora, and N. de Freitas, "A Tutorial on Bayesian Optimization of Expensive Cost Functions, with Application to Active User Modeling and Hierarchical Reinforcement Learning," *arXiv:1012.2599 [cs]*, 2010.

[143] P. V. Balachandran, J. Theiler, J. M. Rondinelli, and T. Lookman, "Materials Prediction via Classification Learning," *Scientific Reports*, vol. 5, p. 13285, 2015.

[144] D. T. Fullwood, S. R. Niezgoda, B. L. Adams, and S. R. Kalidindi, "Microstructure sensitive design for performance optimization," *Progress in Materials Science*, vol. 55, no. 6, pp. 477–562, 2010.

[145] C. C. Tasan, M. Diehl, D. Yan, M. Bechtold, F. Roters, L. Schemmann, C. Zheng, N. Peranio, D. Ponge, M. Koyama, *et al.*, "An overview of dual-phase steels: advances in microstructure-oriented processing and micromechanically guided design," *Annual Review of Materials Research*, vol. 45, pp. 391–431, 2015.

[146] The Minerals Metals & Materials Society (TMS), *Modeling Across Scales: A Roadmapping Study for Connecting Materials Models and Simulations Across Length and Time Scales*. Warrendale, PA: TMS, 2015.

[147] J. M. Jani, M. Leary, A. Subic, and M. A. Gibson, "A review of shape memory alloy research, applications and opportunities," *Materials and Design*, vol. 56, pp. 1078–1113, 2014.

[148] G. Machado, H. Louche, T. Alonso, and D. Favier, "Superelastic cellular niti tube-based materials: Fabrication, experiments and modeling," *Materials and Design*, vol. 65, pp. 212 – 220, 2015.

[149] D. Dye, "Shape memory alloys: Towards practical actuators," *Nature materials*, vol. 14, no. 8, p. 760, 2015.

[150] B. Holschuh, E. Obropta, and D. Newman, "Low spring index niti coil actuators for use in active compression garments," *IEEE/ASME Transactions on Mechatronics*, vol. 20, no. 3, pp. 1264–1277, 2015.

[151] J. H. Panchal, S. R. Kalidindi, and D. L. McDowell, "Key computational modeling issues in integrated computational materials engineering," *Computer-Aided Design*, vol. 45, no. 1, pp. 4–25, 2013.

[152] D. Howe, B. Goodlet, J. Weaver, and G. Spanos, "Insights from the 3rd world congress on integrated computational materials engineering," *JOM*, vol. 68, no. 5, pp. 1378–1384, 2016.

[153] M. Abramson, C. Audet, G. Couture, J. J.E. Dennis, S. L. Digabel, and C. Tribes, "The NOMAD project," 2015.

[154] E. Kozeschnik, "Matcalc: The materials calculator," 2017.

[155] E. Kozeschnik, K. Janssens, and C. Bataille, *Modeling solid-state precipitation*. Momentum Press, 2012.

[156] C. Audet, S. Le Digabel, and C. Tribes, "NOMAD user guide," Tech. Rep. G-2009-37, Les cahiers du GERAD, 2009.

[157] S. Le Digabel, "Algorithm 909: NOMAD: Nonlinear optimization with the MADS algorithm," *ACM Transactions on Mathematical Software*, vol. 37, no. 4, pp. 1–15, 2011.

[158] B. E. Franco, J. Ma, B. Loveall, G. A. Tapia, K. Karayagiz, J. Liu, A. Elwany, R. Arroyave, and I. Karaman, "A Sensory Material Approach for Reducing Variability in Additively Manufactured Metal Parts," *Scientific Reports*, vol. 7, 2017.

[159] P. Nie, O. A. Ojo, and Z. Li, "Numerical modeling of microstructure evolution during laser additive manufacturing of a nickel-based superalloy," *Acta Materialia*, vol. 77, no. Supplement C, pp. 85–95, 2014.

[160] C. Haberland, M. Elahinia, J. M. Walker, H. Meier, and J. Frenzel, "On the development of high quality NiTi shape memory and pseudoelastic parts by additive manufacturing," *Smart Materials and Structures*, vol. 23, no. 10, p. 104002, 2014.

[161] J. Raplee, A. Plotkowski, M. Kirka, R. Dinwiddie, A. Okello, R. Dehoff, and S. Babu, "Thermographic Microstructure Monitoring in Electron Beam Additive Manufacturing," *Scientific Reports*, vol. 7, p. 43554, 2017.

[162] J. Sam, B. Franco, J. Ma, I. Karaman, A. Elwany, and J. H. Mabe, "Tensile actuation response of additively manufactured nickel-titanium shape memory alloys," *Scripta Materialia*, vol. 146, pp. 164–168, 2018.

[163] K. Karayagiz, A. Elwany, G. Tapia, B. Franco, L. Johnson, J. Ma, I. Karaman, and R. Arróyave, "Numerical and experimental analysis of heat distribution in the laser powder bed fusion of Ti-6al-4v," *IISE Transactions*, vol. 0, no. 0, pp. 1–17, 2018.

[164] E. Y. Panchenko, Y. I. Chumlyakov, I. V. Kireeva, A. V. Ovsyannikov, H. Sehitoglu, I. Karaman, and Y. H. J. Maier, "Effect of disperse Ti3n4 particles on the martensitic transformations in titanium nickelide single crystals," *The Physics of Metals and Metallography*, vol. 106, no. 6, p. 577, 2008.

[165] M. Nishida, C. M. Wayman, and T. Honma, "Precipitation processes in near-equiatomic TiNi shape memory alloys," *Metallurgical Transactions A*, vol. 17, no. 9, pp. 1505–1515, 1986.

[166] S. Baroni, S. de Gironcoli, A. Dal Corso, and P. Giannozzi, "Phonons and related crystal properties from density-functional perturbation theory," *Reviews of Modern Physics*, vol. 73, no. 2, pp. 515–562, 2001.

[167] J. M. Perez-Mato, S. V. Gallego, E. S. Tasci, L. Elcoro, G. de la Flor, and M. I. Aroyo, "Symmetry-Based Computational Tools for Magnetic Crystallography," in *Annual Review of Materials Research, Vol 45* (D. R. Clarke, ed.), vol. 45, pp. 217–248, Palo Alto: Annual Reviews, 2015.

[168] M. I. Aroyo, J. M. Perez-Mato, D. Orobengoa, E. Tasci, G. de la Flor, and A. Kirov, "Crystallography online: Bilbao Crystallographic Server," *Bulgarian Chemical Communications*, vol. 43, no. 2, pp. 183–197, 2011.

[169] E. Kozeschnik, *Modeling solid-state precipitation*. [New York, N.Y.] (222 East 46th Street, New York, NY 10017): Momentum Press, 2013.

[170] M. Seifi, A. Salem, J. Beuth, O. Harrysson, and J. J. Lewandowski, "Overview of materials qualification needs for metal additive manufacturing," *JOM*, vol. 68, no. 3, pp. 747–764, 2016.

[171] B. Dutta and F. H. S. Froes, "The Additive Manufacturing (AM) of titanium alloys," *Metal Powder Report*, vol. 72, no. 2, pp. 96–106, 2017.

[172] B. Baufeld, O. Van der Biest, and R. Gault, "Additive manufacturing of Ti–6Al–4V components by shaped metal deposition: microstructure and mechanical properties," *Materials & Design*, vol. 31, pp. S106–S111, 2010.

[173] Y. Zhu, J. Li, X. Tian, H. Wang, and D. Liu, "Microstructure and mechanical properties of hybrid fabricated Ti–6.5 Al–3.5 Mo–1.5 Zr–0.3 Si titanium alloy by laser additive manufacturing," *Materials Science and Engineering: A*, vol. 607, pp. 427–434, 2014.

[174] G. Dinda, A. Dasgupta, and J. Mazumder, "Laser aided direct metal deposition of inconel 625 superalloy: Microstructural evolution and thermal stability," *Materials Science and Engineering: A*, vol. 509, no. 1-2, pp. 98–104, 2009.

[175] G. Bi, C.-N. Sun, H.-c. Chen, F. L. Ng, and C. C. K. Ma, "Microstructure and tensile properties of superalloy IN100 fabricated by micro-laser aided additive manufacturing," *Materials & Design*, vol. 60, pp. 401–408, 2014.

[176] W. J. Sames, K. A. Unocic, R. R. Dehoff, T. Lolla, and S. S. Babu, "Thermal effects on microstructural heterogeneity of Inconel 718 materials fabricated by electron beam melting," *Journal of Materials Research*, vol. 29, no. 17, pp. 1920–1930, 2014.

[177] K. Guan, Z. Wang, M. Gao, X. Li, and X. Zeng, "Effects of processing parameters on tensile properties of selective laser melted 304 stainless steel," *Materials & Design*, vol. 50, pp. 581–586, 2013.

[178] I. Tolosa, F. Garciandía, F. Zubiri, F. Zapirain, and A. Esnaola, "Study of mechanical properties of aisi 316 stainless steel processed by "selective laser melting", following different manufacturing strategies," *The International Journal of Advanced Manufacturing Technology*, vol. 51, no. 5-8, pp. 639–647, 2010.

[179] M. Mahmoudi, G. Tapia, B. Franco, J. Ma, R. Arroyave, I. Karaman, and A. Elwany, "On the printability and transformation behavior of nickel-titanium shape memory alloys fabricated using laser powder-bed fusion additive manufacturing," *Journal of Manufacturing Processes*, vol. 35, pp. 672–680, 2018.

[180] G. Tapia, W. King, L. Johnson, R. Arroyave, I. Karaman, and A. Elwany, "Uncertainty Propagation Analysis of Computational Models in Laser Powder Bed Fusion Additive Manufacturing Using Polynomial Chaos Expansions," *Journal of Manufacturing Science and Engineering*, vol. 140, no. 12, pp. 121006–121006–12, 2018.

[181] C. Kamath, B. El-dasher, G. F. Gallegos, W. E. King, and A. Sisto, "Density of additively-manufactured, 316l SS parts using laser powder-bed fusion at powers up to 400 W," *The International Journal of Advanced Manufacturing Technology*, vol. 74, no. 1-4, pp. 65–78, 2014.

[182] I. Yadroitsev, A. Gusarov, I. Yadroitsava, and I. Smurov, "Single track formation in selective laser melting of metal powders," *Journal of Materials Processing Technology*, vol. 210, no. 12, pp. 1624–1631, 2010.

[183] I. Yadroitsev, P. Krakhmalev, and I. Yadroitsava, "Hierarchical design principles of selective laser melting for high quality metallic objects," *Additive Manufacturing*, vol. 7, pp. 45–56, 2015.

[184] I. Yadroitsev, I. Yadroitsava, P. Bertrand, and I. Smurov, "Factor analysis of selective laser melting process parameters and geometrical characteristics of synthesized single tracks," *Rapid Prototyping Journal*, vol. 18, no. 3, pp. 201–208, 2012.

[185] G. Tapia and A. Elwany, "A review on process monitoring and control in metal-based additive manufacturing," *Journal of Manufacturing Science and Engineering*, vol. 136, no. 6, p. 060801, 2014.

[186] S. K. Everton, M. Hirsch, P. Stravroulakis, R. K. Leach, and A. T. Clare, "Review of in-situ process monitoring and in-situ metrology for metal additive manufacturing," *Materials & Design*, vol. 95, pp. 431–445, 2016.

[187] P. Lott, H. Schleifenbaum, W. Meiners, K. Wissenbach, C. Hinke, and J. Bültmann, "Design of an optical system for the in situ process monitoring of selective laser melting (slm)," *Physics Procedia*, vol. 12, pp. 683–690, 2011.

[188] M. Cola and S. Betts, "In-Situ Process Mapping using Thermal Quality Signatures during Additive Manufacturing with Titanium Alloy Ti-6al-4v," *Case Study for Sigma Labs*, p. 29, 2018.

[189] L. Scime and J. Beuth, "Using machine learning to identify in-situ melt pool signatures indicative of flaw formation in a laser powder bed fusion additive manufacturing process," *Additive Manufacturing*, vol. 25, pp. 151–165, 2019.

[190] M. H. Farshidianfar, A. Khajepour, and A. P. Gerlich, "Effect of real-time cooling rate on microstructure in laser additive manufacturing," *Journal of Materials Processing Technology*, vol. 231, pp. 468–478, 2016.

[191] W. Huang and R. Kovacevic, "Feasibility study of using acoustic signals for online monitoring of the depth of weld in the laser welding of high-strength steels," *Proceedings of the Institution of Mechanical Engineers, Part B: Journal of Engineering Manufacture*, vol. 223, no. 4, pp. 343–361, 2009.

[192] T. H. C. Childs, C. Hauser, and M. Badrossamay, "Selective laser sintering (melting) of stainless and tool steel powders: Experiments and modelling," *Proceedings of the Institution of Mechanical Engineers, Part B: Journal of Engineering Manufacture*, vol. 219, no. 4, pp. 339–357, 2005.

[193] D. Tomus, P. A. Rometsch, M. Heilmaier, and X. Wu, "Effect of minor alloying elements on crack-formation characteristics of Hastelloy-X manufactured by selective laser melting," *Additive Manufacturing*, vol. 16, pp. 65–72, 2017.

[194] N. J. Harrison, I. Todd, and K. Mumtaz, "Reduction of micro-cracking in nickel superalloys processed by selective laser melting: A fundamental alloy design approach," *Acta Materialia*, vol. 94, pp. 59–68, 2015.

[195] J. Gockel and J. Beuth, "Understanding Ti-6al-4v microstructure control in additive manufacturing via process maps," *Solid Freeform Fabrication Proceedings, Austin, TX, Aug*, pp. 12–14, 2013.

[196] T. Mukherjee, J. S. Zuback, A. De, and T. DebRoy, "Printability of alloys for additive manufacturing," *Scientific Reports*, vol. 6, 2016.

[197] V. Juechter, T. Scharowsky, R. F. Singer, and C. Körner, "Processing window and evaporation phenomena for Ti6al4v produced by selective electron beam melting," *Acta Materialia*, vol. 76, pp. 252–258, 2014.

[198] T. H. C. Childs, C. Hauser, and M. Badrossamay, "Mapping and Modelling Single Scan Track Formation in Direct Metal Selective Laser Melting," *CIRP Annals*, vol. 53, no. 1, pp. 191–194, 2004.

[199] T. DebRoy, H. Wei, J. Zuback, T. Mukherjee, J. Elmer, J. Milewski, A. Beese, A. Wilson-Heid, A. De, and W. Zhang, "Additive manufacturing of metallic components–process, structure and properties," *Progress in Materials Science*, vol. 92, pp. 112–224, 2018.

[200] J. C. Ion, H. R. Shercliff, and M. F. Ashby, "Diagrams for laser materials processing," *Acta Metallurgica et Materialia*, vol. 40, no. 7, pp. 1539–1551, 1992.

[201] G. Taguchi and A. J. Rafanelli, "Taguchi on Robust Technology Development: Bringing Quality Engineering Upstream," *Journal of Electronic Packaging*, vol. 116, no. 2, pp. 161–161, 1994.

[202] H.-J. Choi, *A robust design method for model and propagated uncertainty*. PhD Thesis, Georgia Institute of Technology, 2005.

[203] W. Chen, M. M. Wiecek, and J. Zhang, "Quality Utility A Compromise Programming Approach to Robust Design," *Journal of Mechanical Design*, vol. 121, no. 2, pp. 179–187, 1999.

[204] E. Sandgren and T. M. Cameron, "Robust design optimization of structures through consideration of variation," *Computers & Structures*, vol. 80, no. 2021, pp. 1605–1613, 2002.

[205] S. Chandrasekhar, *Hydrodynamic and Hydromagnetic Stability*. Courier Corporation, 2013.

[206] J. C. Steuben, A. P. Iliopoulos, and J. G. Michopoulos, "Discrete element modeling of particle-based additive manufacturing processes," *Computer Methods in Applied Mechanics and Engineering*, vol. 305, pp. 537–561, 2016.

[207] A. Block-Bolten and T. W. Eagar, "Metal vaporization from weld pools," *Metallurgical Transactions B*, vol. 15, no. 3, pp. 461–469, 1984.

[208] C. B. Alcock, V. P. Itkin, and M. K. Horrigan, "Vapour Pressure Equations for the Metallic Elements: 298-2500k," *Canadian Metallurgical Quarterly*, vol. 23, no. 3, pp. 309–313, 1984.

[209] C. J. Smithells, W. F. Gale, and T. C. Totemeier, *Smithells metals reference book*. Amsterdam ; Boston: Elsevier Butterworth-Heinemann, 8th ed. / edited by w.f. gale, t.c. totemeier ed., 2004.

[210] M. Laurent Brocq, A. Akhatova, L. Perrière, S. Chebini, X. Sauvage, E. Leroy, and Y. Champion, "Insights into the phase diagram of the CrMnFeCoNi high entropy alloy," *Acta Materialia*, vol. 88, pp. 355–365, 2015.

[211] M. W. Chase, "NIST JANAF Themochemical Tables, Fourth Edition," tech. rep., National Institute of Standards and Technology, 1998.

[212] S. Roy, M. Juha, M. S. Shephard, and A. M. Maniatty, "Heat transfer model and finite element formulation for simulation of selective laser melting," *Computational Mechanics*, vol. 62, no. 3, pp. 273–284, 2018.

[213] I. Couckuyt, T. Dhaene, and P. Demeester, "ooDACE toolbox: a flexible object-oriented Kriging implementation," *The Journal of Machine Learning Research*, vol. 15, no. 1, pp. 3183–3186, 2014.

[214] I. Toda-Caraballo, E. I. Galindo-Nava, and P. E. J. Rivera-Díaz-del Castillo, "Unravelling the materials genome: Symmetry relationships in alloy properties," *Journal of Alloys and Compounds*, vol. 566, pp. 217–228, 2013.

[215] T. Iida and R. I. L. Guthrie, *The thermophysical properties of metallic liquids. Volume 2: Predictive models*. Oxford: Oxford University Press, first edition ed., 2015.

[216] H.-J. Fecht and R. K. Wunderlich, "Fundamentals of Liquid Processing in Low Earth Orbit: From Thermophysical Properties to Microstructure Formation in Metallic Alloys," *JOM*, vol. 69, no. 8, pp. 1261–1268, 2017.

[217] J. Valencia and P. Quested, "Thermophysical Properties," in *ASM Handook*, vol. 15, pp. 468–481, ASM International, 3rd ed., 2008.

[218] T. Iida and R. I. L. Guthrie, *The Thermophysical Properties of Metallic Liquids: Volume 1 Fundamentals*. Oxford University Press, 2015.

[219] P. Quested, R. Brooks, and B. Monaghan, "The prediction of thermophysical properties for modelling solidification of metallic melts," *High Temperature Materials and Processes*, vol. 22, no. 5, pp. 247–256, 2011.

[220] D. S. Viswanath and B. C. Mathur, "Thermal conductivity of liquid metals and alloys," *Metallurgical Transactions*, vol. 3, no. 7, pp. 1769–1772, 1972-07-01.

[221] K. Mundra, T. DebRoy, T. Zacharia, and S. David, "Role of thermophysical properties in weld pool modeling," *Welding journal*, vol. 71, no. 9, pp. 313–s, 1992.

[222] M. W. Chase, "Themochemical tables, fourth edition," *NIST-JANAF*, pp. 1–1951, 1998.

[223] L. Ward, A. Agrawal, A. Choudhary, and C. Wolverton, "A general-purpose machine learning framework for predicting properties of inorganic materials," *npj Computational Materials*, vol. 2, p. 16028, 2016.

[224] L. Wang, N. Wang, and N. Provatas, "Liquid channel segregation and morphology and their relation with hot cracking susceptibility during columnar growth in binary alloys," *Acta Materialia*, vol. 126, pp. 302–312, 2017.

[225] M. Rappaz, J.-M. Drezet, and M. Gremaud, "A new hot-tearing criterion," *Metallurgical and Materials Transactions A*, vol. 30, no. 2, pp. 449–455, 1999.

[226] T. W. Clyne, M. Wolf, and W. Kurz, "The effect of melt composition on solidification cracking of steel, with particular reference to continuous casting," *Metallurgical Transactions B*, vol. 13, no. 2, pp. 259–266, 1982.

[227] S. Kou, "A simple index for predicting the susceptibility to solidification cracking," *Welding Journal*, vol. 94, no. 12, pp. 374s–388s, 2015. 374s.

[228] S. Kou, "A criterion for cracking during solidification," *Acta Materialia*, vol. 88, pp. 366–374, Apr. 2015.

[229] D. G. Eskin, Suyitno, and L. Katgerman, "Mechanical properties in the semi-solid state and hot tearing of aluminium alloys," *Progress in Materials Science*, vol. 49, no. 5, pp. 629–711, 2004.

[230] A. Block-Bolten and T. W. Eagar, "Metal vaporization from weld pools," *Metallurgical Transactions B*, vol. 15, no. 3, pp. 461–469, 1984.

[231] K. Mundra and T. Debroy, *Toward understanding alloying element vaporization during laser beam welding of stainless steel*, vol. 72:1. American Welding Society, 1993.